Cavity Catalysis: Controlling Chemical Reactions through Cooperative Vibrational Strong Coupling

Jyoti

A thesis submitted for the partial fulfillment of

the degree of

Doctor of Philosophy

Department of Chemical Sciences

Indian Institute of Science Education and Research Mohali

Knowledge city, Sector 81, SAS Nagar, Manauli PO, Mohali 140306, Punjab, India.

December, 2022

DEDICATED **to**

MY PARENTS

Declaration

The work presented in this thesis has been carried out by me under the guidance of Dr. Jino George at the Indian Institute of Science Education and Research Mohali. This work has not been submitted in part or in full for a degree, a diploma, or a fellowship to any other university or institute. Whenever contributions of others are involved, every effort is made to indicate this clearly, with due acknowledgement of collaborative research and discussions. This thesis is a bona fide record of original work done by me and all sources listed within have been detailed in the bibliography.

JYOTI

Place:

Date:

In my capacity as the supervisor of the candidate's thesis work, I certify that the above statements by the candidate are true to the best of my knowledge.

Dr. Jino George

Supervisor

Department of Chemical Sciences

IISER Mohali

Place:

Date:

Acknowledgement

It’s an incredible work experience to work under the supervision of Dr. Jino George. I want to express my gratitude for his constructive suggestions during the planning and development of the research work. Being a first student, I feel lucky to learn from scratch, and thanks for converting my mistakes into lessons and skills into strengths. He is always very patient, calm, and kind, which keeps a healthy work environment. I am also thankful for his time on my thesis corrections, suggestions, and for trying to come up with the best version.

I am also grateful to my committee members, Dr. Arijit Kumar De and Dr. P. Balanarayan, for giving valuable suggestions to complete the research objective. I thank Dr. Sugumar Venkataramani and his group members for extending the use of their lab space during my first year.

It is a genuine pleasure to express my gratefulness to Mr. Jaibir Singh and Mr. Thabassum Ahammad for their valuable suggestions throughout completing this work. I thank Mrs. Akhila Kadyan for always being supportive and Ms. Kuljeet Kaur for proofreading my thesis. Apart from this, I am grateful to the beautiful humans in the lab, Dr. Jhuma Dutta, Dr. Ben Johns, Pooja Bhatt, Pallavi Garg, Nitin Yadav, and all MS students, for facilitating a wonderful atmosphere in the lab.

I express deepest thanks to Mr. Sumit Mishra for his constant support and exploring the beautiful city “Chandigarh”. Ms. Samita Mishra for endless tea sessions, and my roommates Sonam, Himanshi and Komal. Finally, I would like to thank my parents for their love and encouragement during my study. I also thank my brother and elder sisters, who always support me in achieving high in my carrier. Furthermore, I am grateful to the beautiful humans who joined me in IISER Mohali. Lastly, I would like to acknowledge the IISER community for facilitating a remarkable opportunity.

Contents

List of Figures……VII

List of Tables……...XI

List of Schemes……..…….XII

Abbreviations……XIII

Preface……...…….....XV

Chapter 1. **Introduction: Light-Matter Interactions**……1

1.1 Motivation……2

1.2 Light-Matter Interactions……3

(a) Weak Interactions……3

(b) Strong Coupling……...5

1.3 Coherent Control of Chemical Reaction and Light-Matter Coupling……8

1.4 Chemical reaction in strong coupling conditions……16

1.5 Applications of VSC beyond chemical reactivity……...23

Chapter 2. **Ester Solvolysis under Cooperative Vibrational Strong Coupling**: **The Concept of Cavity Catalysis Solvolysis**……..25

2.1 Cooperative VSC……26

2.2 Fabry-Perot Resonator……27

2.3 a. Ester solvolysis in Fabry-Perot cavities……..31

2. 3 b. Corrections to the original paper……36

2.4 Result and Discussion……37

2.5 Conclusion……..46

Chapter 3. **Study of structure-reactivity relationship under cooperative VSC**……47

3.1 Introduction……48

3.2 Linear Free-Energy Relationships (LFER)……48

3.3. Reaction Series studied for LFER under VSC……54

3.4 Result and Discussion……59

3.5 Conclusion……..68

Chapter 4. **Improving Enzyme Catalytic Efficiency by Cooperative Vibrational Strong Coupling of Water**……..69

4.1 Introduction……70

4.2 Selection of Enzyme: α −Chymotrypsin……72

4.3 Type of inhibition……...75

4.4 Experiment methods to study the kinetic parameter of $\alpha - CT$ under VSC……...76

4.4.1. Solution preparation……..76

4.4.2. Cavity preparation and reaction study……...77

4.5 Result and Discussion……80

4.6 Conclusion……..90

Chapter 5. **Conclusion and Outlook**……..…91

References……...94

List of Publications……...106

List of Conferences……...107

List of Figures

Figure 1.1. Purcell enhancement of spontaneous emission. (a) in free space; (b) Weak coupling to a cavity mode will enhance the spontaneous rate of emission by increasing the local density of modes (M_1 and M_2 representing mirrors).

Figure 1.2. Infinite vacuum states are available in space with zero-point energy.

Figure 1.3. (a) Schematic illustration of the weak and strong coupling between the optical cavity and molecular transition; (b) weak coupling results in the spontaneous emission $\kappa + \gamma > 2g$; (c) strong coupling results in Rabi oscillation $\kappa + \gamma < 2g$.

Figure 1.4. Schematic diagram of between a molecular transition and a cavity resonance, in which two hybrid light−matter states $P+$ and $P-$ are formed and are separated by the so-called Rabi splitting energy $\hbar\Omega_R$. (Ebbesen et al. 2016)

Figure 1.5. Collective coupling (VSC) of N oscillators with the optical mode.

Figure 1.6. Floquet calculation for the H_2^+ molecular potential deforms in the presence of intense light with two intensities at 3.5 TW/cm^2 and 56 TW/cm^2. (Schumacher et al. 1989)

Figure 1.7. (a) $C_2H_2/F_2/N_2$~1/1/100: growth of product absorption versus time, corrected for growth 1119.1 cm^{-1} during spectroscopic exposure; (b) Different vibrational modes corresponding to C_2H_2. (Pimentel et al. 1989)

Figure 1.8. Evolution to study chemical reactions by different methods.

Figure 1.9. A display of the PES involved times $t_0 \rightarrow t_\infty$ refers to the evolution of the wavepacket as it moves along the coordinate and is broadened by dispersion. (Zewail et al. 1988)

Figure 1.10. FTS results for NaI as a function of probe wavelength; (a) 575 nm (b) 580 nm (c) 590 nm and (d) 615 nm. (Zewail et al. 1989)

Figure 1.11. (a) Structure of spiropyran (SPI) and merocyanine (MC); (b) Fabry-Perot cavity schematic diagram of the cavity (upper and bottom Ag mirror) and non-cavity (bottom Ag mirror) also measured from the same film; (c) Transmission spectrum of the coupled system in the cavity as a function of irradiation time at 330 nm; (d) Kinetics of the growth of the MC absorbance measured for the bare molecules (red) and the coupled system (green). (Thomas et al. 2016)

Figure 1.12. Strong coupling in electronic and vibrational transition; corresponding Rabi splitting energy represented by $\hbar\Omega_R$ and $\hbar\Omega_{VR}$.

Figure 1.13. (a) Chemical reaction- Silane deprotection of 1-phenyl-2-trimethylsilyl acetylene in the presence of TBAF; (b) IR spectrum of PTA outside (blue trace) and inside ON-resonance (red trace) of the cavity; (c) Under ON-resonance shift on the higher order cavity modes; (d) Kinetic of the reaction ON-resonance (red squares), outside cavity (blue squares) and OFF-resonance cavity (green squares). (Thomas et al. 2016)

Figure 1.14. (a) Reaction rate decreases as a function of the cavity tuning (red squares) and outside cavity (blue squares); (b) Decrease in the ratio of the reaction rates under VSC and outside cavity as a function of the Rabi splitting energy. (Thomas et al. 2016)

Figure 1.15. Eyring plot for the reactions inside the ON-resonance cavity (red squares) and outside the cavity (blue squares). (Thomas et al. 2016)

Figure 1.16. (a) Major silyl cleavage pathways shown are Si-C to form 1, Si-O to form 2 for the reaction of R with TBAF; (b) Cavity tuning as a function of reaction rate inside the cavity (red spheres), blue dashed line represents the average rate of outside the cavity. (Thomas et al. 2019)

Figure 1.17. Schematic illustration of possible transition states under (A) non-cavity and (B) VSC. (Thomas et al. 2020)

Figure 2.1. Cooperative vibration strong coupling of solute-solvent molecules with the cavity mode forms vibro-polaritonic states separated by Rabi splitting energy represented $\hbar\Omega_{VR}$.

Figure 2.2. (a) Image and (b) sketch of a microcavity QED reactor.

Figure 2.3. Schematic representation of the paths of light travel in the Fabry-Perot resonator.

Figure 2.4. FWHM of the cavity mode.

Figure 2.5. IR spectrum of an empty cavity with a free spectral range of 240 cm^{-1}.

Figure 2.6. Absorption spectra showing the evolution of PNP- at 400 nm during the progress of the ester solvolysis.

Figure 2.7. Carbonyl band of PNPA (ATR spectra; black trace) and FTIR spectra of ^{12}EtOAc (red trace); (a) 10% diluted ^{12}EtOAc with hexane; overlapping of carbonyl stretching mode of ^{12}EtOAc and PNPA; (b) pure ^{12}EtOAc coupled with $10th$ mode of the cavity; formed $VP+$ and $VP-$ (blue trace) vibro-polaritonic states.

Figure 2.8. Temporal evolution of PNP- in the FP-cavity with spacer 18 μm using scan kinetic mode of the spectrometer for SBW of; (a) 1 nm and (b) 5 nm.

Figure 2.9. Single point kinetic rate measured (k_{app}) at 407 nm with SBW of 1 nm by tuning the cavity mode (^{12}EtOAc; blue filled circles) and non-cavity (^{12}EtOAc; blue empty circles). The dashed curve is a guide to the eye.

Figure 2.10. Reaction kinetics at 400 nm in non-cavity (black trace), OFF-resonance at 1801 cm^{-1} (red trace), ON-resonance at 1764 cm^{-1} (blue trace) corresponding; (a) Absorption traces; (b) Kinetic traces follows pseudo-first-order.

Figure 2.11. The experiment was performed by tuning the cavity mode position by changing the FSR value at 400 nm with SBW of 5 nm; (a) Abs vs. time; (b) Calculation of reaction rate; given in table 2.1.

Figure 2.12. Kinetic action spectra of cavity tuning experiments around the C=O_{str} of PNPA molecules: cavity (filled blue circles) and non-cavity (empty blue circles). The dotted line is a guide to eye.

Figure 2.13. Carbonyl band of PNPA (ATR spectra; black trace) and FTIR spectra of ^{13}EtOAc (red trace); (a) 10% diluted ^{13}EtOAc with hexane; (b) Pure ^{13}EtOAc coupled with $10th$ mode of the cavity; formed $VP+$ and $VP-$ (blue trace).

Figure 2.14. Comparison of kinetics rate by changing the isotope of solvent from ^{12}EtOAc to ^{13}EtOAc. (a) Vibrational overlapping of C=O_{str} of ^{12}EtOAc with PNPA whereas ^{13}EtOAc shifts the band position; (b) Corresponding kinetic traces measured by tuning the cavity (^{12}EtOAc:

blue filled circles;[13]EtOAc: red filled circles) and non-cavity ([12]EtOAc: empty blue circles;[13]EtOAc: empty red circles).

Figure 2.15. Eyring plot for a reaction inside the cavity (blue circles) and non-cavity (red circles).

Figure 3.1. Deviation of Hammett plot for the series of reactions (a) concave downward (b) concave upward (c) Log k versus a for the reaction of benzaldehydes and n-butyl amine.[97] (d) Log k versus σ for the reaction of benzyl chlorides with thiosulfate in (1) ethanol, (2) diglyme, and (3) acetone. [97]

Figure 3.2. A TS diagram for single-step reactions and corresponding linear Hammett plot.

Figure 3.3. (a) Hypothetical cases for IKR occurrence for a reaction series (b) Van't Hoff plots of the alkaloids belonging to Dihydrosanguinarine (4), Berberine (5), Stilopine (6), Allocryptopine (7), Sanguinarine (8), Protopine (9).

Figure 3.4. Scan kinetics for the formation of *PNP*- ions from *PNPB* and *m-CH3* (a, c) non-cavity; (b, d) ON-resonance cavity.

Figure 3.5. Formation of PNP- ions during the reaction for solvolysis of PNPB (non-cavity) kept for 5000 $seconds$.

Figure 3.6. FTIR spectra of neat IPAc solvent (green trace), *p-CH3* in chloroform (red trace) and cavity ON-resonance $7th$ mode coupling with C=O_{str} band of solute and solvent molecules show the formation of vibro-polaritonic ($VP+$ and $VP-$) states.

Figure 3.7. Reaction rate plot for non-cavity and ON-resonance cavity (a) *p-Cl*, (b) *m-CH3*, (c) *p- CH3*, (d) *PNPB*, (e) *m-OCH3*, (f) *m-Cl*.

Figure 3.8. Tuning of the 7th mode position moved slowly from 1680 cm^{-1} to 1780 cm^{-1} in each experiment, and the corresponding k_{app} was plotted with the IR transmission spectra of the C=O_{str} band of solute (red trace) and solvent molecules (green trace). An increase in k_{app} was observed (blue squares) at the ON-resonance conditions for (a) *p-Cl*, (b) *p- CH3*, and (c) *m-CH3* derivatives [blue dotted curve is guiding to eye].

Figure 3.9. Hammett plot for a series of ester solvolysis (*p-CH3, m-CH3, m-OCH3, p-Cl, and m-Cl*) in non-cavity (red squares) and ON-resonance cavity conditions (blue squares).

Figure 3.10. IR spectrum of acetonitrile (green trace), solute *p-CH3* (red trace), and the calculated reaction rate k_{app} for detuning experiment of cavity (dark black circles) and non-cavity (empty black circles).

Figure 3.11. Concentration dependence experiment by mixing anisole and IPAc in different ratios and the corresponding reaction rate *p-CH3* for non-cavity (red squares) and ON-resonance cavity (blue squares).

Figure 3.12. Temperature dependence experiment for non-cavity and cavity;(a) *p-CH3*, (b) *p-Cl*, (c) *m-OCH3*, (d) *PNPB*.

Figure 3.13. (a) Thermodynamic relation between the free energy of activation versus σ for the cavity (blue circles) and non-cavity (red squares); (b) Enthalpy-entropy compensation plot for cavity versus non-cavity experiments is listed in table 3.3.

Figure 4.1. Pepsin enzymatic activity under VSC of the water stretching mode. (a) Emission spectra between $500-596\ nm$ were collected under excitation with $485\ nm$ light for the

pepsin hydrolytic activity towards substrate in a Fabry–Perot cavity; (b) kinetic traces for on- and off-resonance to the water stretching vibration; (c) Detuning plot for $6th$ order mode, $7th$ order mode and $10th$ order mode coupled. Blue dashed curve: water absorption coefficient. Black line: average measured initial reaction velocity of reactions measured in a non-cavity. (Vergauwe et al. 2019)

Figure 4.2. UV-Visible spectra of $\alpha - CT$ in TRIS buffer at different concentrations $0.05M$ (black line), $0.5\ M$ (red line), $0.1\ M$ (blue line) at pH 8.0 and temperature 25℃.

Figure 4.3. Modes of inhibition (a) Competitive inhibition; (b) Non-competitive inhibition; (c) Uncompetitive inhibition.

Figure 4.4. ATR absorption spectra (red and blue arrow) of water (O-H_{str}; red trace), $\alpha - CT$ (blue trace) , and transmission spectrum corresponds to black arrow shows the formation of $VP+$ and $VP-$ with mylar spacer 6 μm coupling of 7th mode of the cavity (black trace) with O-H_{str} bond.

Figure 4.5. Beer law plot- follow linear relation in the (a) non-cavity (b) cavity; by varying the PNPA concentration $0.4 - 2.0\ mM$ and keeping enzyme concentration fixed $E_0 = 5 \times 10^{-5} M$ for a pathlength of 25 μm.

Figure 4.6. Michaelis-Menten plot for non-cavity keeping fixed concentration of enzyme $5 \times 10^{-5} M$ and varying the substrate concentration $0.4 - 2.0\ mM$.

Figure 4.7. Temporal evolution of PNP- ions during the hydrolysis with $\alpha - CT$ ($5 \times 10^{-5} M$) with PNPA $0.5\ mM$ for (a,b) non-cavity and cavity with $25\ \mu m$, (c,d) are the corresponding rate plot.

Figure 4.8. Lineweaver-Burk plot for the hydrolysis of PNPA ($0.4 - 2.0\ mM$) using $\alpha - CT$ ($5 \times 10^{-5} M$), non-cavity (red trace), and cavity (blue trace).

Figure 4.9. Comparison of half-cavity (black trace), ON-resonance (blue trace), and half-cavity (black trace) with a PNPA concentration of $0.4\ mM$.

Figure 4.10. FT-IR spectra of D_2O in red traces and FP cavity mode splitting into $VP+$ $and\ VP-$ in black traces with $25\ \mu m$ spacer.

Figure 4.11. (a) High-resolution mass spectra of $\alpha - CT$ in H_2O (black trace), D_2O (red trace) at zero time; (b) is the corresponding zoomed spectra indicating the fractional change in the m/z value, and (c) Aging experiment of $\alpha - CT$ in D_2O.

Figure 4.12. Circular dichroism spectra of α-CT in a buffer solution of H_2O (black trace), D_2O (red trace).

Figure 4.13. Lineweaver-Burk plot for the hydrolysis of PNPA in D_2O for the non-cavity (black squares) and a cavity (violet circles) by coupling to the O-D_{str} band and its comparison with the O-H_{str} band of water coupling.

Figure 4.14. (a) Experimental cavity dispersion of vibro-polaritonic states formed by coupling O-H_{str} mode of water molecules in 6 μm spacer; (b) Dispersive curve of Vibro-polaritonic states by using TMM simulation.

Figure 4.15. The enzymatic reaction with a fixed concentration of PNPA ($0.4\ mM$) and $\alpha - CT$ ($5 \times 10^{-5} M$) by changing the concentration of H_2O: D_2O molecules in the non-cavity (red dot) and cavity (blue dot). (Dotted lines are guides to the eye)

Figure 5.1. (A, B) Laser control experiments used (A) Non-resonance pumping; (B) Resonance pumping; (C) Resonance coupling using optical cavities in ground state.

List of Tables

Table 2. 1. k_{app} of tuning experiment.

Table 3. 1. Vibrational frequency of carbonyl band ($C{=}O_{str}$) in the given esters.

Table 3. 2. k_{app} of cavity and non-cavity experiment as plotted in the figure 3.9.

Table 3. 3. Thermodynamic parameter extracted from the linear regression fit of figure 3.12.

Table 4. 1. Hydrolysis of PNPA by $\alpha - CT$ $(5 \times 10^{-5} M)$ keeping $pH = 8.5$ and $T = 22℃$.

List of Schemes

Scheme 2. 1. Base catalyzed solvolysis of PNPA in the ethyl acetate (EtOAc).

Scheme 3. 1. Solvolysis of benzoic acid and its derivative.

Scheme 3. 2. Scheme of PNPB transesterification reaction.

Scheme 4. 1. Mechanism of peptide bond cleavage in the active site of pepsin. (Vergauwe et al. 2019)

Scheme 4. 2. Stepwise mechanism of $\alpha - CT$ involving three distinct steps.

Scheme 4. 3. Charge-Relay mechanism for ester hydrolysis of PNPA using $\alpha - CT$.

Abbreviations

QED – Quantum Electrodynamics

FP cavity – Fabry-Pérot Cavity

FWHM – Full Width Half Maxima

IR – Infrared

TS – Transition State

FTS – Femtosecond Transition State Spectroscopy

PES – Potential Energy Surface

UV – Ultraviolet

PSS – Photostationary State

SPI – Spiropyran

MC – Merocyanine

PVA – Polyvinyl Alcohol

VSC – Vibrational Strong Coupling

$\hbar\Omega_R$ – Electronic Rabi splitting energy

$\hbar\Omega_{VR}$ – Vibrational Rabi splitting energy

PVAc – Polyvinyl Acetate

DPPA – Diphenyl Phosphoryl Azide

PTA – 1-phenyl-2-trimethylsilylacetylene

TBAF – Tetra-n-butylammonium fluoride

FTIR – Fourier Transform Infrared

QEDFT – Quantum-Electrodynamical Density-Functional Theory

Q-factor – Quality Factor

FSR – Free Spectral Range

PNPA – *para*-nitrophenyl acetate

PNP^- – *para*-nitrophenoxide ion

EtOAc – Ethyl Acetate

SBW – Slit band-width

RI – Refractive Index

OD – Optical Density

VET – Vibrational Energy Transfer

LFER – Linear Free-Energy Relationships

EWS – Electron-Withdrawing Substituents

EDS – Electron-Donating Substituents

RDS – Rate-Determining Step

S_N1 – Nucleophilic Substitution Unimolecular Reaction

S_N2 – Nucleophilic Substitution Bimolecular Reaction

IKR – Isokinetic Relationship

NMR – Nuclear Magnetic Resonance

PNPB – *para*-nitrophenyl benzoate

IPAc – Isopropyl Acetate

α −Chymotrpsin – $\alpha - CT$

CD – Circular Dichroism

LBHB – Low Barrier Hydrogen Bonding

ES – Enzyme-Substrate

DME – Dimethoxy Ethane

TRIS – Tris(hydroxymethyl)aminomethane

PMMA – Polymethyl methacrylate

TON – Turnover number

TMM – Transfer Matrix Method

$C{=}O_{str}$ – Stretching frequency of carbonyl in all molecules

$O\text{-}H_{str}$ – Stretching frequency of water

HRMS – High-resolution mass spectroscopy

Preface

Selective vibrational excitation using lasers has introduced coherent, site-selective and mode-selective chemistry. Here, the conversion efficiency is poor due to the availability of internal vibrational relaxation pathways within the molecule. Selective and collective vibrational excitation is possible by coupling a fundamental vibrational transition to a confined electromagnetic field of a cavity. This phenomenon occurs in the absence of external photons (external stimuli) at room temperature. It offers a unique way to activate or deactivate a chemical bond in a ground state chemical reaction. This new research area that studies chemical reactivity under strong light-matter coupling is known as *polaritonic chemistry*. Strong coupling is typically achieved by placing molecules in an infrared micro-cavity resonator which couples the vibrational transition to the cavity mode. Collective coupling of Avogadro number of vibrational resonators results in large Rabi splitting energy that can affect the potential energy landscape of the reacting molecules. According to quantum electrodynamics, a molecular state is dressed by the confined electromagnetic field resulting in vacuum Rabi splitting. The notion of zero-point energy is invoked here. VSC has been shown to accelerate or retard the chemical reactivity of various organic and biomolecular reactions. Furthermore, VSC is not only a tool to control chemical reactions but also gives insight into which vibrations are involved in a reaction.

In the current thesis, we focus on the influence of vibrational strong coupling (VSC) that can control chemical reactivity by site-selective/band-selective coupling of vibrational states. In the **chapter 2,** for the first time, we discussed the idea of cooperative VSC between the solvent and reactant molecules that can catalyze a chemical reaction (aka-*cavity catalysis*). Solvolysis of *para*-nitrophenyl acetate enhances reaction rate by resonant coupling to $^{12}C{=}O$ stretching mode of ethyl acetate molecules. The thermodynamics suggest that solute-solvent interaction is modified under VSC due to the reshuffling of activation parameters. In **chapter 3,** the same concept is applied to study the structure-reactivity behavior under cooperative VSC conditions. Interestingly, resonant coupling shows a non-linear behavior in the Hammett plot suggesting a drastic electron density variation at the C=O active site. Various control experiments, both in cavity and non-cavity, show the role of solvent vibrational overlap has a major influence on chemical reactivity. Further studies suggest that the mechanism of the reaction remains the

same under strong coupling conditions. In **chapter 4,** we look into the behavior of biomolecular reactions under VSC. Here, the role of water molecules in an enzymatic reaction has been studied in cooperative VSC conditions. The catalytic efficiency has been increased by more than seven times at the ON-resonance condition without affecting the reaction mechanism. It indicates that competitive catalysis can be achieved by vacuum field coupling. A general conclusion is drawn in **chapter 5**, that VSC can control a chemical reaction without any external stimuli at room temperature. Our attempts here open a new and novel spectroscopic tool to understand the nature of a chemical bond and its reactivity.

Chapter 1

Introduction:

Light-Matter Interactions

1. 1 Motivation

A vacuum state does not mean a "state of nothing," instead, it contains an oscillating electromagnetic field with zero-point energy. It first appeared in Planck's theory of blackbody radiation and Einstein's theory of molecular agitation at zero temperature (theoretically) in 1911 and 1913. In quantum field theory, the vacuum state contains the feature of energy fluctuations even in the absence of real photons. Vacuum energy influenced the physical properties of matter and was a hot topic of interest in the early $1950s$. The question arises- Does this field have any effect on an atom? Dirac is the first person to derive the theory applied to the interaction of an assemble of light-quanta with an ordinary atom. The spontaneous emission rate in his quantum theory of radiation is later called quantum electrodynamics (QED).[1] Here, Dirac assumed that spontaneous emission occurs due to the availability of infinite vacuum states in space. van der Waals force is a very familiar concept in physics and chemistry. In 1930, Fritz London showed that the fluctuating dipole moment of two atoms or molecules leads to the long-range interaction energy of r^{-6} (r is the distance between two-particle).[2] In molecular physics, at any moment, the electron density not being uniform through the atom (or molecule). That creates a weak dipole moment and changes quickly all along the time. So, each inhomogeneous distribution creates an induced dipole moment that can interact with the ones of neighbour's atoms or molecules, and consequently, a force appears between the molecules. In 1948, Casimir introduced a similar thought in terms of fluctuating electromagnetic field that opens up a new array of phenomena known as the Casimir effect.[3] The effect of two uncharged metallic plates placed parallel to each other in a vacuum and that will start attracting each other is similar to the van der Waals force between the neutral molecules. Later, it also appears that the Casimir effect can be either attractive or repulsive. It depends on the nature of the field and geometrical features. In 1955, Lamb won the Nobel prize for the concerning discovery of the fine structure of the hydrogen spectrum.[4] He probed the interaction between the vacuum energy fluctuations and the hydrogen electron in different orbitals. The shift in the energy levels arises from the emission and absorption of the virtual photons and gives depth to our understanding of electromagnetic theory.[5]

1. 2 Light-Matter Interactions

a) Weak Interactions

Spontaneous emission is ultimately responsible for most of the light around us, and it is not the isolated property of an atom but an atom-vacuum system. In 1946, E.M. Purcell suggested the radiative rate constant and spontaneous emission rate of a radiating dipole can be controlled by coupling to an electromagnetic field (Figure 1.1 b).[6] An ability to enhance the spontaneous emission rate of an emitter in a weak coupling regime would allow the fabrication of a high-efficiency device.

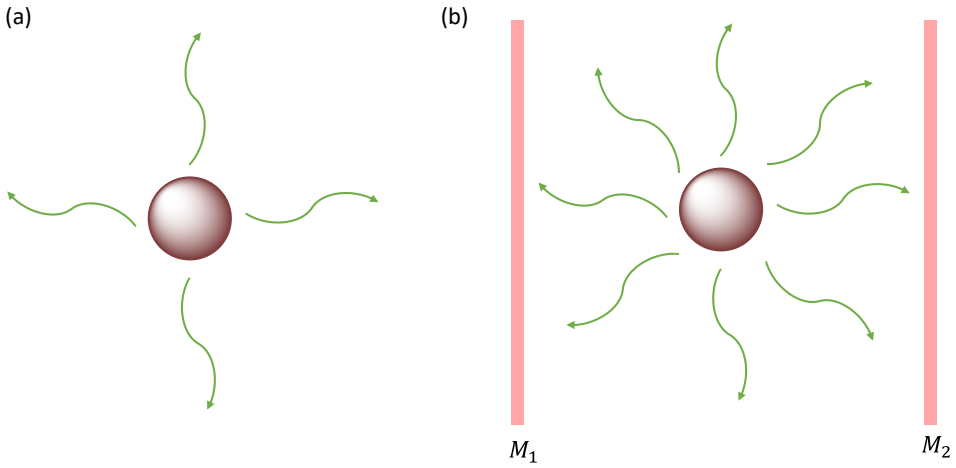

Figure 1. 1. Purcell enhancement of spontaneous emission. (a) in free space; (b) weak coupling to a cavity mode will enhance the spontaneous rate of emission by increasing the local density of modes (M_1 and M_2 representing mirrors).

Kuhn and co-workers were looking for a novel method of electronic energy transfer over a long distance, like the energy transfer from the excited donor to a nearby acceptor.[7] If the excited dye molecule is considered an oscillating dipole on the metal substrate, then the electric field reflecting from the mirror surface interacts with the dipole. The mirror influences the fluorescence emission of the organic dye deposited on the dielectric films. By varying the thickness of the dielectric film layer, it observed that oscillation in the lifetime of the dye. Here, the metal acts as an acceptor and absorbs at the fluorescent wavelength. In the early $1970s$, Karl H. Drexhage showed very clearly the effect of local variation in an electromagnetic field and a fluorescent dye molecule when the molecule is placed perpendicular to the surface.[8] Some groups discovered that the surface plasmons modes between the metal-dielectric interface were responsible for energy absorption.[9]

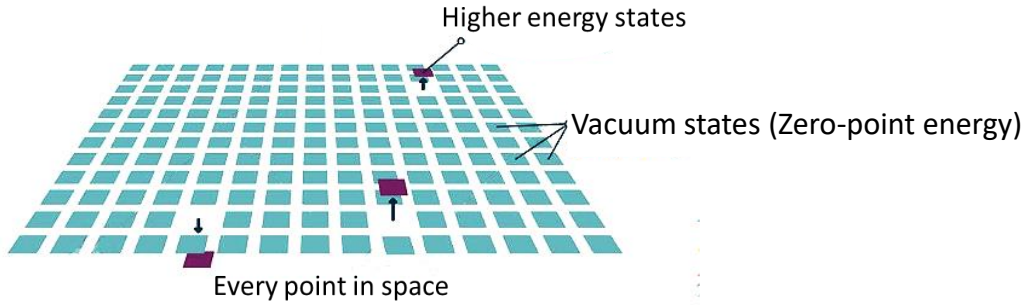

Figure 1. 2. Infinite vacuum states are available in space with zero-point energy.

An electromagnetic field occupies every point in space and the lowest energy state of the field is quantized, known as vacuum (Figure 1.2); it acts as a reservoir. In the QFT theory, it described that the properties of the vacuum are analogous to the properties of the ground state of a quantum mechanical harmonic oscillator. The vacuum field describes an infinite number of harmonic oscillators, and the ground state of each oscillator has its own "zero-point energy" associated with the vacuum fluctuations. The vacuum electric field amplitude E_0 in a mode of frequency ω is given in equation 1.1:

$$E_0 = \sqrt{\frac{\hbar\omega}{2\varepsilon_0 v}} \qquad [1.1]$$

ε_0 vacuum permittivity, v volume of an electromagnetic field. The coupling of an atom to each field mode is described by the so-called Rabi frequency (Ω_R) of the vacuum- is the frequency at which the atom and the field (a single mode of field) exchange energy.

$$\Omega_R = \frac{d.E_0}{\hbar} \qquad [1.2]$$

d transition electric dipole of the atom defines as the strength of interaction between the initial and final state of transition. The probability of photon emission per unit of time was given by the Fermi golden rule, which states that the rate of spontaneous emission (Γ) is depends upon the density of states $\rho(\varepsilon)$ of the coupled electromagnetic field. Inside the cavity, spontaneous emission enhances because the density of the state increases compared to free space (Figure 1.3 a, b).

$$\Gamma = \frac{2\pi}{\hbar} \left|\vec{d}.\overrightarrow{E_0}\right|^2 \rho(\varepsilon) \qquad [1.3]$$

This irreversible process leads an atom to the ground state, and the vacuum field acts as a reservoir. However, since $1990s$, different microcavities providing photon confinement have been developed.

b) Strong Coupling

In 1983, Haroche observed the formation of new hybrid states in the millimeter-wave regime for the Rydberg atoms of sodium coupled to the Fabry-Perot (FP) cavity.[10] This effect can be generalized to many atoms. It is possible to couple N identical Rydberg atoms and study their collective behavior.[11] Here, $N = 2{,}000\ to\ 40{,}000$ atoms are used for studying the collective behaviour. Due to strong interaction, the dynamics of the radiative relaxation altered compared to uncoupled system. Collective coupling creates Rabi oscillations on the time frame (Figure 1.3 c) of reversible energy exchange between the field and the atoms at the enhanced rate $\Omega_R\sqrt{N}$.[10] A few years later, Kimble explored for the quantum dynamical processes for single and many atoms with the high finesse optical cavity of spherical mirrors.[12] Laser cooling and other technique allowed the creation of ultracold gases, where one can achieve coherent behavior of a macroscopic cloud of atoms.

The mode structure in a vacuum can be altered when the cavity size is comparable to the wavelength. An excited atom confined between two parallel mirrors become infinitely long-lived if the distance between the mirrors is less than the wavelength. The resonance interaction between the molecular transition and confined electromagnetic field is widely known. The interaction is strong enough by coherent energy exchange between field and molecule, which reverses. Then the two new hybrid light-matter states are formed and separated by Rabi splitting energy; the system enters into a strong coupling regime (Figure 1.3 c; 1.4). The phenomenon leads to the formation of new polaritonic states $P+$ and $P-$ called upper and lower polaritons, respectively. Jaynes-Cumming two-state model defines the Rabi splitting energy depending upon the other variables given in equation 1.4.[13]

$$\Delta E = \hbar\Omega_R = \sqrt{4g_n^2 - (\kappa - \gamma)^2} \qquad [1.4]$$

ΔE energy difference between $P+$ and $P-$; κ and γ decay constants of the photon and excited state of the molecule. κ is the inverse of the lifetime of a photon in the empty cavity, γ is the inverse of the lifetime of the excited state of a molecule in open space. g is the interaction

energy between the electric component of the field and the transition dipole moment. In the absence of any dissipation, Rabi splitting energy is written as:

$$\hbar\Omega_R = 2g_n = 2\ d.E_0 = \ 2\ d\sqrt{\frac{\hbar\omega}{2\varepsilon_0 v}} \times \sqrt{n_{ph}+1} \qquad [1.5]$$

ħω is the resonant energy and n_{ph} is the number of photons involved in the coupling. Strong coupling can even be possible in the dark, which means no external source of a photon in the cavity, known as vacuum Rabi splitting. In this condition, coupling occurs due to the molecular transition and electromagnetic vacuum fluctuations with zero-point energy. An additional condition for strong coupling that needs to be satisfied is $\frac{\kappa+\gamma}{2} < \hbar\Omega_R$. The central idea to design large splitting energy can be observed by keeping the mode volume v minimum to reach maxima of E_0 and transition dipole moment d high as possible. It is important to note that all the molecules placed inside the cavity do not undergo coupling to the electromagnetic field. The coupling of the molecule depends on the orientation of the transition dipole moment with the electric field. The interaction is maximum when the cavity is resonant with the transition dipole of the molecule, and the two new peaks can be seen in the absorption spectra. As expected, this interaction becomes less pronounced as one move away from the bare molecule transition energy.

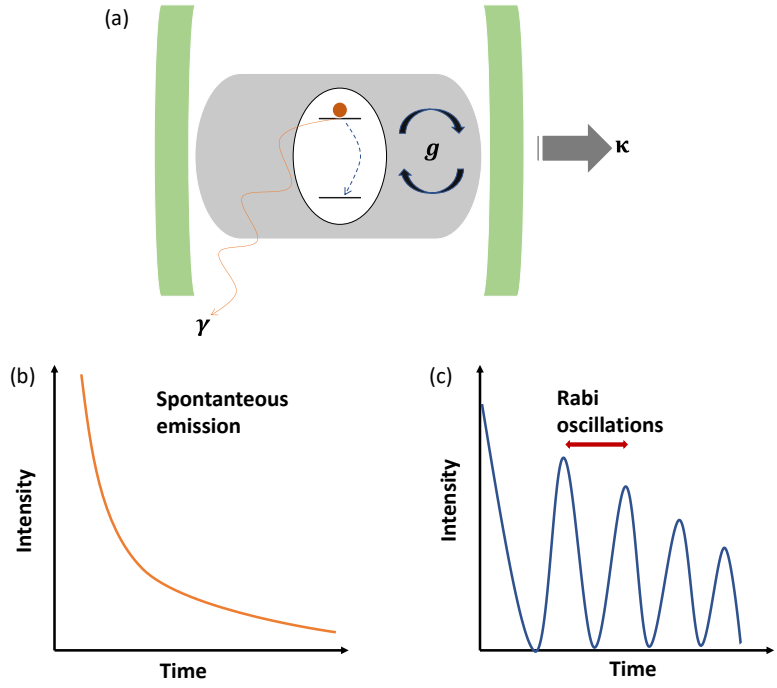

Figure 1.3. (a) Schematic illustration of the weak and strong coupling between the optical cavity and molecular transition; (b) weak coupling results in the spontaneous emission $\kappa + \gamma > 2g$; (c) strong coupling results in Rabi oscillation $\kappa + \gamma < 2g$.

Conventionally to achieve strong coupling, the new hybrid states must be separated more than the full-width half maxima (FWHM) of both molecular absorption peak and optical mode. The coupling strength is such that the Rabi frequency is a significant fraction of the transition frequency ($\sim > 10\%$) of the system that enters into the ultra-strong coupling regime. A large number of molecules enhances the value of Rabi splitting $\left(\hbar\Omega_R \propto \sqrt{C}\right)$. Therefore, it contains collective states; C is the concentration of the molecule in a mode volume (Figure 1.5). The coupling of N molecules generates $N + 1$ collective states in which only two states $P+$ and $P-$ are detectable. $N - 1$ are optically inactive states called '*dark states'* and have an important influence on the relaxation pathway in a strongly coupled system. Dark states cannot be directly excited with light and therefore cannot be seen in an absorption spectrum.[14] After excitation to the upper polaritonic state, relaxation happens in the dark state faster than the emission process because of the large number of dark states explained by the Fermi golden rule.

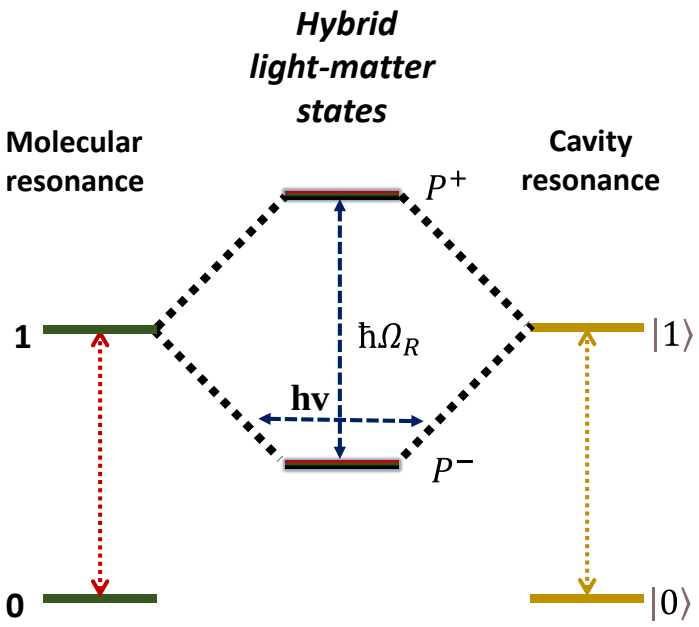

Figure 1. 4. Schematic diagram of between a molecular transition and a cavity resonance, in which two hybrid light−matter states $P+$ and $P-$ are formed and are separated by the so-called Rabi splitting energy $\hbar\Omega_R$. (Ebbesen et al. 2016)

An essential property of the polaritonic states is their dispersive nature inherited from the photonic component. The molecular transition energy is constant for all angles and shows wavelength independence. The photonic mode has dispersion and varies with the angle of minimal at normal incidence (Eqn. 1.6). In-plane wavevector is related to the wavelength and angle of incidence through:

$$k_{\parallel} = \frac{2\pi}{\lambda} \sin\theta \qquad [1.6]$$

Incident angle in light-matter interaction is detuned to reveal the hybrid state dispersive nature. When the ON-resonance condition is reached, two branches of hybridization repel each other and become equal in energy from the fundamental transition. The effect observed is known as anti-crossing behavior. The minimum value of energy separation between two new hybrid states determines the Rabi splitting energy ($\hbar\Omega_R$). Energy curves diverge from each other as detuned from the cavity energy coincides with the transition energy of the molecule.

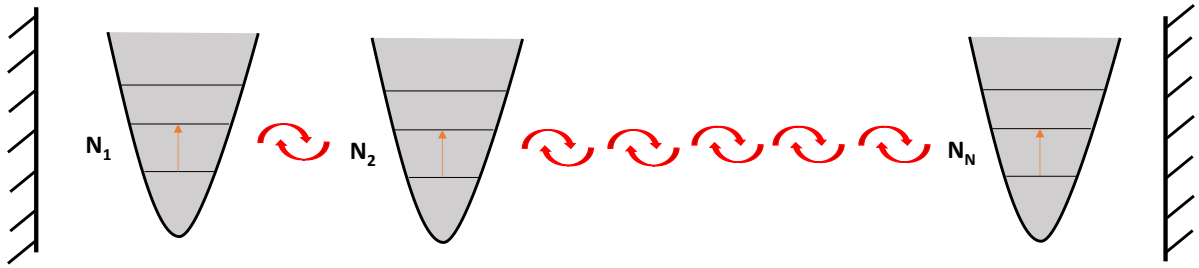

Figure 1. 5. Collective coupling (VSC) of N oscillators with the optical mode.

All molecular (studied electronic and vibrational) transitions allowed to couple with the cavity mode and form polaritonic states. In the early $1990s$, the report on strong coupling observed the Rabi splitting in the order of 1-10 meV, especially for inorganic semiconductors at cryogenic temperature.[15] In 1998, giant Rabi splitting energy was reported of the order of 100 meV for the organic excitons such as J-aggregates.[16] The major advantage was the use of organic dye molecules in an FP cavity configuration at room temperature. This splitting was more significant in the case of thin films of cyanine dye-forming J-aggregates placed in a microcavity formed by two-silver layers.[17] The cavities based on the dielectric mirrors arise due to the tight confinement of the field. In 2004, a single quantum dot reached a strong coupling regime by interacting with the photonic crystal that displayed anti-crossing between the quantum dot's first exciton band and a photonic mode.[18] The concept of strong light-matter interactions and the formation of polaritonic states are well established in the late $90s$, whereas its applications in chemistry are less explored.[19–24]

1. 3 Coherent Control of Chemical Reaction and Light-Matter Coupling

Manipulating the yield of a chemical reaction is at the heart of chemistry, and the concept underlying coherent control of chemical reactions has been the goal for years. The practical purpose of this process is to control unwanted side products in a multi-path chemical process.

If the desired products are kinetically favored, it is possible to change the experimental conditions (pressure, temperature, pH) to maximize the yield of the product. A challenge arises if the desired product is not dynamically favored. Different approaches are used to lower the reaction barrier, such as chemical catalyst or photocatalysis, to alter the reaction pathway.

Early development in chemical kinetics was the universal description of the rates of a chemical reaction proposed by Svante Arrhenius (1889), but this does not provide a detailed molecular picture of a chemical reaction. In 1931, Henry Eyring provided the potential energy surface (PES) calculation for $H+H_2$ and described the reactant's nuclei journey to a product passing through the transition state (TS). In 1935, Eyring, Evans and Polanyi formulated the transition state theory. According to this, the fastest reaction is given by kT/h which is the frequency for the passage through the TS. Later stopped-flow method was used as a technique in which two reactants were mixed in a flow tube and observed the product at different distances. It is one of the classical ways by knowing the speed of flow; one could translate this into time. Later, B. Chance came with the millisecond time scale, and the stopped-flow method is still used in biological studies. A molecular collision occurs less than a picosecond's timescale; at that time, real-time studies were not possible. Around 1950, a technique of George porter reached a microsecond time scale and the work shared the Nobel prize in 1967.[25] They provided an intense burst of a coherent laser and created radicals in the sample, and used white light for the recording of the spectra. This process allowed us to visualize the relatively stable intermediate. In the $1960s$, picosecond resolution made it possible to study photophysical rates of internal conversion and novel approaches for measuring vibrational relaxation channels in a chemical reaction.

In 1989, D. W. Schumacher and co-workers published work on a laser-induced coupling of the electronically excited states and softening the molecular bond.[26] H_2^+ molecular ion was formed in an above-threshold ionization of H_2 gas irradiated by intense laser light. This induced deformation of the internuclear potential is due to the strong laser field. These experiments help to study the energy level of H_2^+ as a function of laser electric field strength or the component of the field along the internuclear axis. All the molecules get dissociated at high intensities, producing randomly oriented molecules with high energy. Therefore, higher vibrational states become unbounded as the molecule rotates into the alignment with the polarization. Intense field intensity is necessary to lower the energy of the crossing to permit the vibrational state and come onto resonance with the predissociation state. At 3.5 TW/cm^2 the $v = 6$ level is no

longer bound. As the laser intensities crosses 50 TW/cm^2, most of the vibrational levels in the manifold are unbound that result in bond breaking (Figure 1.6).

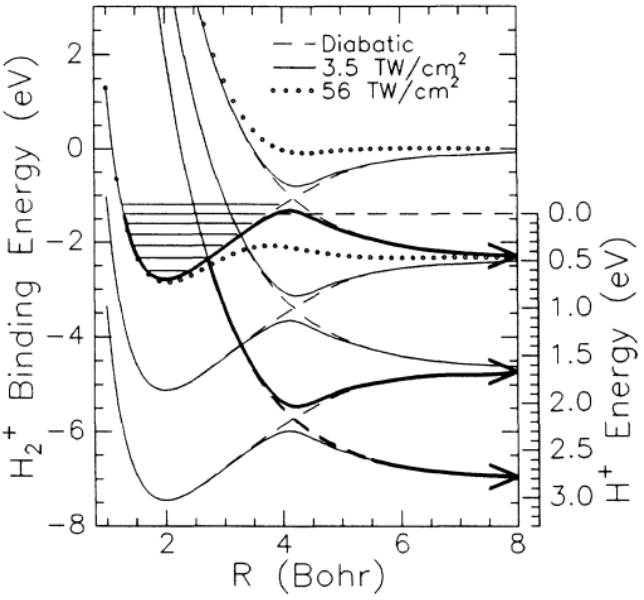

Figure 1. 6. Floquet calculation for the H_2^+ molecular potential deforms in the presence of intense light with two intensities at 3.5 TW/cm^2 and 56 TW/cm^2. (Schumacher et al. 1989)

In another set of experiments, George C. Pimental used his state-of-the-art chemical lasers to study resonant pumping into fundamental and combination vibrational states.[27,28] It was the study of a bimolecular reaction of C_2H_4+F_2 show an increase in the conversion yield by selective single-photon excitation processes. The kinetic growth of the product was studied by selective irradiation of vibrationally states. The product absorption of CH_2=CHF.HF at 1119 cm^{-1} versus time for irradiation of two C-H stretching modes v_{11} and v_9 at 2989 cm^{-1} and 3105 cm^{-1} respectively shown in figure 1.7 and also plot the growth curves for excitation of combination $v_2 + v_{12}$ at 3076 cm^{-1} and $v_3 + 2v_7 + v_{10}$ at 4209 cm^{-1} respectively. The general feature observed is the increase in the quantum efficiency with the energy per exciting infrared photon. The observed difference in the quantum efficiency with a factor of 250 between out-of-plane CH_2 wagging mode v_7 and combination $v_7 + v_8$. Both of the vibrational transitions involve similar vibrational motions, so it was expected that this effect is not to be expected with mode-specific effects. More interestingly, the steep quantum yield associated with $v_7 + v_8$ at 1896 cm^{-1} is smaller than the v_{11} at 2989 cm^{-1}. It is postulated that $v_7 + v_8$ mode is an out-of-plane motion that significantly distorts molecular planarity, which should contribute considerably to the reaction coordinate. In contrast v_{11} mode, only in plane C-H stretching motion that can hardly be influential in an addition reaction. Hence, it looks pretty excited, with two different quantum yields directly showing mode specificity.

These prototypical experiments show control of molecular reactivity of C_2H_4 upon excitation of in-plane C-H stretching motions: v_9 and v_{11} is a mode-to-mode relaxation process of the vibrational energy while IR photon excitation in cryogenic conditions. Thus, the general upward trend follows the quantum efficiency, which is five orders of magnitude over a photon range of 953 to 4209 cm^{-1}. Each measured value is the sum of the quantum efficiency of the mode excited and the quantum yields of all the cascading relaxation processes. The product branching between 1,2-difluoroethane and vinyl fluoride was found to be the same for all the vibrational transitions between 1896 and 4209 cm^{-1}. The isotopic effect of HF/DF branching ratio of the reaction F_2 with CH_2CD_2, trans-CHDCHD, and cis-CHDCHD was determined to be 1: 1, independent of the precursor $C_2H_2D_2$ isomer and particular mode excitation in the reaction. This result indicates that product branching occurs by $\alpha\beta$ elimination of HF/DF from the vibrationally excited, electronically ground state 1,2-difluoroethane intermediate. It is influenced by the selection rule that undergoes the significance of the intramolecular vibrational process and correlates with molecular symmetry. The experiments were performed

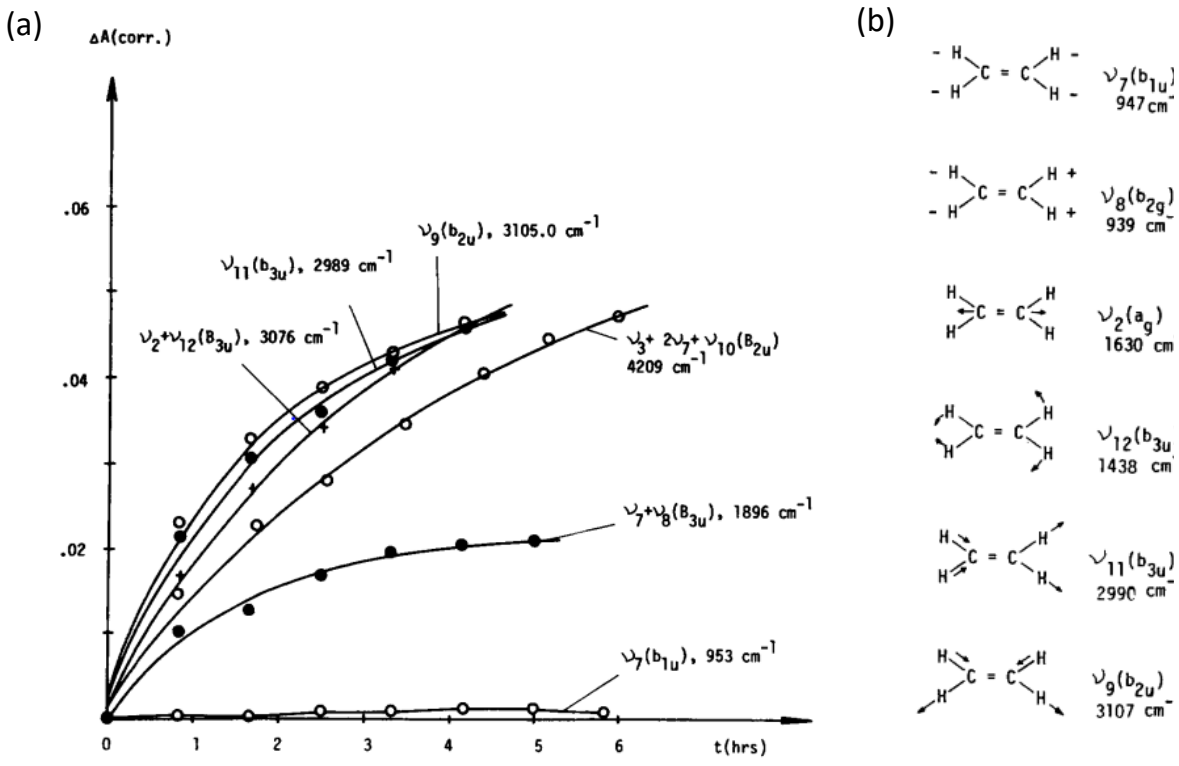

Figure 1. 7. (a) $C_2H_2/F_2/N_2$~1/1/100: growth of product absorption versus time, corrected for growth 1119.1 cm^{-1} during spectroscopic exposure; (b) Different vibrational modes corresponding to C_2H_2. (Pimentel et al. 1989)

at cryogenic temperatures as they suppressed the thermal reaction and achieved single-photon vibrational excitation without rotational and translational excitation.

R. Zare and co-workers (1982) proposed the stereo-dynamic control by colliding two beams of reagents by applying an external field.[29–31] The open-shell reagent demonstrated the reactions of electronically excited calcium atoms with various halogen-containing compounds. The orientation and alignment of one reagent with respect to another are achieved, and the absorption of linear polarized light controls angular momentum direction. These studies have shown the reaction rate can be changed by less than an order of magnitude and provides a way of probing the reaction pathways.

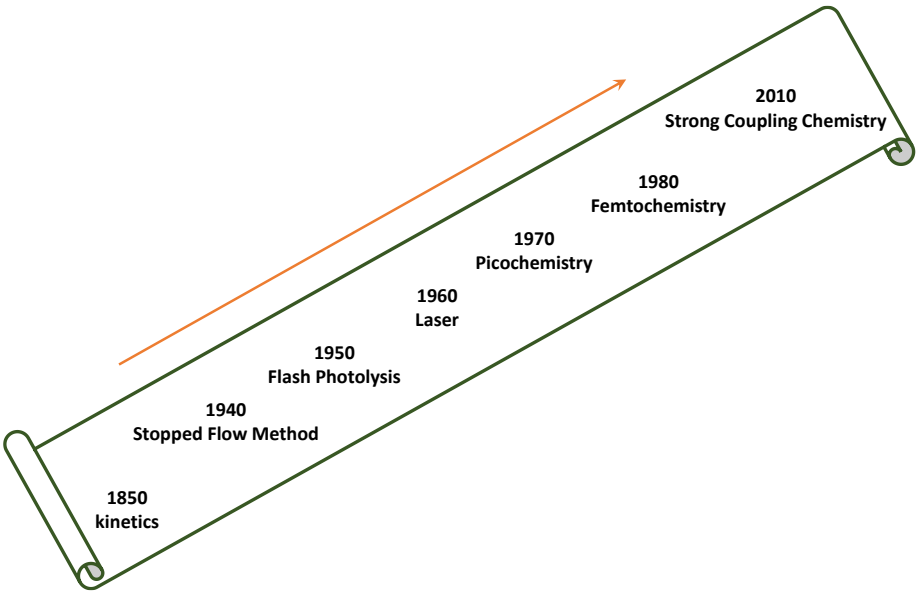

Figure 1. 8. Evolution to study chemical reactions by different methods.

Another experiment by Crim et al. was the vibration excitation of either O-H or the O-D bonds to enhance the H+HOD reaction selectively.[32] Vibrational overtone excitation experiment used the light from a Ti: sapphire laser to excite overtones of either the O-H or the O-D stretching vibrations in a low-pressure containing HOD, reacted the vibrationally excited molecules with hydrogen atoms produced in a microwave discharge, and detected the OH or the OD products by laser-induced fluorescence with ultraviolet light from a frequency-doubled dye laser. When the O-H bond is excited, the reaction forms a more branching ratio of H_2+OD, and when O-D is excited, more ratio of HD+OH product is formed. It shows that vibrational excitation of the O-H stretch in HOD causes at least a 220-fold excess of the OD product over the OH product. Vibrational excitation of the O-D bond in HOD leads to at least a 200-fold preference for its cleavage, as the presence of essentially only the OH fragment. The vibrational excitation breaks that bond preferentially in the bimolecular reaction. O-H and O-D maintain the local nature of excitation because of significant frequency differences and need not worry about intramolecular vibrational relaxation (IVR). Bond-selected chemistry using light is a practical

reality that rests on the simple concept of exciting a vibration in a molecule that becomes the reaction coordinate in a bimolecular reaction. These studies show that the mode of internal excitation controls the reaction outcome.

In the past years, a chemical reaction was studied by utilizing the coherent properties of laser light to influence the motion of electrons and nuclei. Tannor and Rice utilized the time domain and ultrashort light pulses to create a wave packet of molecular eigenstates.[33] They used ultrashort $(70 - 110\ fs)$ laser pulses for the experimental demonstration to ionize the Na_2 molecule. It found that the ratio of molecular to atomic ion products oscillates with the delay between the laser pulses with a period determined by wave packets motion. Brumer and Shapiro put forward the frequency domain-phase control of a molecular scattering event. The idea is to excite an atom/molecule by two coherent light sources that lead to the same upper state from which various processes can occur, such as ionization/ dissociation. The essence of the coherent radiation control approach is to utilize the phase and intensity properties of the laser excitation to alter the production of the desired product is enhanced.[34–37] Later, a computational study on the photodissociation of IBr to produce I+Br and I+Br* with a high-quality potential surface calculation was conducted to understand reaction dynamics in the ultrafast time scale. Contour plot of Br yield as a function of the relative laser pulse and amplitude results show that control on the product yield ranges from $25 - 95\%$. Gordon and co-workers conducted experimental verification of the same system.[38] The excited molecule DI molecules were delayed either by atomization to produce DI+ or by predissociation to produce a ground state D atom and an electrically excited I atom. Later, additional photon absorbs and produces I+. The oscillating ion signals were offset one from the another by a constant phase lag so that I+ to DI+ ratio can be controlled by varying the phase difference between two laser beams.

Zewal et al. in 1992 reported using laser pulses of femtosecond duration that, it is possible to probe the nuclear motion of the formation and breakup of the transition state (TS). The first application of femtosecond transition state spectroscopy (FTS) was to study the dissociation of ICN.[39] Reaction trajectory leads to the TS, the potential energy window, and measurement of the process's lifetime with femtosecond resolution opens a new era for chemical reaction dynamic studies. Later, Dan Imre et al. calculated the influence of wave packet motion and observed FTS transients. They described such control of chemical reaction using two sequential coherent laser pulses. Finally, all the dissociation reaction dynamics of NaI were orchestrated, and the resonance behavior of a bond converting from being covalent to being ionic along the

reaction coordinate was picturized. The vertical transition from ionic to covalent surface ($V_0 \rightarrow V_1$) after absorption of the pump photon in NaI is shown in figure 1.9. As the molecule falls apart, it encounters the level crossing of these two surfaces, and it is expected that FTS results in the coupling of potential surfaces of these systems.

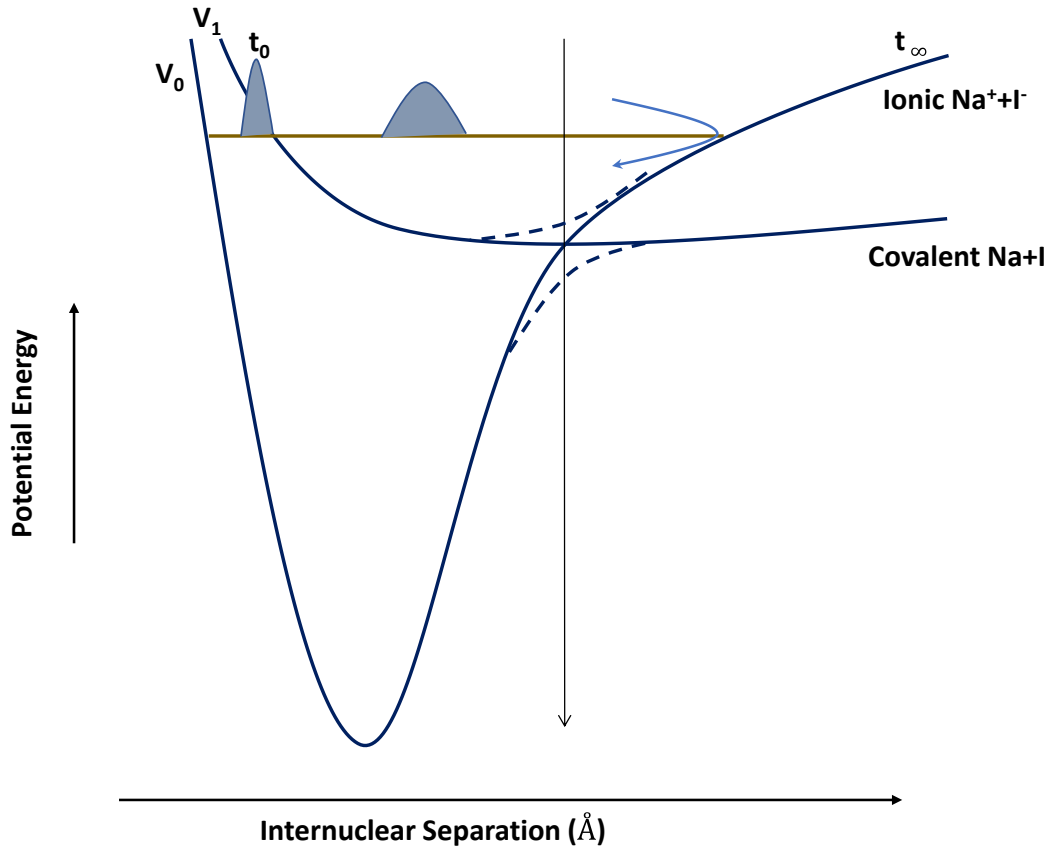

Figure 1.9. A display of the PES involved times $t_0 \rightarrow t_\infty$ refers to the evolution of the wavepacket as it moves along the coordinate and broadened by dispersion. (Zewail et al. 1988)

The appearance of an oscillation in FTS indicates that some NaI molecules were trapped in a well-formed by the avoided crossing of covalent and ionic PES. The damping gave the probability of escaping out of the well. The wave packets were highly delocalized in the space ~0.1 Å, and the spreading of the wavepacket was minimal up to a few picoseconds. An apparent vibrational coherence during the reaction trajectories from the reactant to the product is observed in the experiment. By changing the probe wavelength, one can effectively study the dynamics of the dissociative process at different positions of the reaction coordinate. Comparing the ON and OFF resonance and tuning of the probe wavelength shows that the ON-resonance signal shows an initial sharpen rise with a series of stair-stepped plateaus. At the same time, the OFF-resonance displays a damped oscillation. The probe is kept at 589 nm, (it is resonant with the sodium D-line transitions) resonance situation arises. For the OFF

resonance probe, the wavelength in figure 10 b is not enough to eliminate the ON-resonance contribution (Figure 1.10).

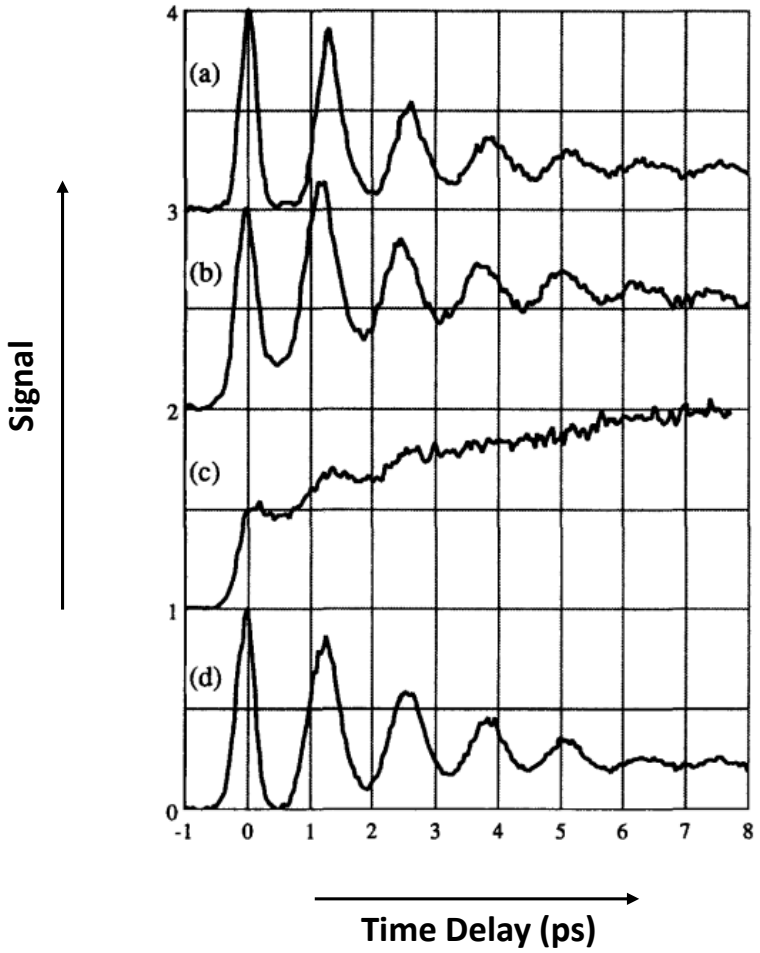

Figure 1. 10. FTS results for NaI as a function of probe wavelength; (a) 575 nm (b) 580 nm (c) 590 nm and (d) 615 nm. (Zewail et al. 1989)

Consequently, the signal does not decay at 575 nm and 615 nm. The propagation of the wave packet generated from the pump oscillates back and forth across the well. The experimental result shows the parameter of the dynamics, such as the time of bond breakage and the covalent-ionic coupling magnitude. The reaction of iodine molecules with xenon atoms forms XeI by exciting the product through the TS. Modulation in the product yield is observed as the pulse's delay is varied. It controls a coherent femtosecond pulse that reflects the dependence on the nuclear motion of the reactants. These studies are a beautiful demonstration of understanding the complexity of reaction dynamics. However, few researchers argued that the molecule is too big to see quantum coherence effects among the vibrational states.[40–42]

1.4 Chemical reaction in strong coupling conditions

In the initial phase of the scientific advance, strong coupling experiments were mainly on atomic states and later with semiconductor physics.[12–25] Study on strong light-matter coupling on molecular states and its effect on the chemical reaction was first demonstrated by Thomas Ebbesen group at the University of Strasbourg. The first attempt was to couple electronically excited states of a molecule following a photoisomerization reaction.[43,44] A photochromic molecule-spiropyran (SPI) undergoes photoisomerization and generates an extended conjugation (merocyanine-MC) by UV radiation at 330 nm and as shown in figure 1.11 a.[43] MC formation results in strong absorption in the visible region (560 nm) and slowly the system reaches to a photostationary state (PSS). In order to achieve strong coupling, SPI (in a PMMA film) was sandwiched between two Ag mirrors. A thin layer of PVA film is used to avoid the direct contact of Ag mirrors with the photochromic molecule (Figure 11 b). The above geometry generates an FP cavity mode around 560 nm, having an overall thickness of 130 nm (PVA/PMMA/PVA) between the mirrors. This situation results in resonance with the forming MC molecules that resulted in the formation of hybrid states. A complete conversion of SPI to MC gives a Rabi splitting energy of 700 meV at the ON-resonance condition. Photoisomerization kinetics traces collected show a non-linear nature for non-cavity and cavity systems. The rates measured for the two systems are similar in the initial times, but later the reaction rate decreased significantly in the cavity. The kinetics analysis of the photoisomerization reaction shows that the rate retarded as the hybrid light-matter states formed. The final concentration of the species at the PSS is also modified, increasing the MC yield by 10 %. However, there is no change observed when the cavity is designed to be OFF resonance from the MC absorption transition and show very similar behavior as outside the cavity. The reaction rate altered under on-resonance conditions, thus slowing down the reaction. Strong coupling of the electronically excited state of the MC generates polaritonic states with new energy levels. This results in reshuffling the chemical reaction landscape, affecting the reaction rate and the quantum yield of a photoisomerization reaction.

Further, theoretical studies are done by several groups to understand the effect of strong coupling by calculating the potential energy surface (PES) of the polaritonic states.[135] First, this concept is applied to a photoisomerization reaction that shows suppression under a strong coupling regime.[45] Later, A. Rubio's group combined the idea of quantum electrodynamics and density functional theory to study the electronic, nuclear and photonic degree of freedom of the coupled system.[46] They explained that the reaction barrier increases due to the less energy

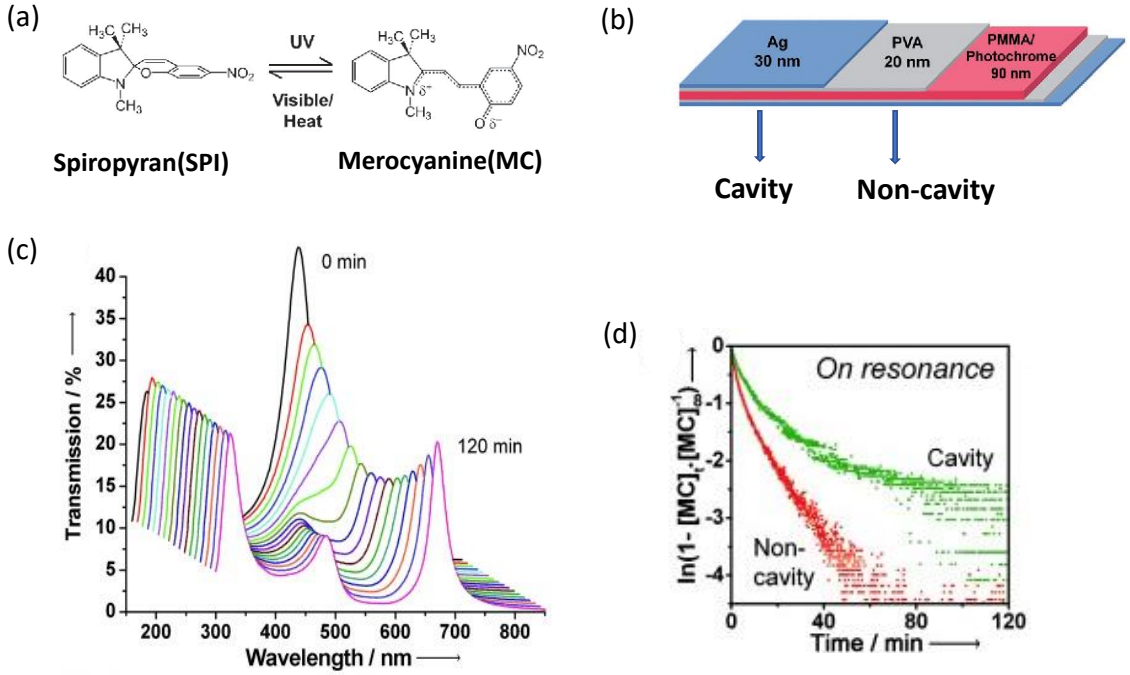

Figure 1. 11. (a) Structure of spiropyran (SPI) and merocyanine (MC); (b) Fabry-Perot cavity schematic diagram of the cavity (upper and bottom Ag mirror) and non-cavity (bottom Ag mirror) also measured from the same film; (c) Transmission spectrum of the coupled system in the cavity as a function of irradiation time at 330 *nm*; (d) Kinetics of the growth of the MC absorbance measured for the bare molecules (red) and the coupled system (green). (Thomas et al. 2016)

of lower polariton than the bare molecule. The same effects showed for the photobleaching of J-aggregates. Further studies are available in the literature on the effect of strong coupling and reduction in intersystem crossing etc., that can affect the photoconversion processes. Many groups focused on theoretical and experimental studies are based on coupling the electronic transition and its effect on excited-state reaction dynamics and the PES of the associated system.[47–52]

Strong coupling is not limited to electronic transitions (Figure 1.12). This thesis focuses on coherently coupling molecular vibrational modes of the ground state with a vacuum field that can generate symmetrical and anti-symmetric states, as mentioned in the previous section. The coherent nature of the single-mode cavity field drives all the coupled molecules in the same phase. It indues coherence among the molecule vibrations and an IR photon (cavity reservoir); therefore, macroscopic coherence is generated under vibrational strong coupling (VSC) conditions.[54–64] Electronic strong coupling provide a Rabi splitting energy ($\hbar\Omega_R$) in the range of 0.3-1.0 eV for organic molecules, and the same vibrational fundamental states can give

vibrational Rabi splitting ($\hbar\Omega_{VR}$) in the order of ~ 20-50 meV. Rabi splitting can still occur even in the absence of real photons due to interaction of the vibrational transition dipole and the cavity mode through zero- point energy fluctuations. This residual splitting is known as the vacuum Rabi splitting. Please note that there will also be an un-coupled population in the system that can be a large population in vibrational strong coupling experiments. To prove the idea of VSC, Ebbesen and co-workers (2015) experimentally demonstrated strong coupling of an IR photon with a thin polymer film in an FP cavity configuration.[53] Here, Polyvinyl acetate (PVAc) was chosen that has a sharp band feature of C=O symmetric stretching at 1740 cm^{-1}. The relatively high frequencies of molecular vibrational transitions fixed by the bond strength and the tiny atomic masses involved in the vibrations, lead to important features. Such molecular modes are in their ground state, allowing coherent light–matter coupling.

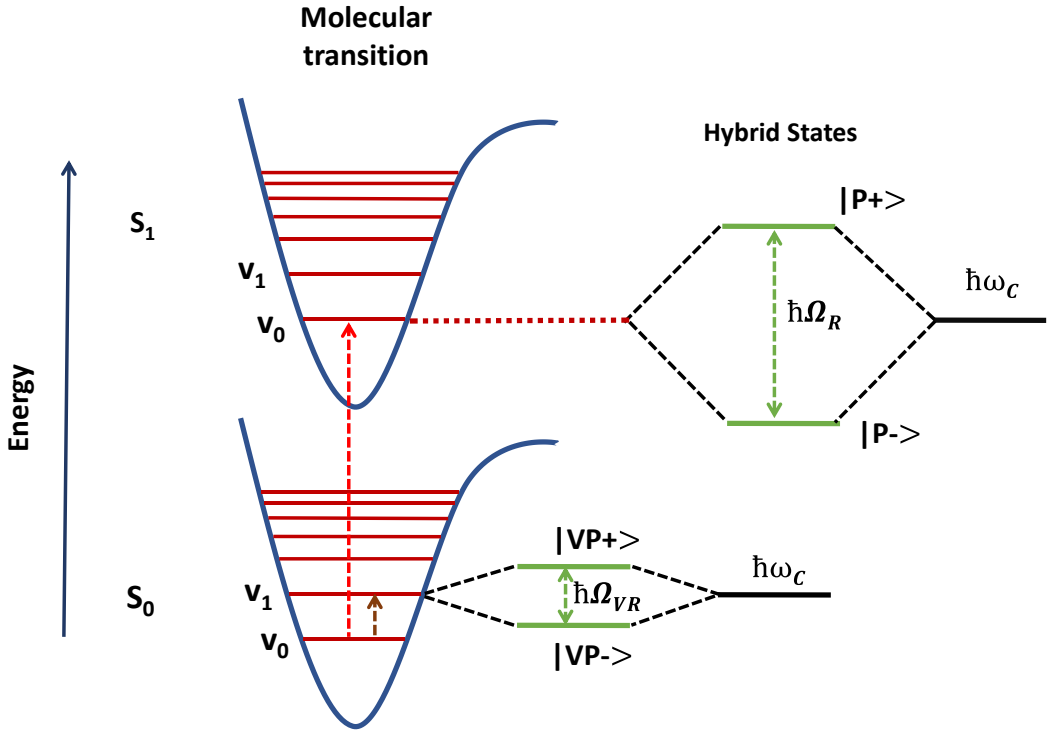

Figure 1.12. Strong coupling in electronic and vibrational transition; corresponding Rabi splitting energy represented by $\hbar\Omega_R$ and $\hbar\Omega_{VR}$.

Under ON-resonance conditions, new vibro-polaritonic states are formed with Rabi splitting energy of 167 cm^{-1}. Later in the same year, they investigated VSC in the liquid phase for various functional groups in the infrared (IR) region for the first time.[58] The key idea is that coupling molecules in the liquid state will allow us to investigate the various chemical reactions. IR absorption spectra of three different molecules studied under VSC, one of which is DPPA (diphenyl phosphoryl azide) isolated N=N=N stretching mode at 2169 cm^{-1} shows

Rabi splitting ($\hbar\Omega_{VR}$) of 127 cm^{-1} which is larger than the FWHM of the bare molecule band and cavity mode. The same investigated for C≡N of benzonitrile and C=O of citronellal. Liquid phase study of VSC gives rise to a fundamental difference in the rapid orientation of the molecule in solution and could increase a dephasing rate. So, to overcome the dephasing rate, later reported that the VSC can be controlled or tuned by the orientation of the molecules for a nematic liquid crystal.[64] They demonstrated the coupling of the C≡N stretching vibration of the liquid crystal by applying an external voltage to relate the molecular transition dipole and the electric field direction of the cavity. Here, a decrease in Rabi splitting energy from 57 to 39 cm^{-1} to the applied voltage was observed. It shows that the molecule's orientation switches from parallel to perpendicular to the cavity plane at the high voltage. Using in-plane polarized light parallel with the cavity shows this effect, whereas perpendicular to the cavity shows no change in splitting energy even when applied to high voltage. The overall goal of the experiment is to study the strength of the molecule field coupling depending on the angle between the molecule's transition dipole moment and electromagnetic field. This feature opens many exciting opportunities, such as site-selective chemistry targeting a given bond in a reaction. The electronic transitions are high in the energy that involve the delocalization of the electron over the entire molecule. Whereas the vibrational changes are localized and splitting energy ~ 10 % of the fundamental vibrations. So far, the concept of VSC studied on various systems involving solids and liquid phases, including polymers, organometallic complexes, liquid crystals, and proteins. Moreover, surface plasmon's strong coupling with the vibrational transition was also achieved.[65–69]

To investigate the idea of direct coupling of a given vibrational bond to influence the reactivity in the ground state has been a topic of interest in this field. For the first time in 2016, a desilylation reaction was performed of a pure reactant 1-phenyl-2-trimethylsilylacetylene (PTA) under VSC conditions.[70] PTA undergoes a base-catalyzed reaction with tetra-n-butylammonium fluoride (TBAF), in which an F^- ion attack on the silicon atom forms a pentavalent intermediate. The reaction follows pseudo-first-order kinetics, and traces are monitored by FTIR spectroscopy at different time intervals (Figure 1.13). The FP cavity consists of two parallel mirrors separated by a distance of 6 μm, and the screws on the top of the cell are used for preciously control to achieve the ON-resonant condition with a vibrational transition of a molecule. The reaction was monitored by tuning the cavity mode position and coupling with the C-Si bond at 860 cm^{-1}. The reactant and the product are different in their refractive indices; therefore, this affect the cavity mode position and the same is used for

determining the reaction kinetics. The value of splitting energy of 98 cm^{-1} ensure that VSC achieved is larger than the FWHM of both vibrational transition (Si-C) 39 cm^{-1} and respective cavity resonance 30 cm^{-1}. Another cavity mode falls exactly on C≡C vibrational mode at 2160 cm^{-1} but does not follow the criteria of strong coupling.

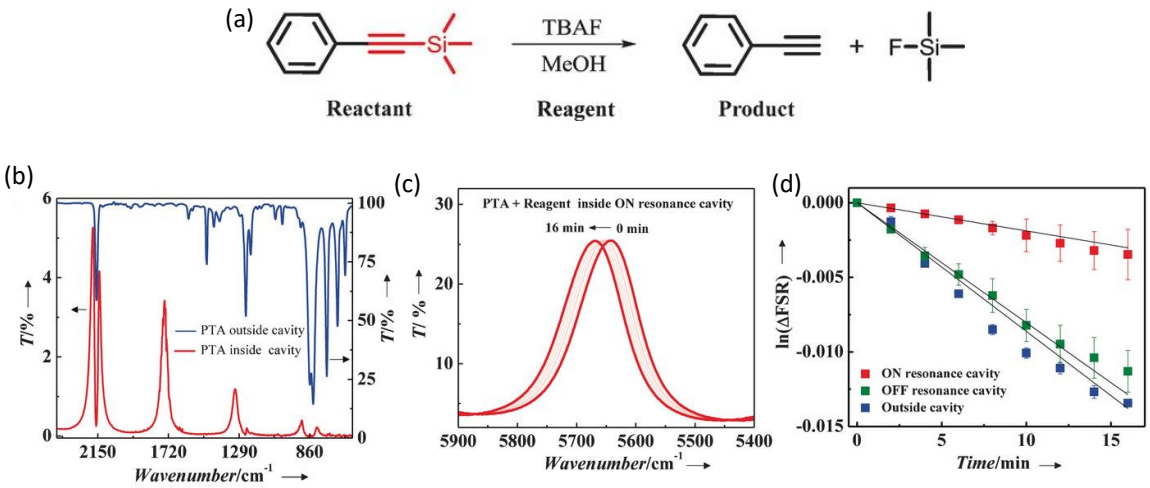

Figure 1.13. (a) Chemical reaction- Silane deprotection of 1-phenyl-2-trimethylsilyl acetylene in the presence of TBAF; (b) IR spectrum of PTA outside (blue trace) and inside ON-resonance (red trace) of the cavity; (c) Under ON-resonance shift on the higher order cavity modes; (d) Kinetic of the reaction ON-resonance (red squares), outside cavity (blue squares) and OFF-resonance cavity (green squares). (Thomas et al. 2016)

The reaction was initiated after mixing PTA with TBAF and immediately injected into the microfluidic IR cavity. A logarithmic plot in the shift of the higher mode position versus time gives a straight line and compares the cavity rates under different mode positions (Figure 1.13 d). Under VSC, the reaction rate decreased by a factor of 4.5, and the detuning cavity roughly gives the same rate as the non-cavity (Figure 1.14 a). It is interesting to note that the kinetic rate plot- a straight line does not deviate from its path as in the case of merocyanine-electronic strong coupling. Rabi splitting energy hardly changes in the desilylation experiment due to the presence of Si-C bonds in both the reactant and product molecules. Rabi splitting depends upon the number of oscillators and is directly proportional to the square root of PTA concentration. Further experiments are conducted by varying the Rabi splitting energy from 58 cm^{-1} to 114 cm^{-1} by increasing the PTA concentration from 0.87 M to 3.37 M. The retardation of the reaction under VSC increases with increasing coupling strength (Figure 1.14 b).

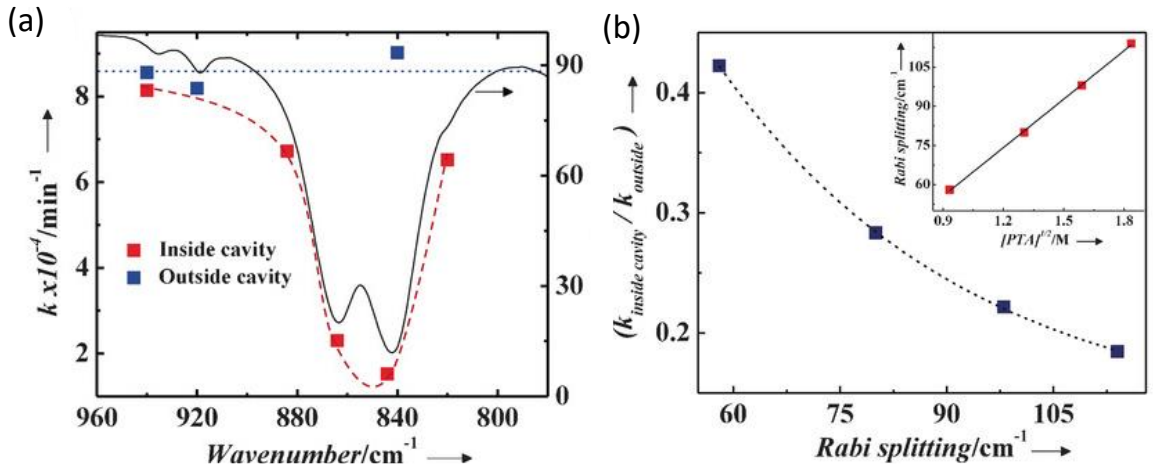

Figure 1. 14. (a) Reaction rate decreases as a function of the cavity tuning (red squares) and outside cavity (blue squares); (b) Decrease in the ratio of the reaction rates under VSC and outside cavity as a function of the Rabi splitting energy. (Thomas et al. 2016)

Thermodynamic parameters were extracted using the Eyring equation that allows us to understand the activation energy of the TS.[71] Reaction barrier increases under VSC as enthalpy of activation increased from 39 to 96 $KJmol^{-1}$ and the changed in the sign of enthalpy of activation from -171 to 7.4 $KJmol^{-1}$ as shown in figure 1.15. These suggest a modification of the TS from associative to dissociative pathway. It demonstrates that VSC can significantly modify chemical landscapes and opens a new way to control chemical reactions.

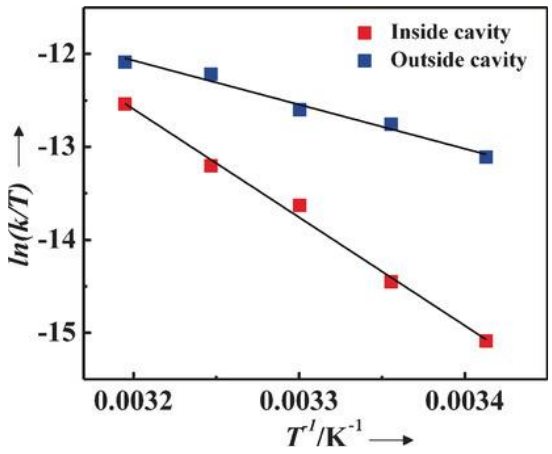

Figure 1. 15. Eyring plot for the reactions inside the ON-resonance cavity (red squares) and outside the cavity (blue squares). (Thomas et al. 2016)

VSC as a function of change in concentration of PTA is analyzed, which increases the Rabi splitting from 55 cm^{-1} to 128 cm^{-1}. The relative change in the reaction rate depends on the Rabi splitting energy, which is controlled by the reactant concentration. The corresponding enthalpy of activation doubled from 35 to 84 $KJmol^{-1}$ and changed its sign for the entropy of activation from -49 to -1 $KJmol^{-1}$. The difference between the total free energy change

under VSC and non-cavity is relatively minor because the enthalpy and entropy of activation compensate for each other. The change in the thermodynamic data is more significant than the Rabi splitting energy which is typically on the order of thermal energy ($k_B T$).

Another class of reactions that was studied is Prins cyclization under VSC of the carbonyl band of a series of aldehyde and ketone.[72] Here, a nucleophilic attack (C=O) on the carbonyl carbon of aldehyde or ketone determines the reaction rate. Under VSC, the reaction rate decreased by $2-5\ times$ depending upon the reactivity of C=O_{str} (stretching frequency of C=O) of different derivatives. The increase of the activation energy by VSC might suggest the effect of C=O stretching vibration decreases the polarity of the functional group involved in the rate-determining step. Prins cyclization has essential application in pharmaceutical chemistry. Modification of enzymatic reactions under VSC is also studied.[73] The coupling of the O-H_{str} band of water on the enzyme pepsin slows down the proteolytic activity. Vacuum Rabi splitting of O-H_{str} gives 700 cm^{-1} ; 21 % of the bare transition indicates the system is in ultra-strong coupling. The reaction constant k_{cat}/K_M was 4.5-fold decreased after VSC, whereas there is no effect of bending coupling. VSC of water affects the intermolecular interactions may be through H-bonding, van der Waals interactions, and hydrophobic interaction, leading to changes in the dynamics and enzyme-substrate interaction and the rate of the product formation.

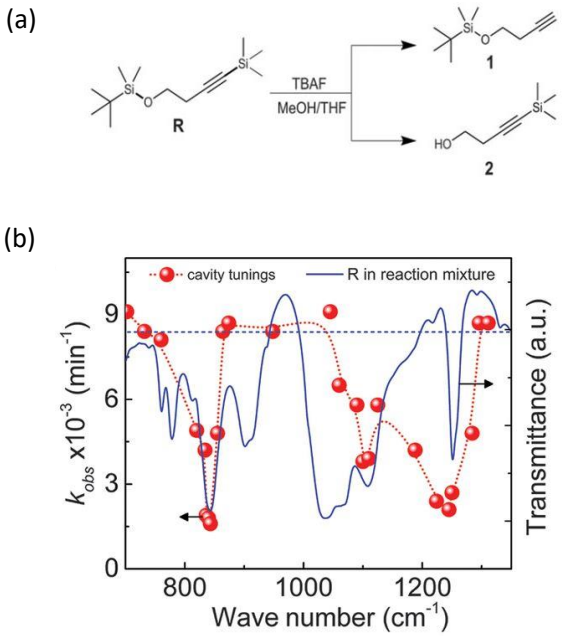

Figure 1. 16. (a) Major silyl cleavage pathways shown are Si-C to form 1, Si-O to form 2 for the reaction of R with TBAF; (b) Cavity tuning as a function of reaction rate inside the cavity (red spheres), blue dashed line represents the average rate outside the cavity. (Thomas et al. 2019)

In another significant step, the ratio of the two competing reaction rates and the branching ratio of the product formation was tested under VSC conditions.[74] To explore this, a silane derivative (R) was used with two different sites for silyl bond cleavage. Nucleophile attack on the Si atom results in two products: the cleavage of the Si-C bond, and the Si-O bond. IR spectrum of the R shows strong absorption bands corresponding to Si-C ($842\ cm^{-1}$), Si-O ($1110\ cm^{-1}$) stretching modes and bending mode of the CH_3 group bonded to Si ($1250\ cm^{-1}$). VSC of the Si-C stretching band retarded the reaction rate by a factor of 3.5 compared to the outside/OFF resonance cavity (Figure 1.16). Similarly, the coupling of Si-O retarded the rate by a factor of 2.5 times relative to the outside/OFF resonance cavity. The plot of reaction rate versus cavity tuning confirms that vibrational modes influenced the reaction rate. It also studied that the reaction rate can be precisely controlled by the TS under VSC representations in figure 1.17.

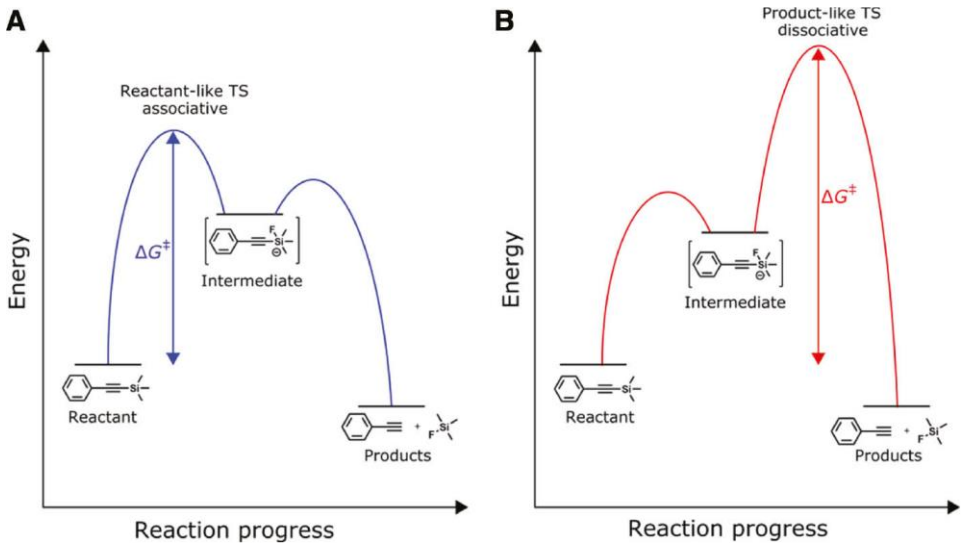

Figure 1. 17. Schematic illustration of possible transition states under (A) non-cavity and (B) VSC. (Thomas et al. 2020)

The chemical landscape is lifted towards the desired product, and VSC can be useful for elucidating reaction mechanisms.

1. 5 Applications of VSC beyond chemical reactivity

VSC can offer band-selectivity and recently utilized for electrochemical energy conversion without light pumping. Ionic conductivity is enhanced by order of magnitude by coupling the O-H_{str} band of water of an aqueous electrolyte $HClO_4$.[75] The cavity vacuum field might become a tool for material synthesis and molecular self-assembly. An observation of pseudo polymorphism in the crystallization from water and zeolite imidazolate frameworks (ZIFs) was

also studied inside the cavities after coupling of the O-H_{str} band of water resulting that: ZIF-8 crystals were selectively formed while the mixture of ZIF-L and ZIF-8 formed otherwise.[76] These metal-organic frameworks are of interest for gas absorption, chemical sensing, and catalysis applications. VSC has become a valuable tool for chemistry and material science where no external light source induced and selected bond is involved in the mechanism. The spontaneous Raman scattering was studied recently, and it was found that the coherent nature of vibro-polaritonic states boosts the scattering cross-section by two to three orders of magnitude.[60] So far, the spectral properties like the selection rule and lifetime of the vibro-polaritonic states are poorly understood. Infrared and filtered pump-probe spectroscopy reports the exciting vibration polariton's spectroscopic features and relaxation dynamics. Jeffrey C. Owrutsky and co-workers showed the strong coupling of the NO band of sodium nitroprusside to a mode of FP-cavity.[77] They found that the vibro-polaritonic excited state lifetime is longer than the coherent time revealed by Rabi-oscillation decay, indicating the support of an incoherent population. The cavity effect is also applied in the solid-state material properties such as; charge transport, magnetism, and superconductivity.[78,79] There has been extensive work to generalize the presence of strong radiation field molecule coupling in quantum chemistry. Theoretical studies under VSC are still not conclusive as there are many approaches starting from non-equilibrium nature to resonance interactions. Angel Rubio and co-workers recently developed the ab initio method, confirming that the QEDFT method is suitable for accessing such a local polaritonic effect. Collective strong coupling paves a way to control the local states and hence the fate of bond making or bond-breaking process.

Chapter 2

Ester Solvolysis under Cooperative Vibrational Strong Coupling: The Concept of Cavity Catalysis

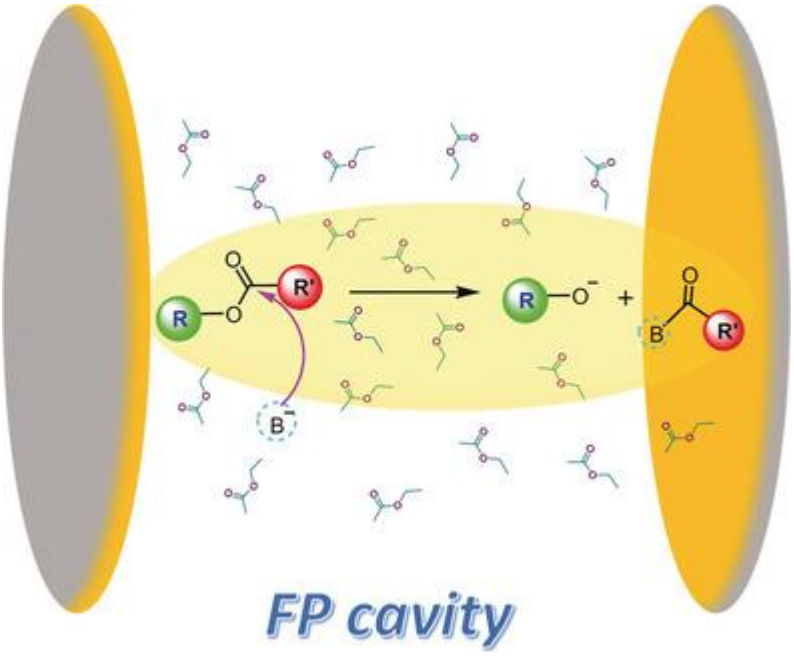

2. 1 Cooperative VSC

In a two-level quantum emitter system, there will be negligible populations that can modify the total energy of the system. In another way, the strong coupling of a single emitter is an arduous task at room temperature. To achieve strong coupling at a single molecule level, the molecular oscillator has to be very strong, and the mode volume of the cavity has to be extremely small [Eqn. 1.5 in Chapter 1]. Further, it is exciting to explore the model of the VSC in molecular ensembles and later to large numbers collectively coupled to the cavity mode.[47,80,81,132] Recently, A. Nitzan and co-workers simulated the cavity molecular dynamics forming collective VSC.[82] Asymmetric stretch of CO_2 molecules coupled to the cavity mode accelerates the hot molecule relaxation processes. This might be due to the transient excitation of the polaritons, which facilitates intermolecular vibrational energy transfer under VSC conditions. This idea can be further extended to understand the cooperativity and the collective behavior of the coupled molecules. Joel and co-workers demonstrate the consequence of Bose-Einstein condensation of polaritons on chemical reactivity.[83] The model includes quasi-degenerate dark modes that do not possess any photonic character and are likely to behave similarly to uncoupled molecules. All dark modes degenerate at a frequency ω_V and shows the massive degeneracy of dark modes, which enhance polaritonic effects by having a macroscopic occupation of the lower polariton mode, i.e., Bose-Einstein condensation. They showed that the vibrational polariton condensate changes in the reaction yield significantly compared with the excitation with infrared laser sources. It is due to the additional channels with reduced activation barriers resulting from the significant accumulation of energy in the lower polaritons and many modes available for the energy distribution during the reaction. In particular, they explained one could counteract the massive degeneracy of dark modes and enhance polaritonic effects by having a macroscopic occupation of lower polariton mode. The condensate can change the reaction yield significantly at room temperature due to the availability of additional reactive channels that differ in energy by $\hbar\Omega_{VR}/2$ rather than $\sim\hbar\omega_V$.

Most experiments of molecular strong coupling are carried out in the collective regime. The same concept was applied to the electron-phonon coupling, in which yttrium barium copper oxide (YBCO) powder was dispersed in the various polymer.[78] Strong polystyrene peaks overlap with the phonon mode of YBCO and explore the superconductivity. The mechanism believed is that strong vibrational bands of polystyrene resonant with the phonon mode that acts as a mediator, leading to VSC. This observation suggests that cooperative VSC modifies the molecular properties without external stimuli.

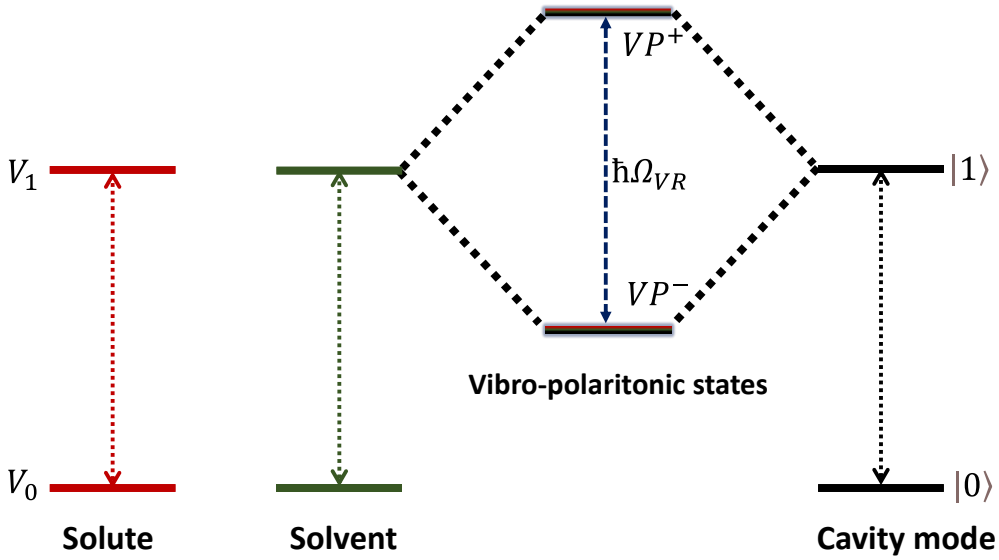

Figure 2. 1. Cooperative vibration strong coupling of solute-solvent molecules with the cavity mode forms vibro-polaritonic states separated by vacuum Rabi splitting energy represented $\hbar\Omega_{VR}$.

As mentioned above, cooperative coupling of a large number of molecular oscillators with an infrared photon result in large Rabi splitting energy that can modify the chemical energy landscapes. Cooperative VSC can be achieved in the liquid phase using specially designed Fabry-Perot microcavities. Recent experiments suggest that VSC can modify the chemical reaction rate and crystallization process at room temperature.[84,85] A solute with matching vibrational energy as solvent vibrations undergoes intermolecular energy transfer due to vibrational overlap in the system, leading to chemical and physical modification (Figure 2.1). For example, coupling a vibrational transition to an infrared cavity mode influences the ground state chemical reactivity. The introduction of cooperative VSC has opened the door to further advances in the field because chemical reactions are studied with low concentrations and in homogeneous media. Few examples are available in literature using cooperative VSC that can modify a ground-state chemical reaction without any external optical pumping. There are classes of organic reactions being explored. However, the current theoretical understanding cannot explain this experimental finding ably.

2. 2 Fabry-Perot Resonator

The development of micro/nanofabrication technology and its applications came decades ago. Micro- resonator with a high Q-factor with low internal loss is highly desirable and used for many applications. Choosing a microcavity for a particular experiment depends on several

factors such as ease of fabrication, less optical losses, minimum mode volume and tunability. The practical application of VSC requires a microchannel within a few micrometers ($2-25\ \mu m$) to study a chemical reaction. Ebbesen and co-workers have already demonstrated that such cavities can be fabricated easily using Au mirrors on IR transparent windows for liquid phase VSC (Figure 2.2 a).[58] Spectroscopic studies will help us to understand further how the coupling strength is affected when a vibrational transition of a molecule is coupled with the cavity mode.

The FP-cavity consists of two parallel gold (Au) mirrors coated onto BaF_2/CaF_2 windows separated by a mylar spacer shown in figure 2.2 b. The mirrors are aligned parallel to each other so that an electromagnetic field bounces back and forth and forms standing waves. The physical distance between the mirrors can be controlled by the top four screws in the demountable cell (Figure 2.2 a). Fine-tuning can be done by losing or tightening the screws to achieve the overlapping of a cavity mode with the vibrational stretching band of a molecule. The cavity can be tuned to resonance using a flexible polymer spacer between the mirrors—this close configuration forms a microfluidic cell that holds the liquid. Molecules with low vapor pressure are ideal for FP-cavity experimental studies.

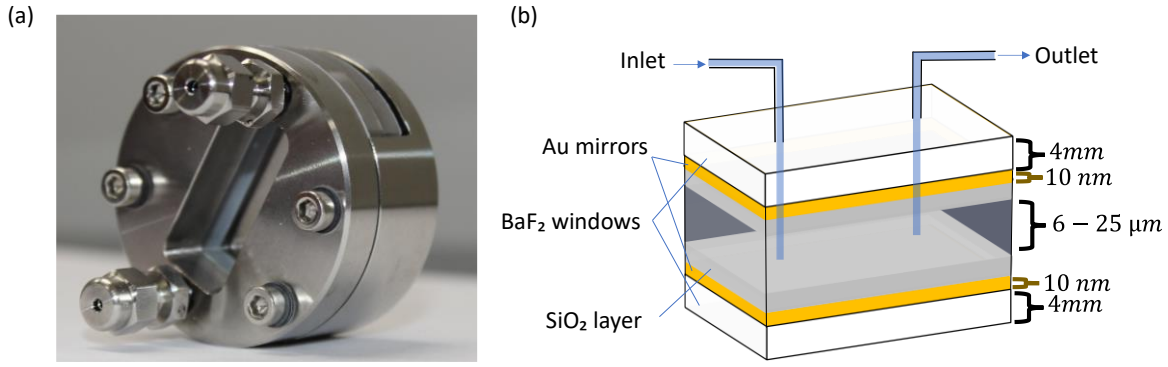

Figure 2. 2. (a) Image and (b) sketch of a microcavity QED reactor.

When the light comes in phase after a round trip accumulation, it forms cavity mode; this process will continue until the light leaks out of the cavity. The multiple reflections of light between the two reflective surfaces increase the electromagnetic field density. Consider an incident beam traveling through an FP cavity confined between two parallel mirrors; Figure 2.3 shows the path of light traveled through the cavity – the primary beam is partially reflected and transmitted at the first mirror. The transmitted light is subsequently reflected and again transmitted between the mirrors. Constructive interference occurs if the transmitted beams are in phase, this corresponds to a maximum transmission peak. At the same time, the transmitted

beams form destructive interference out of phase, resulting in a minimum in the transmission peak. It depends upon the angle of light travel, thickness, and refractive index of the medium. Here, r denotes the coefficient of reflection of mirrors and t is the transmission coefficient.

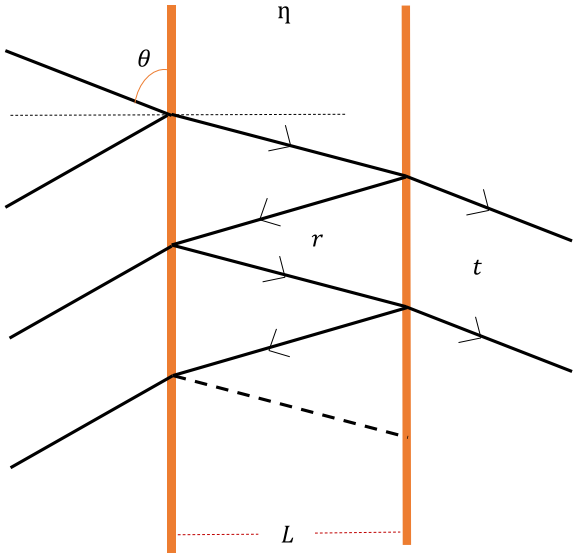

Figure 2. 3. Schematic representation of the paths of light travel in the Fabry-Perot resonator.

The phase difference δ between two successive transmissions is given by

$$\delta = \frac{2\,\pi}{\lambda}\, 2nL\, \cos\theta \qquad [2.1]$$

where n is the refractive index of the medium in the cavity, L is the cavity length, and θ is the incident angle of the light.

R denotes the reflectance and T transmittance of the mirrors and is given by,

$$T = \frac{(1-R)^2}{1-2R\cos\delta + R^2} = \frac{1}{1+F\,\sin^2\frac{\delta}{2}} \qquad [2.2]$$

Factor F is known as the coefficient of the finesse of the cavity.

$$F = \frac{4R}{(1-R)^2} \qquad [2.3]$$

Finesse factor depends upon the value of R. If the reflectance R is minimal, the value of F is also small, and the transmission peaks are broad and indistinct. If R is close to unity, sharp transmission and high Q-factors can be achieved.

The criteria to reach VSC is to achieve higher coupling strength compared to FWHM of the

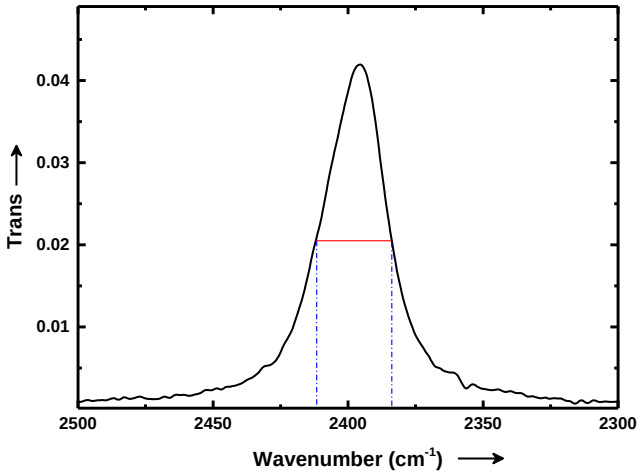

Figure 2. 4. FWHM of the cavity mode.

cavity mode and absorption band of the molecule. The energy dissipation from the cavity can be due to the absorption, scattering, or leakage through the imperfect mirrors. The quality factor (Q) can be defined as the ratio of energy stored inside the cavity and the energy dissipated per cycle. It was observed that the dissipation rate in the FP-cavity is lower as the thickness of the cavity increases.

$$Q = \frac{\omega_r}{\Delta\omega_c} \qquad [2.4]$$

ω_r is the resonant frequency and $\Delta\omega_c$ is the linewidth of the cavity mode (FWHM).

Generally, a high Q-factor cavity is achieved by the mirrors' high reflectivity so that photon is stored in the microcavity for a longer time. Fabry-Perot cavities based on metallic mirrors can be easily fabricated, with high reflectivity in the IR region ($R_{Au} = 98 - 99\ \%$) and a reasonable Q-factor (~ 100) shown in figure 2.4. Mode volume in FP-cavity is much higher than the distributed Bragg reflector (DBR) and plasmonic cavities. Therefore, high mode volume allows a large number of molecules in the cavity, and large collective Rabi splitting energy can be achieved. The resulting cavity modes are equally spaced in frequency, and the separation between the successive cavity modes is termed the free spectral range (FSR) of the cavity can be calculated in figure 2.5. The ON-resonance condition depends upon the cavity pathlength (μm) and refractive index (n) of the medium.

$$FSR\ (cm^{-1}) = \frac{10^4}{2nL} \qquad [2.5]$$

The collective strong coupling of the vibrational band with the cavity mode depends upon the concentration of the molecules. Under the resonant conditions, two distinct peaks in the

transmission spectra suggest forming vibro-polaritonic states. The polaritonic states inherit both the properties of the molecular state and the infrared photon. The upper and lower polaritons FWHM is the average of both the molecular band and the cavity mode and going up in the cavity mode numbers increases the lifetime of the polaritons and hence lowers the dissipation in the system. Please note that strong coupling process disappears if the photon decoherence occurs while coupling to large pathlength cavity modes. Whereas a low dissipation rate enhances the coherence time of hybrid states, and hence it can be long-lived. In another way, the total dissipation rate of the cavity and molecule should be slower than the

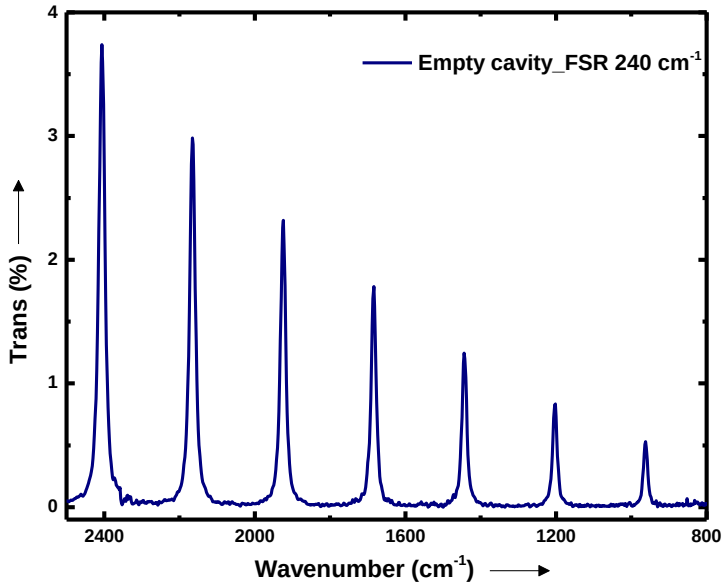

Figure 2. 5. FTIR spectrum of an empty cavity with a free spectral range of 240 cm^{-1}.

Rabi exchange process to achieve the so-called strong coupling condition. The molecule decay rate depends upon the transition dipole moment that is viewed as oscillating in phase under strong coupling. The cavity absorbs the energy emitted from the first molecule, and again it is used to excite the second molecule; this process is repeated multiple times until the system undergoes decoherence. It creates a strong interaction between the IR photon and many molecules coupled to the photon. Consequently, new vibro-polaritonic states are formed that can control the potential energy landscape of a chemical reaction.

2. 3 *a*. Ester solvolysis in Fabry-Perot cavities

A Cary 5000 UV-VIS spectrophotometer was used to measure the ester solvolysis of *para*-nitrophenyl acetate (PNPA) using a demountable flow cell set-up. PNPA was purchased from

Sigma Aldrich and had a molecular weight of 181.15 kg/mol^{-1}; melting point of $75-77$℃. 0.1 M of PNPA undergoes a base-catalyzed reaction with tetra-butyl ammonium fluoride (TBAF). The decomposition products of PNPA are *para*-nitrophenoxide ion (PNP^-) and *para*-nitrophenol had a UV absorption consisting of two bands shown in figure 2.6.[86] One was enhanced in alkaline solution, and the other in acidic solution. In an alkaline solution, there is maximum absorption at 400 nm, and the absorption diminishes as the solution becomes acidic.[87]

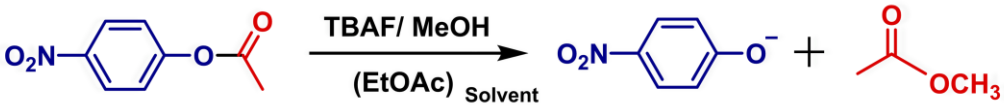

Scheme 2. 1. Base catalyzed solvolysis of PNPA in the ethyl acetate (EtOAc).

There is also an isosbestic point at 350 nm and the estimated pKa of *para*-nitrophenol is 7.15. We focus on studying the experiments at an alkaline pH (8.5) and assume that the reaction follows a pseudo-first-order process.

A demountable flow cell with BaF_2 windows was purchased from Specac Ltd. UK and used for the studies. BaF_2 ($4mm\ window\ thickness$) was coated with 10 nm Au film by sputtering techniques and Mylar spacer of 18 μm was used for the non-cavity and cavity experiments.

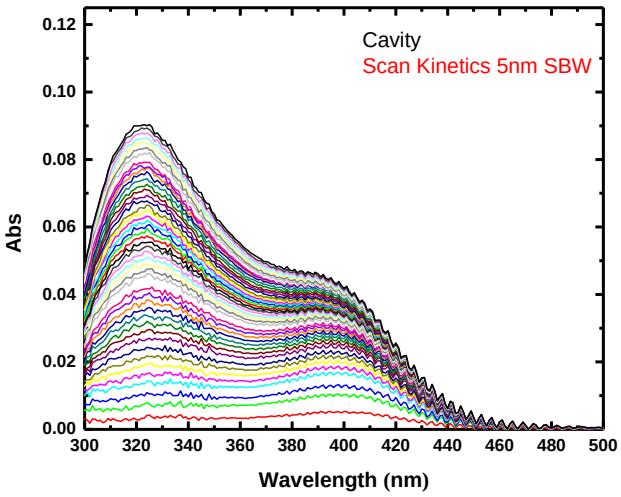

Figure 2. 6. Absorption spectra showing the evolution of PNP- at 400 nm during the progress of the ester solvolysis.

Ester solvolysis of PNPA in the mild alkaline condition of TBAF was done by mixing 0.1 M PNPA ($18mg\ in\ 1ml\ of\ EtoAc$) and 0.1 M TBAF ($31.5\ mg\ in\ 1ml\ of\ methanol$). A fresh

solution of PNPA (reactant) was prepared each time, whereas TBAF (reagent) was prepared and stocked. The reactant 270 μl and reagent 30 μl were mixed in the ratio of 9: 1 in a glass vial. The reaction mixture was injected immediately into the demountable cell with the disposable syringe (Inlet and outlet shown in figure 2.2 a, b). It is essential to remove the air bubble during the injection. The final concentration of the PNPA and TBAF was 0.1 M and 0.01 M, respectively. Reaction rate followed with the absorption peak at 400 nm, and kinetic data was plotted for an initial 100 $seconds$. Free spectral range (FSR) was measured in the same UV-VIS spectrophotometer in which reaction kinetics were studied. FSR was calculated in every case by taking the average cavity modes of an empty cavity and by back-calculation to assure that it reached the resonance condition before the injection of the reaction mixture. We were using Eqn. 2.5, the refractive index of the solvent (EtOAc) and pathlength 18 μm, FSR were estimated before and cross-checked after the completion of the reaction. Refractive index variation of the medium is minimal as the concentration of the solvent is 100 $times$ larger than the reactant. After setting the empty cavity FSR, the flow cell was kept for stabilization ~30 $minutes$.

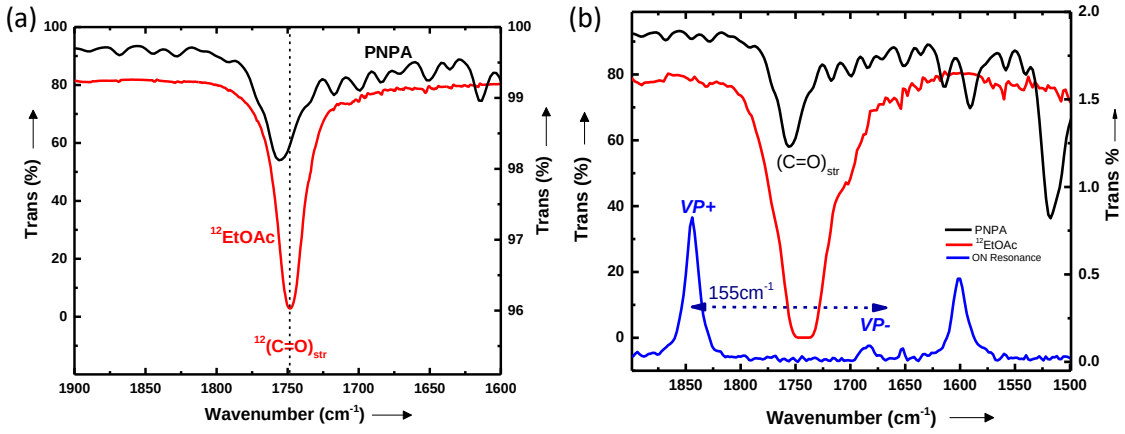

Figure 2. 7. Carbonyl band of PNPA (ATR spectra; black trace) and FTIR spectra of ^{12}EtOAc (red trace); (a) 10% diluted ^{12}EtOAc with hexane; overlapping of carbonyl stretching mode of ^{12}EtOAc and PNPA; (b) pure ^{12}EtOAc coupled with $10th$ mode of the cavity; formed $VP+$ and $VP-$ (blue trace) vibro-polaritonic states.

Base catalyzed ester solvolysis follows a $B_{Ac}2$ mechanism in which methoxy ion ($^{-}OCH_3$) attacks the electron-deficient carbonyl C-atom and forms a tetrahedral intermediate; it is the rate-determining step for the reaction.[88,89] Secondly, acyl bond-breaking follows the TS, leading to product formation (Scheme 1.1). PNP- is a better leaving group that shows a yellow coloration to the medium. The rate of PNPA solvolysis is dependent on the stability of the TS,

which is controlled by the surrounding solvent molecules. To achieve strong coupling, it is not possible to directly couple the PNPA vibrational bands because of less number of oscillators/ low concentration. We have chosen a solvent with a matching frequency of carbonyl stretching of the solute molecule (Figure 2.7 a); these vibrations ($C{=}O_{str}$) are involved in the rate-determining step of the reaction. Rabi splitting energy of 155 cm^{-1} is achieved by cooperative coupling of both the solute (PNPA; 0.1 $wt\%$) and solvent (EtOAc) molecules, as shown in figure 2.7 b. The formation of vibro-polaritonic states changes actual transition energy into upper and lower polaritonic states with $VP+$ and $VP-$ at 1840 cm^{-1} and 1685 cm^{-1}, respectively. Rabi splitting and the polaritonic states can be easily seen by using a Bruker FT-IR spectrophotometer.

We compared the reaction rate in the non-cavity and cavity by maintaining all the physical conditions of the system similar, except the cavity will have two parallel mirrors. Initially, the progress of the reaction can be easily monitored by the temporal evolution of the PNP- using a UV-VIS spectrometer by coupling the $C{=}O_{str}$ band at the end of the reaction. FSR after the reaction gives the information, whether it was under strong coupling conditions or not. Please note that FP-cavity

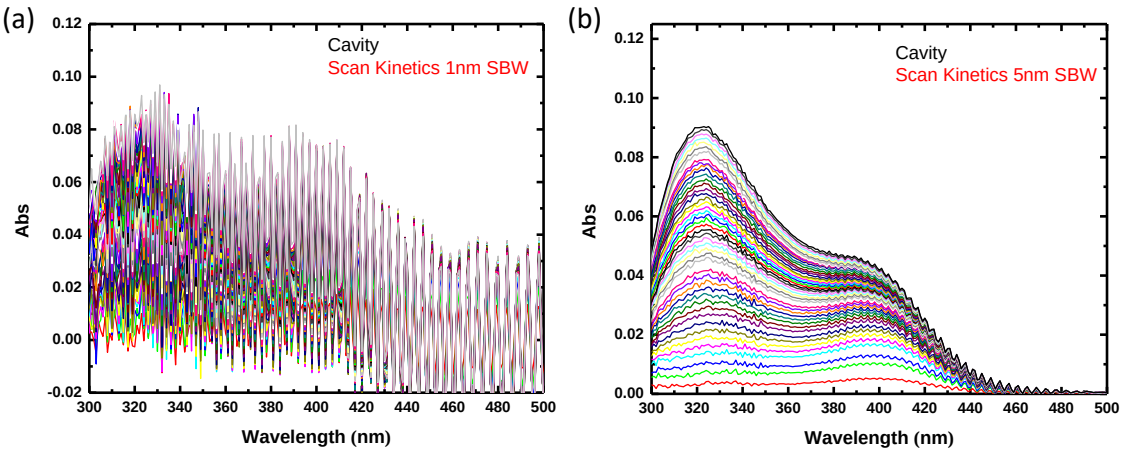

Figure 2. 8. Temporal evolution of PNP- in the FP-cavity with spacer 18 μm using scan kinetic mode of the spectrometer for SBW of; (a) 1 nm and (b) 5 nm.

configuration has feeble interference in the UV-VIS region that misguided us in the beginning and that was proposed in the original article. The interference pattern usually rides over the original absorption as the reaction proceeds (figure 2.8 a). This again gets amplified at ON-resonance conditions due to local environmental changes such as refractive index (RI) variation etc. Later, this was corrected by keeping the slit bandwidth (SBW) high in the instrument (5 nm) so that the absorption line shape is intact (Figure 2.8 b), especially when we collect

single-point kinetic experiments. Please also note that the data collected in the UV-VIS spectrometer is a differential absorption spectrum with an overall absorption reaching only up to 0.05 OD. One needs to be very careful in analyzing the data and the background spectra of the spectrometer shouldn't change during the cause of the measurement. The concentration of the PNPA is also optimized to achieve a reasonable rate for kinetic probing and hence cannot be increased further.

The same experiment was repeated by Wiesehan et al.; they attempted to reproduce our original experiment of *cavity catalysis*.[129] In the report, they achieved the same splitting energy, but the detuning dependence of kinetics rates is not observed. They have done all their experiment in flow-cell conditions. The design of the cell setup consists of four gas syringes. Two syringes contain the desired quantities of each reactant solution and the third syringe contains air and acts as a driving piston that drives the fluid. The fourth syringe contains EtOAc to flush out the residues. The experiments are challenging for the following reasons: 1) molecules spend less time in the cavity, and the VSC effect is minimal. 2) Even if the measurement pauses to static mode, some residue pressure will generate a flow condition, especially if the pathlength is $18\mu m$ due to the internal pressure of the cavity configuration. We believe that the experimental setup and kinetics measurements conditions are different from our experiment. It can be due to solution preparations, reactant mixing ratio, and washing and drying the windows. After each measurement, cleaning the spacer, windows, vials and tubing is very important. Our experimental setup is different; we used static conditions for the measurement discussed in the follow-up manuscript.[134] We opened the geometry and carefully washed the windows, demountable cell inlet-outlet and dried. It is crucial to note that the spacer should be clean and has no residue from the previous measurement. The report shows the parallelism of the mirrors in figure 5 (ref. 133) and the interference pattern. In our case, a sweet spot (Newton Ring) is the center of the cavity that offers parallel mirrors. It can be achieved by equally tightening or losing the screws. A uniform Newton ring confirms that the mirrors are perfectly parallel, which is the first criterion for achieving strong coupling. As the UCSD team suggests, the experimental procedure for the reproducibility test is not similar to the original work. Another major concern is the kinetic rate calculated by averaging the absorbance area between $395 - 405\ nm$ for each time step. Averaging the raw data is risky as the interference will be amplified that read to serious errors in cavity data. Each measurement in the cavity is independent and cannot be comparable or averaged out. Wiesehan et al. have done the detuning experiment within the range of $\mp 80\ cm^{-1}$ and found an error bar high as the move from the ON-resonance

condition. There may be a chance of leaking the solution from the cavity as it is loose/ or in a more tight situation. The interference pattern in the cavity misled the original change in the absorbance of PNP- ions and the area under the curve for the rate calculation will give unclear results. The judgment to reach ON-resonance conditions (X-axis of the tuning curve) by Wiesehan et al. is looking into the upper and lower polaritons positions. That is different in all our experiments; we have assumed this parameter by using FSR calculation between 7000-5000 cm^{-1}; a procedure to estimate the actual FSR is discussed in the previous section.

2.3 *b*. Corrections to the original paper

Our earlier experiments were done using SBW-1 nm by default for single-point kinetic measurements and experiment turned out to be amplified due to the interference mode of the cavity at 407 nm. This error occurred due to the system default setting and the temporal scan is always done at SBW of 5 nm. This original result is published in *Angew. Chem. Int. Ed. 2019, 58, 10635-10638* and has been corrected in the follow-up publications. In the original report, final FSR was calculated using an FTIR spectrophotometer in the range of $6000 - 4000\ cm^{-1}$ after probing the reaction kinetics. Each FSR data is calculated by averaging of five higher order uncoupled modes ($6000 - 4000\ cm^{-1}$) and plotted versus the apparent rate as shown in the figure 2.9. We further conducted all the experiments in an SBW-5 nm and the interference pattern is completely smoothened, as shown in figure 2.8 *b*. Originally reported figure shows an enhancement of more than one order of magnitude, as shown in figure 2.9.

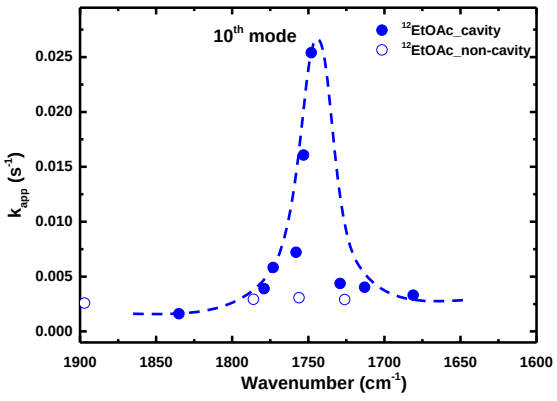

Figure 2.9. Single point kinetic rate measured (k_{app}) at 407 nm with SBW of 1 nm by tuning the cavity mode (^{12}EtOAc; blue filled circles) and non-cavity (^{12}EtOAc; blue empty circles). The dashed curve is a guide to the eye.

PNP- absorption is also sensitive as the absorption envelope still suffers from signal-to-noise issues due to poor absorption of 18 μm pathlength cell. Please note that the tuning experiments are very challenging as each cavity data give slightly different conditions even if one does a measurement within the same day using the same stock solution. Cavity Q-factor is another uncontrollable parameter, which may vary between 70 to 100 while tuning experiments. However, we attempted to see a general trend using the same stock solutions, pH conditions and the temperature of the medium.

2.4 Result and Discussion

At room temperature, the reaction follows the pseudo-first-order and the apparent rate of the non-cavity $k_{app} = 1.1 \times 10^{-3}\ s^{-1}$ (average of three measurements) plotted in figure 2.10 b. Cavity experiments are done at different tuning conditions, including the ON-resonance points and OFF-resonance data on either side of the C=O_{str} band region. ON-resonant cavity shows an enhancement of $k_{app} = 2.8 \times 10^{-3}\ s^{-1}$ which is roughly 2.5 $times$, increase compared to OFF-resonance and non-cavity apparent rates (Figure 2.10 b). In the present study of the reproducibility test, the FSR calculation was done by the same UV-spectrophotometer, which is different from the original paper. This method analyzes the FSR on the same area where reaction kinetic is probed. Cary-5000 UV spectrophotometer controls the level of precision across the whole scan. To achieve the strong coupling, we pre-calculate the estimated FSR using the eq [2.5] before the reaction mixture is injected into the demountable cell. The reaction mixture was injected into the cavity and run the kinetics for 5 minutes. Further, the FSR value is calculated in the range of $7000 - 6000\ cm^{-1}$; that avoids the background absorbance of O-H overtone stretching modes nearly $5500\ cm^{-1}$. That can result in a shift in the actual FSR of the system. Since the probing area of the beam in the UV-Vis spectrometer may be different from the actual FTIR probing area, this can in principle globally shift in the tuning plots.

Due to limited thickness availability, cavity tuning and kinetic action spectra have been done around the vibrational envelope of the C=O_{str} band. Please note that a Mylar spacer of 18 μm

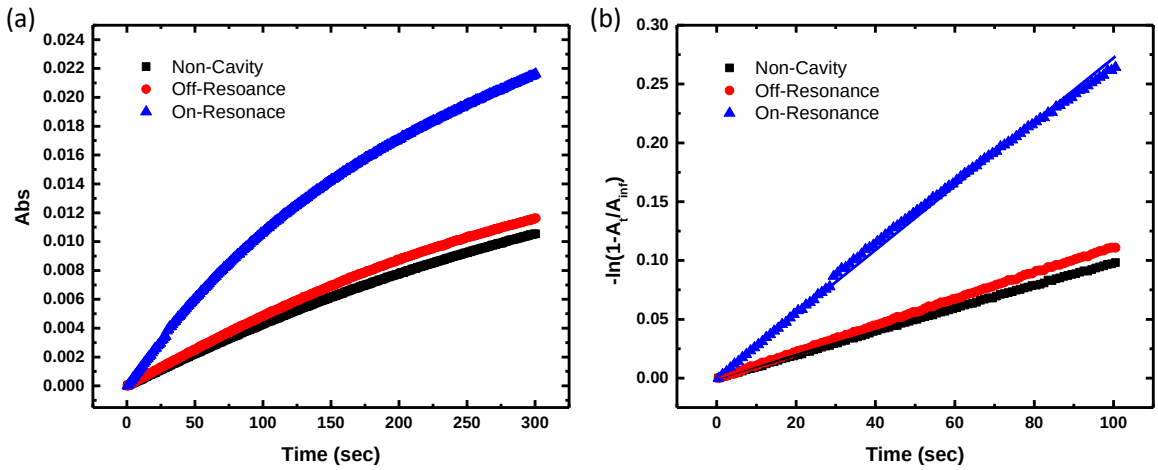

Figure 2.10. Reaction kinetics at 400 nm in non-cavity (black trace), OFF-resonance at 1780 cm^{-1} (red trace), ON-resonance at 1744 cm^{-1} (blue trace) corresponding; (a) Absorption traces; (b) Kinetic traces follow pseudo-first-order.

is elastic and we tightened or loosened the spacer very carefully using the front screws of the FP cavity set-up, that gives a FSR precision of 1 cm^{-1}; that can carefully tune the $10th$ mode position. Here, we tuned the cavity mode position of 1780 cm^{-1}, $k_{app} = 1.1 \times 10^{-3} s^{-1}$ shows the same rate as that of non-cavity. The reaction kinetics were performed for each experiment by slowly changing the FSR of the cavity. The apparent rate calculation by varying the cavity mode position is plotted in figure 2.11; table 2.1, and corresponding apparent rates versus cavity tuning is shown in figure 2.12.

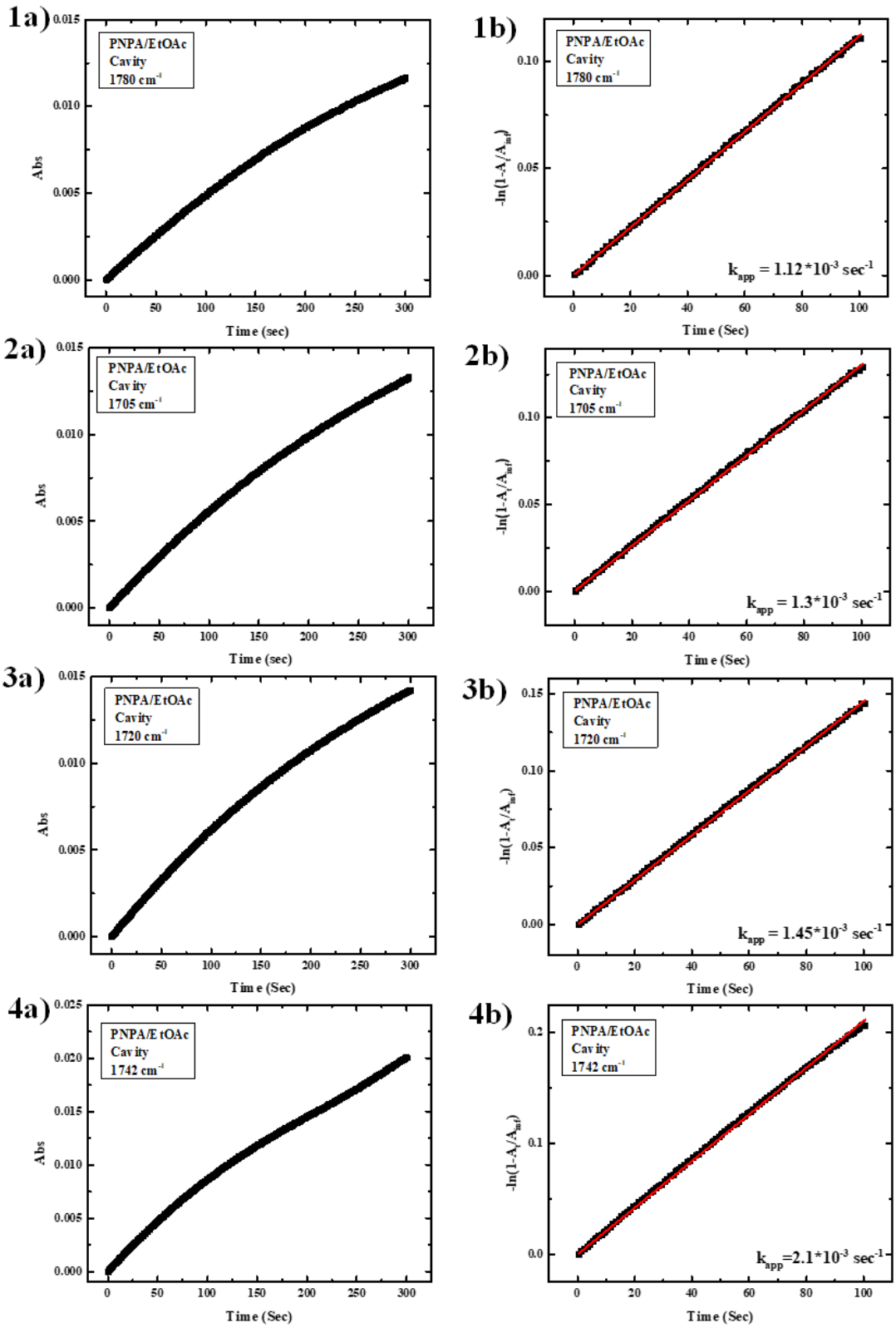
1a)
PNPA/EtOAc
Cavity
1780 cm-1
Abs
Time (sec)
1b)
PNPA/EtOAc
Cavity
1780 cm-1
-ln(1-At/Ainf)
kapp = 1.12*10-3 sec-1
Time (Sec)
2a)
PNPA/EtOAc
Cavity
1705 cm-1
Abs
Time (sec)
2b)
PNPA/EtOAc
Cavity
1705 cm-1
-ln(1-At/Ainf)
kapp = 1.3*10-3 sec-1
Time (Sec)
3a)
PNPA/EtOAc
Cavity
1720 cm-1
Abs
Time (Sec)
3b)
PNPA/EtOAc
Cavity
1720 cm-1
-ln(1-At/Ainf)
kapp = 1.45*10-3 sec-1
Time (Sec)
4a)
PNPA/EtOAc
Cavity
1742 cm-1
Abs
Time (Sec)
4b)
PNPA/EtOAc
Cavity
1742 cm-1
-ln(1-At/Ainf)
kapp=2.1*10-3 sec-1
Time (Sec)

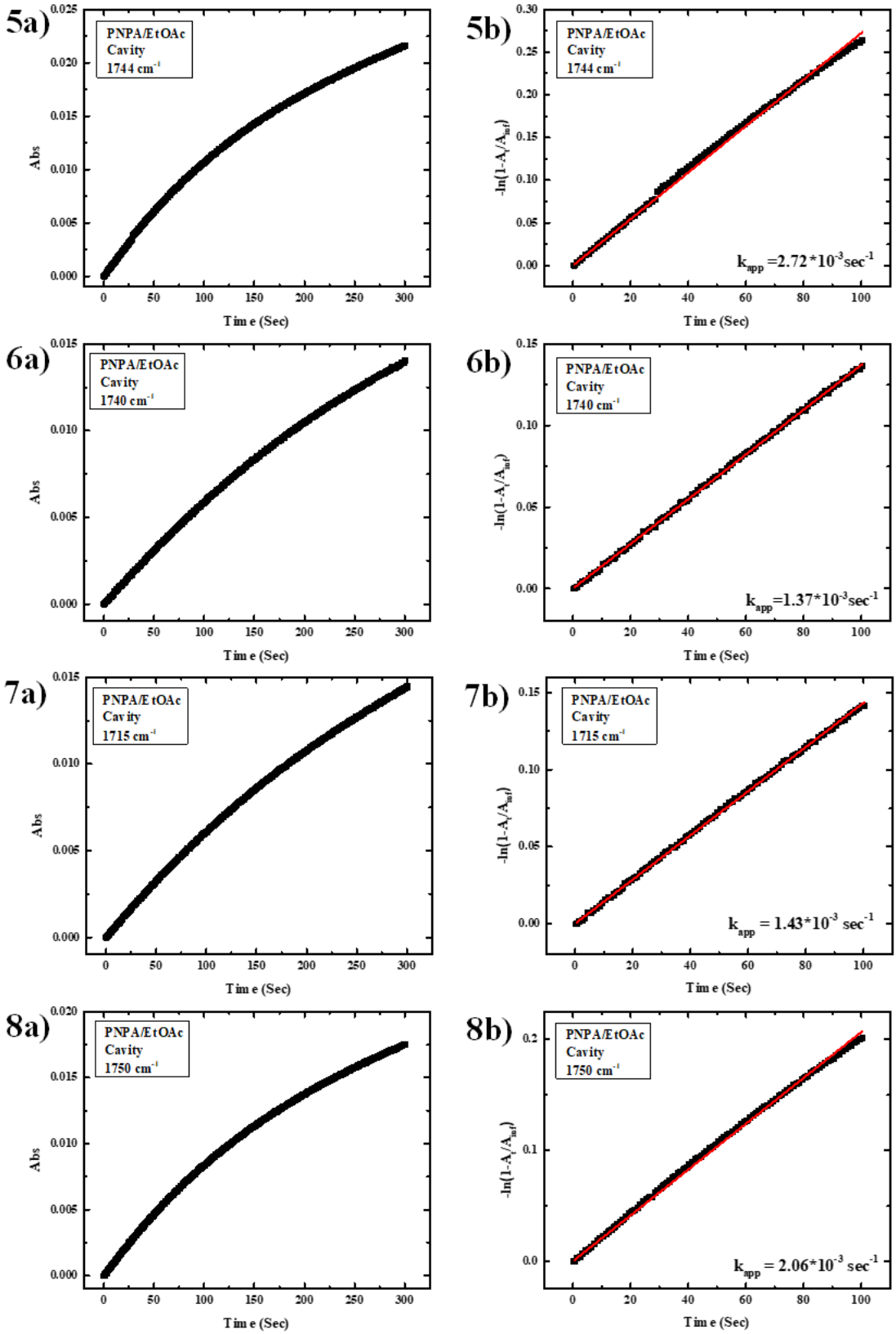

Figure 2.11. The experiment was performed by tuning the cavity mode position by changing the FSR value at 400 *nm* with SBW of 5 *nm*; (a) Abs vs. time; (b) Calculation of reaction rate; given in table 2.1.

Table 2.1. k_{app} of tuning experiment (all the experiments done with the same batch of the solution)

S.No.	$FSR(cm^{-1})$	$k_{app}(s^{-1})$
1	1780	1.12×10^{-3}
2	1705	1.3×10^{-3}
3	1720	1.45×10^{-3}
4	1742	2.1×10^{-3}
5	1744	2.72×10^{-3}
6	1740	1.37×10^{-3}
7	1715	1.43×10^{-3}
8	1750	2.06×10^{-3}
9	1701	1.91×10^{-3}
10	1757	1.58×10^{-3}
11	1769	1.56×10^{-3}

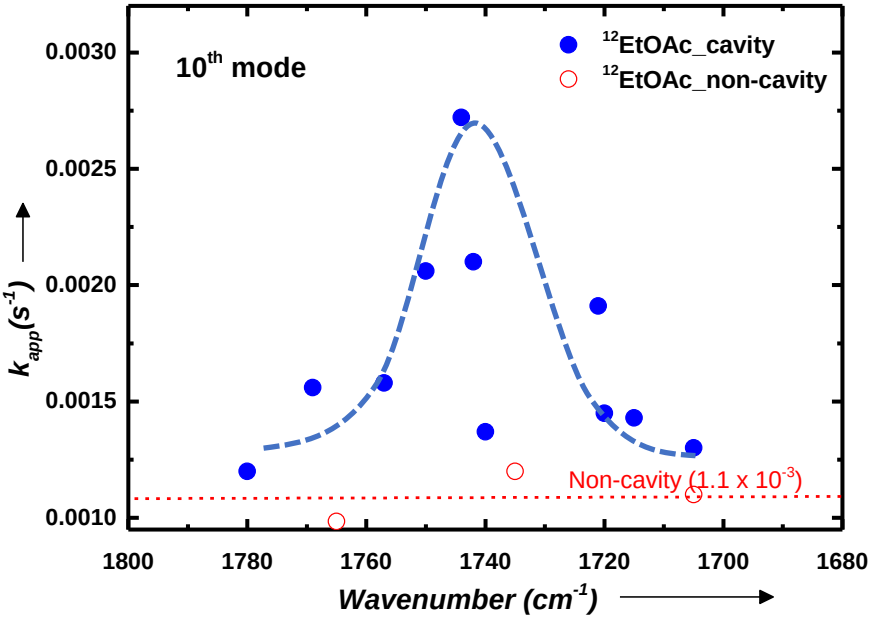

Figure 2.12. Kinetic action spectra of cavity tuning experiments around the C=O_{str} of PNPA molecules: cavity (filled blue circles) and non-cavity (empty red circles). Dotted line is a guide to eye.

Further, isotopic studies are conducted under the cooperative mechanism between the solvent and the reactant molecules. Here, the solvent, ethyl acetate; ^{12}C=O of ^{12}EtOAc is replaced with ^{13}C=O of ^{13}EtOAc isotope. FTIR measurements suggest a shift in the carbonyl frequency from 1750 to 1706 cm^{-1} (Figure 2.13 *a*). The signature of strong coupling was verified by

measuring the FTIR spectra suggesting a similar Rabi splitting energy ($150\ cm^{-1}$) from the carbonyl band of ^{13}EtOAc with $VP+$ and $VP-$ at $1792\ cm^{-1}$ and $1642\ cm^{-1}$ respectively (Figure 2.13 b). It is striking to note that for ^{13}C=O isotopic experiments, the non-cavity apparent rate ($kapp = 2.4 \times 10^{-4}\ s^{-1}$) is one order less than the ^{12}EtOAc system. This significant change indicates the secondary isotopic effect from the vibrational overlapping of solute PNPA with solvent molecules.[90] It facilitates a solvent-directed vibrational energy transfer in the system. Whereas, in the cavity experiments, due to minimal overlap between the reactant and the solvent molecules, the rate modification is negligible, as shown in figure 2.14. It confirms that the VSC of ^{12}EtOAc and PNPA is purely invoked through the cooperative mechanism.

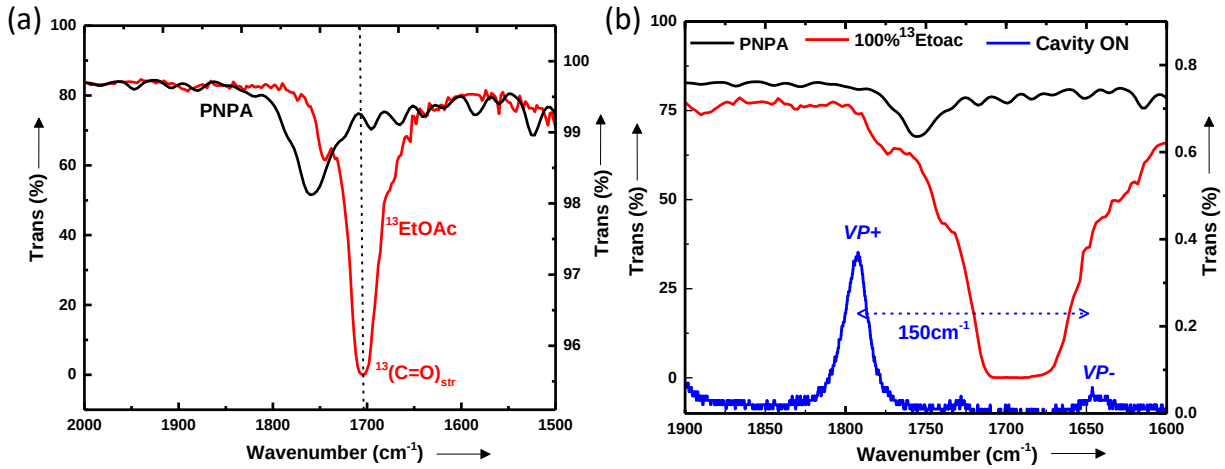

Figure 2. 13. Carbonyl band of PNPA (ATR spectra; black trace) and FTIR spectra of ^{13}EtOAc (red trace); (a) 10% diluted ^{13}EtOAc with hexane; (b) Pure ^{13}EtOAc coupled with $10th$ mode of the cavity; formed $VP+$ and $VP-$ (blue trace).

To continue this discussion, VSC can be transferred from solvent to the solute as long as vibrational bands overlap and IR photon cannot discriminate between the reactant and the solvent vibrational states as the process is occurring collectively. As the cavity mode position enters into the coupling of the C=O$_{str}$ band of the reactant and the solvent molecules, the reaction rate enhances along the vibrational band region and shows a maximum of around $1750\ cm^{-1}$ and decrease as you move away from the active band (Figure 2.14 b). There must be a more vital solute-solvent dipolar interaction that favors the presence of VSC condition and hence after the vibrational energy transfer (VET) between the solvent and the solute molecules. Strong coupling of the C=O$_{str}$ oscillators of the solvent influences the reactivity, where bond selectivity is crucial. The coupling of the carbonyl carbon atom is essential as the same bond determines the rate of the reaction. Lindoy et. al. developed an analytical rate theory for cavity-

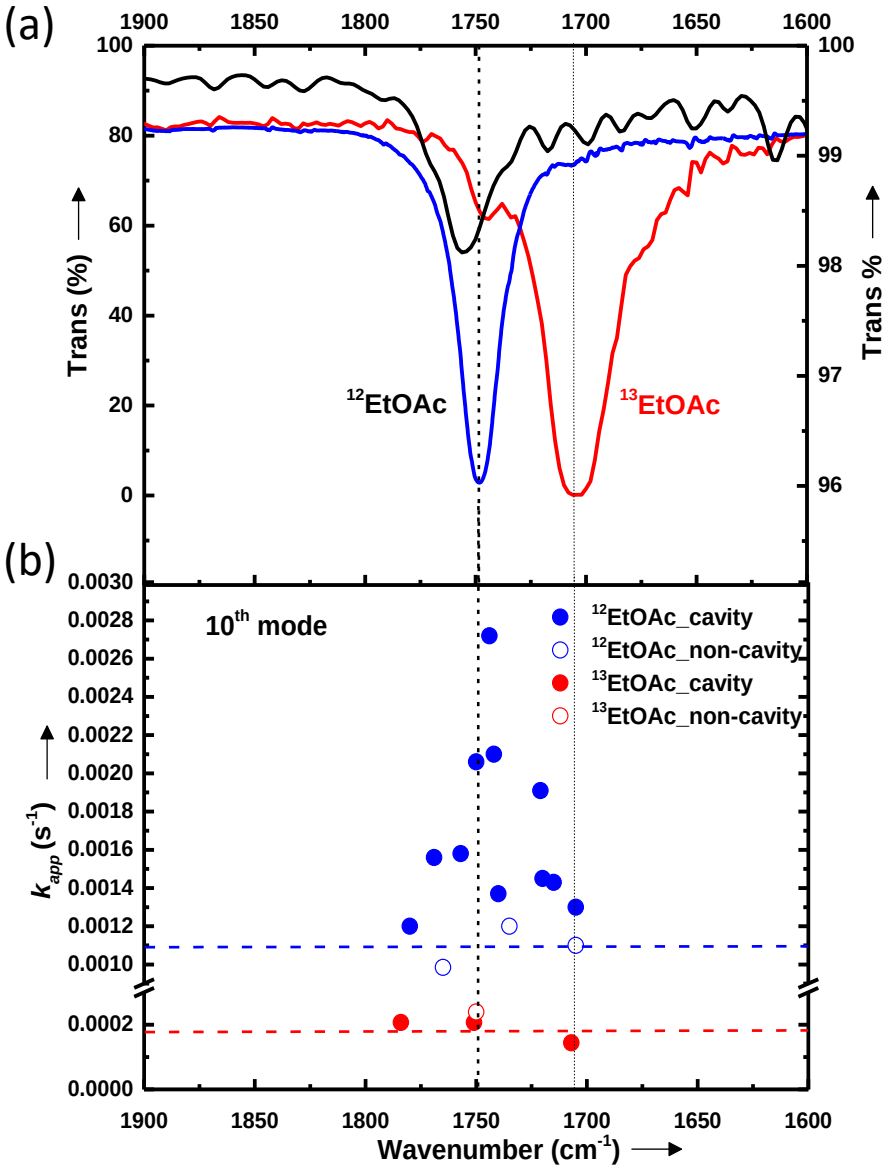

Figure 2. 14. Comparison of kinetics rate by changing the isotope of solvent from ^{12}EtOAc to ^{13}EtOAc. (a) Vibrational overlapping of C=O_{str} of ^{12}EtOAc with PNPA whereas ^{13}EtOAc shifts the band position; (b) Corresponding kinetic traces measured by tuning the cavity (^{12}EtOAc: blue filled circles; ^{13}EtOAc: red filled circles) and non-cavity (^{12}EtOAc: empty blue circles;^{13}EtOAc: empty red circles).

modified ground state chemical kinetics.[138] They showed that the chemical reaction rate can either be enhanced or suppressed depending on the bath friction; when bath friction is weak chemical kinetics is enhanced as opposed to the case of strong bath friction, where chemical kinetics is suppressed. Further, showed that the photon frequency at which maximum modification of chemical rate is achieved is close to the reactant well, and hence resonant rate modification occurs. The results reveal that the cavity modification of chemical rates can

largely be rationalized by considering how molecular vibrational states are altered by hybridization with cavity photon states (forming so-called vibrational polaritons) to effectively increase or decrease the interaction of the molecule with its environment. These effects emerge from fundamental quantum light-matter interactions and cannot be fully captured with simple classical or semiclassical descriptions of light and matter. Most theoretical work operate in the single molecule limit and do not address collective effects in a direct manner. The origin of this remarkable effect remains unknown.

Catalysis, as defined by IUPAC, is: "A process that increases the rate of a reaction without affecting the overall standard Gibbs free-energy change in a reaction." Here, the vacuum field energy accelerates a chemical reaction rate; it is the conserved energy created and annihilated within the system. Our idea was to test the process by looking into the thermodynamic variation of the cavity and non-cavity conditions. Temperature-dependent studies are conducted to extract activation parameters using the Eyring relation that connect the conventional kinetics rates to thermodynamic parameters. All the reactions were performed using a special temperature control jacket covering the microfluidic flow cell cavity and within the temperature range of $20 - 30$ ℃. There is a limitation to experimenting with a range of temperatures because we calculated the initial rate, which becomes very fast at higher temperatures and posed challenges to analyzing the rate of the reaction. The temperature in the flow cell has been equilibrated for $30\ minutes$. The activated parameter was calculated from the Eyring equation under the non-cavity and ON-resonance conditions of VSC.

$$k_{app} = \frac{k_B T}{h} exp\left(\frac{-\Delta H^{\neq}}{RT} + \frac{\Delta S^{\neq}}{R}\right) \qquad [2.6]$$

The enthalpy of activation ($\Delta H^{\neq}$) decreases from $82.53\ KJmol^{-1}\ to\ 70.36\ KJmol^{-1}$, under VSC of ^{12}EtOAc molecules. Another interesting finding is that the entropy of activation ($\Delta S^{\neq}$) decreases significantly from $-20.4\ JK^{-1}mol^{-1}\ to\ -58.86\ JK^{-1}mol^{-1}$; this large decrease of $\Delta S^{\neq}$ Indicates that TS is more polar under VSC conditions (Figure 2.15). However, the change on $\Delta\Delta G^{\neq}$ is in the 1-2 kJ/mol range, close to the solvation energy limit in any chemical reactions. Please note that the Y-axis of $figure$ 2.15 is updated (SBW-5 nm) and is different from the original paper (see footnote*). The overall activated energy is stabilized under the cooperative VSC of solute-solvent molecules. Interestingly, the enthalpy compensates for the entropy of activation, not affecting the reaction mechanism. Hence, 'cavity catalysis' is an apt

terminology here, whereas the VSC effect occurs only by selectively tweaking a vibrational state.

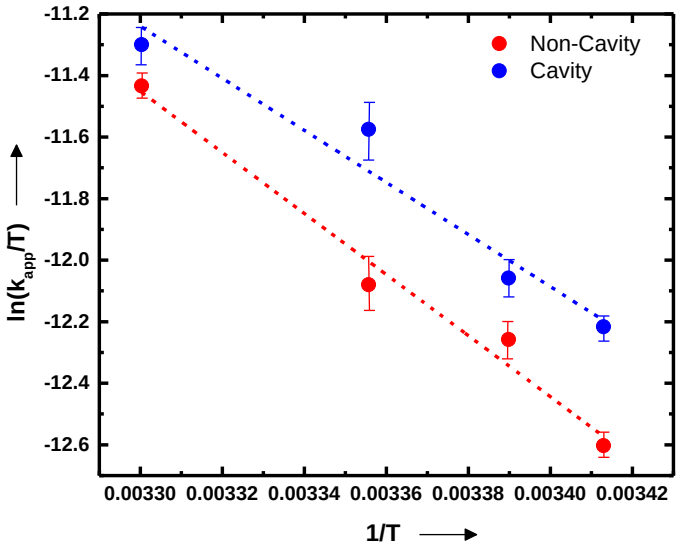

Figure 2. 15. Eyring plot for a reaction inside the cavity (blue circles) and non-cavity (red circles).

* Y-axis of $figure$ 3 of the ref (91) is erroneous as it only plotted the $\ln(k_{app})$ *versus* $1/T$.

Xinyang et. al. shows that at "resonance" frequency, the cavity radiation mode induces a dynamical-caging effect such that the molecular reaction coordinate becomes trapped in a narrow "photonic solvent cage" near the barrier region.[139] To account the "effective change" of the Gibbs free energy barrier $\Delta(\Delta G^{\neq})$ that is equivalent to the change of κ, where κ is the transmission coefficient that captures the dynamical recrossing effects, measuring the ratio between the reaction rate and the TST rate. By using Eyring rate equation $k = \frac{k_B T}{h} exp\left(\frac{-\Delta G^{\neq}}{k_B T}\right)$ and thus $\Delta G^{\neq} = -\frac{1}{\beta}\ln(2\pi\beta \cdot k), \beta = 1/k_B T$, with $k = \kappa \cdot k_{TST}$. Rewrite the above $\Delta G^{\neq} = -\frac{1}{\beta}\ln(2\pi\beta \cdot \kappa \cdot k_{TST})$. k_{TST} is a constant at any coupling strength and cavity frequency and is same for bare molecular case. The effective $\Delta(\Delta G^{\neq})$ solely depends on the change of κ. The change of free energy barrier compared to the bare molecular reaction is then $\Delta(\Delta G^{\neq}) = \Delta G^{\neq} - \Delta G_0^{\neq} = -\frac{1}{\beta}\ln\kappa/\kappa 0$. This work underscores the importance of "dynamical solvent effect" of the cavity radiation modes and may provide a new perspective for understanding the modification of reaction rate in polariton chemistry experiments.

2. 5 Conclusion

Ester solvolysis studies under VSC catalyzed the reaction, and the effect is very selective to coupling the $C{=}O_{str}$ of ^{12}EtOAc molecules in a cooperative way.[91] As evidenced from the isotope experiments, a clear vibrational overlapping between the solute and solvent molecule is the minimum criterion for achieving cooperative VSC. Our first prototypical experiments suggest that cavity catalysis requires the following criteria: 1) vibrational overlap of the solute and the solvent, 2) collective coupling behavior; which purely depends on the total number of coupled molecules, and 3) band and site-selectivity while tuning the cavity mode positions (IR photon energy). The above conditions indicate that VSC occurs internally, i.e., without any external stimuli. Finally, the thermodynamic data unequivocally shows that the reaction is catalyzed under VSC of the solvent. On the experimental side, many classes of chemical reactions need to be investigated to extract general principles that govern under VSC. As demonstrated here, the use of cooperative effects should greatly facilitate this task in that it removes the requirement of a high concentration of reactants to achieve the strong-coupling condition.

Chapter 3

Study of structure-reactivity relationship under cooperative VSC

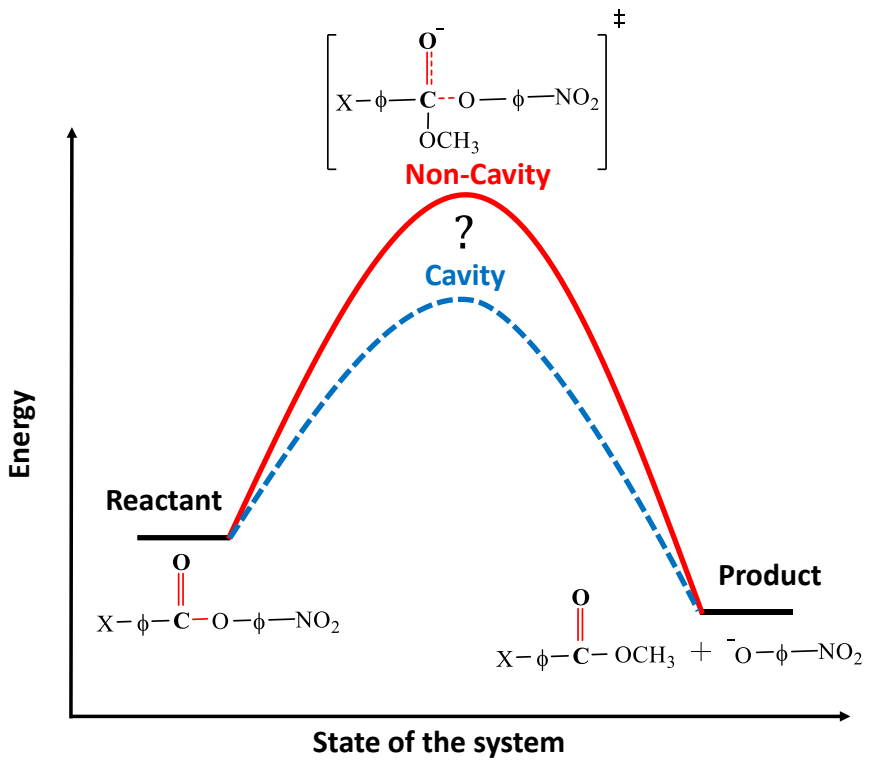

3.1 Introduction

Solute-solvent interactions are very complicated to access spectroscopically and are even more extensive under VSC conditions. To assess the effect of solvent on the reaction rate of a solute via VSC, precise planning for a correct choice of solvent is very important. More than 300 solvents are known, and the qualitative rule of "like dissolving like" and quantitative data, e.g., boiling point, dielectric constant, and refractive index, make it hard to choose the partner for this to synchronize dancing that results in breaking or making of a bond. One of the most common rules for selecting a solvent is "polarity." As discussed in the previous chapter, cooperative VSC requires vibrational overlapping of the solute and uses moderate polarity solvents to probe the chemical kinetics. Electrostatic solvation models are available in the literature discussing the effect of dielectric constant and permanent dipole moment; these are unique parameters that define solvent polarity.[92] The dielectric constant describes the ability of a solvent to separate electrical charges and orient its dipolar molecules. At the same time, solute-solvent interaction is more extensive and complicated: in addition to the nonspecific coulombic, inductive, dispersive interaction, specific hydrogen bonding, electron-pair donor/acceptor, and solvophobic interactions, etc. plays a role in controlling the reaction environment. It is the sum of all molecular properties responsible for the solute and solvent interactions. Organic chemistry, in the very beginning, is purely on qualitative analysis and mechanistic investigation. There are several empirical rules, such as similar compounds react similarly- some changes in the structure and similar changes in the reactivity of the compounds.[93–95] This chapter discusses the effect of substituents (X) in the benzene ring of a reacting molecule under VSC conditions.

3.2 Linear Free-Energy Relationships (LFER)

In 1937, the formulation of the Hammett equation, a linear relationship involving $\log k$ (rate constant) or $\log K$ (equilibrium constant) used as an empirical relation to correlating the structure-property relation of several classes of molecular systems.[93] Initially, the Hammett equation's prime purpose was storing data and predicting new data. The effect of a substituent (X) in the *meta*- or *para*- position of benzene ring upon rate or equilibrium of a reaction is represented in scheme 3.1.

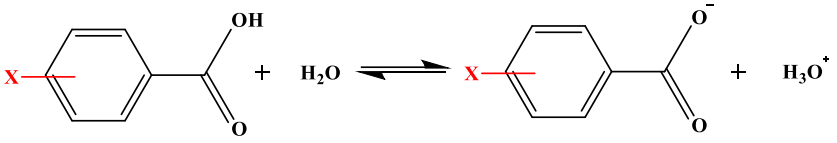

Scheme 3. 1. Solvolysis of benzoic acid and its derivative.

The general form of these correlations can be expressed by:

$$\log k_X = \rho \, log K_X + c \qquad [3.1]$$

$$\log k_H = \rho \, log K_H + c \qquad [3.2]$$

where k_X and K_X are the corresponding rate or equilibrium constants of the substituent, k_H and K_H represent the corresponding rate or equilibrium constants of the unsubstituted benzoate ester. ρ is the slope, and c is the intercept of the straight line in equations 3.1 and 3.2. By comparing its results:

$$log \frac{k_X}{k_H} = \rho \, \sigma \qquad [3.3]$$

Eqn. 3.3 is known as the Hammett relation.

The substituent constant (σ) - measures the polar effect of substituent relative to the hydrogen and independent of the reaction nature. The difference between the logarithm of the ionization constant of substituted benzoic acid and the logarithm of the ionization constant of a benzoic acid gives the value of σ constant for that substituent. With the estimated σ values, ρ values have been obtained by the linear least-square method for a series of substituents in a particular reaction. The reaction constant - ρ depends on the nature of the reaction, medium, and temperature; it measures the susceptibility of the reaction.

In 1953, Jeffe et al. collated data for LFER and studied 371 reactions successfully.[96] By this time, a number of exceptions to the uniqueness of the substituent constant had been noted. The ionization of para-nitrobenzoic acid gave $\sigma = 0.778$, but this value inapplicable to the reactions of phenol or aniline. This comprehensive study criticized the "duality of substituent constants." The equation sought to correlate reactions for side chains and not apply to ortho-substituted benzene derivatives or aliphatic compounds. In the general electrostatic theory of reactivity - the variation has been identified with the relative charge density at the ring carbon atom in which reacting side-chain is attached. Taft's approach was through quantitative separation of the substituent effects into inductive and resonance contributions.[94] His analysis

involves separating polar, steric, and resonance effects in the total impact of structure upon reactivity in ester hydrolysis. The following equation 3.4 evaluates the polar effect of a substituent R in the ester RCO_2R^1:

$$\sigma^* = \left[\log\,(k/k_0)_B - \log\,(k/k_0)_A\right] / \; 2.48 \qquad [3.4]$$

σ^* is the polar substituent constant for R. The rate constants k refer to reactions of RCO_2R^1 as a standard. B and A direct to the basic and acidic hydrolysis for the same R^1, solvent, and temperature. The terms have the following significance; $\log\,(k/k_0)_B$ gives the sum of the polar, steric, and resonance effects of R; $\log\,(k/k_0)_A$ gives the sum of steric and resonance effects of R; the difference provides the polar effect of the substituents. It changes the σ^* value and effect of the linear behavior of linear free energy relationship shown in figure 3.1.

The sigma values with substitution effect permit the identification of rho (ρ) as the relative susceptibility of a particular reaction series to electronic effects. The positive value of ρ indicated that electron-withdrawing substituents (EDS) accelerate the reaction and considerable variation in TS. In contrast, the negative value of ρ showed that electron-donating substituent (EDS) proceeds through the formation of a carbocation in the TS. However, compared to the large number of reactions that give linear relations, several reactions show deviations from linearity (figure 3.1). Sometimes, a clear deviation from Hammett plots is observed using a different substituent constant. Another type of deviation arises when the mechanism of the reaction changes because the presence of the measured rate constant is a composite quantity depending on the rate and equilibrium constant of several reaction steps. In these cases, curvature in the relationship occurs, and several types of linear and non-linear behavior is observed. [97,98] Non-linear Hammett plots have been interpreted as a change in reaction mechanism or rate-determining step (RDS) depending upon the shape of the curvature.

Downward curvature (Figure 3.1 a) has been ascribed to a change in the RDS from changing EDS to EWS. Change in RDS means the formation of TS to its breakdown to products as the substituent in the benzoyl moiety. It can also be concluded that the electronic nature of the substituent in the benzoyl moiety does not influence the RDS. Still, the degree of bond formation in the TS becomes more significant as the substituent changes from EDS to EWS. In contrast, upward curvature (Figure 3.1 b) found for nucleophilic substitution reactions of benzylic systems has been attributed to a change in the mechanism from S_N1 to S_N2, substrates possessing an EDS proceed through an S_N1 mechanism with a negative ρ value, while those

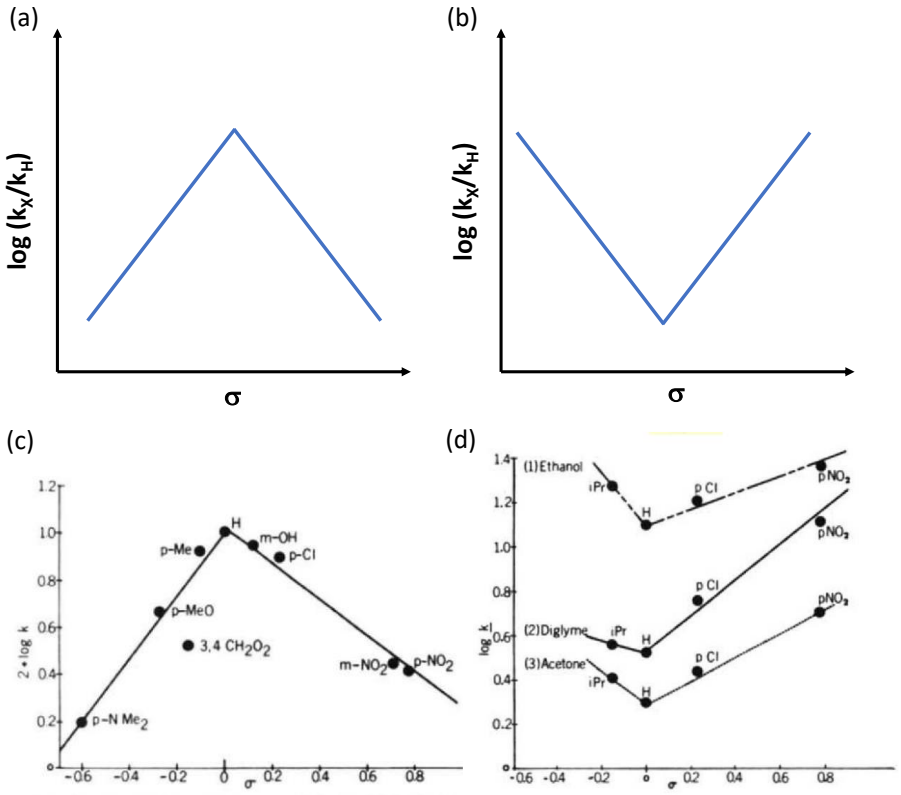

Figure 3. 1. Deviation of Hammett plot for the series of reactions (a) concave downward (b) concave upward (c) Log k versus a for the reaction of benzaldehydes and n-butyl amine.[97] (d) Log k versus σ for the reaction of benzyl chlorides with thiosulfate in (1) ethanol, (2) diglyme, and (3) acetone. [97]

having an EWS proceed through an S_N2 pathway with a positive ρ value. An example of such nonlinear structure-reactivity correlations was studied the reaction of aromatic aldehydes with n-butyl amine under acid catalyzed and neutral conditions.[97] A maximum in the curve occurs near the point for benzaldehyde. This maximum is interpreted as the point where the rate controlling step changes from the reversible addition of amine to aldehyde, which is favored by electron-withdrawing substituents while the subsequent dehydration step is accelerated by electron donating substituents (Figure 3.1 *c*). Concave downward plots have also been observed in Schiff base hydrolysis, the reaction of hydrazones of diaryl ketones, methyl ketones, and aldehydes, the rates of semicarbazone formation for benzaldehydes, the decomposition of benzene diazonium salts, and the acid hydrolysis of substituted amides. Deviations from linearity in the Hammett plot in which the curve tends to be concave upward are thought to be caused by a change in mechanism or transition state brought about by differing effects of electron donors or withdrawers on the course of the reaction. Effects of this type are most often encountered in the reactions of alkyl and acyl halides with nucleophilic reagents. A case illustrative of the concave upward type: the reaction of p- substituted benzyl chlorides

with thiosulfate in solvents of different dielectric constant (Figure 3.1 d). The amount of energy required for desolvation of the thiosulfate ion is less in the less polar solvent diglyme-water than the more polar acetone-water. In addition, it appears that these reactions have different amounts of carbonium ion character. The α carbon becomes "more negative" as the TS is formed from the p −nitro and p −chloro compounds, and "more positive" with the p-isopropyl compounds. Although the preceding examples dealt with the effect of abrupt changes in reaction mechanism, it is believed that for some reactions the mechanism varies continuously.

LFER relates the kinetics versus thermodynamics of a series of reactions, and the Hammett plot describes the relation represented in figure 3.2. The logarithm of an equilibrium constant (K) is proportional to the standard free energy:

$$\log K = -(\Delta G^0 / 2.3\, RT) \qquad [3.5]$$

and the logarithm of a rate constant (k), according to transition state theory, is proportional to the standard free-energy of activation:

$$\log\left(\frac{k}{R.T/N_A.h}\right) = -\left(\frac{\Delta G^{\neq}}{2.3 \times R \times T}\right) \qquad [3.6]$$

h is the Planck constant, T is thermodynamic temperature, R is universal gas constant and N_A is the Avogadro number. A series of reactions differing by substituting the reactant shows the linear relationship between the change in enthalpies and entropies of activation (Eqn. 3.7).

$$\Delta H_i^{\neq} = \alpha + \beta \Delta S_i^{\neq} \qquad [3.7]$$

in which α and β are constants. This behavior is called the enthalpy-entropy compensation effect.[99] It can occur when $\Delta G_i^{\neq}$is approximately constant within the series of reactions while $\Delta H_i^{\neq}$ and $\Delta S_i^{\neq}$ vary significantly. The quality β has a temperature dimension and is defined as the isokinetic temperature, and the corresponding behavior is called the isokinetic relationship (IKR). At temperature β, all the reactions in the series should have the same rate. The compensation and isokinetic effects are not necessarily synonymous, and one occurrence does not imply the other.

The difference between compensation and isokinetic effect stems from the different statistical criteria that are used to decide their existence. The isokinetic effect judgment is based on how close the reaction rates are to each other at a temperature. These effects are empirical

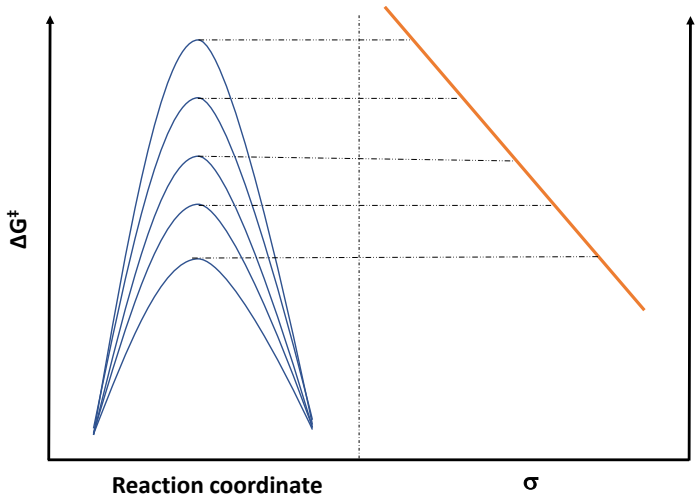

Figure 3. 2. A TS diagram for single-step reactions and corresponding linear Hammett plot.

relationships generated from the statistical analysis. IKR relationship is best to test with Arrhenius lines describing the kinetics of the reaction series is necessary (Figure 3.3a). The significant compensation effect, especially in the solution phase, is due to the redistribution of the energy distinguishable subspecies. It is most likely arising due to a similar physical origin. Figure 3.3 b shows that alkaloids are all separable on the basis of their varying basicity and exhibit a T_{iso} above the experimental temperature range which illustrates fact that selectivity decreases with increase of temperature.

Theoretically, it assumes that reactant molecules distributed within the potential well into discrete energy levels and there is energy exchange with the "heat bath." For a chemical reaction to occur, a reaction crosses the activation barrier that constitutes a point of no return. This system can be expressed as balanced, where for each energy level, the change in the particle density is described by adding molecules jumping into the level and subtracting those that leave it. Under the condition $E_a >> k_B T$, the reaction fulfilled the criteria and crossing the activating barrier. Though it is established that the IKR relationship results from particular energy resonance between reacting molecules and their environment, the detailed mechanism is still not investigated.[100] Linear free energy relationships (LFER) are helpful in two respects. One is the LFER correlation of experimental data from a new reaction series with those of known series; it is useful in explaining reaction mechanisms. On the other hand, LFERs can be used to predict the rate and equilibrium constants produced by changes in the reactant structure or the reaction medium. Crowell et al. showed that the rate could be more sensitive to the different solvents, but in each case, the trend of the Hammett plot remains the same.

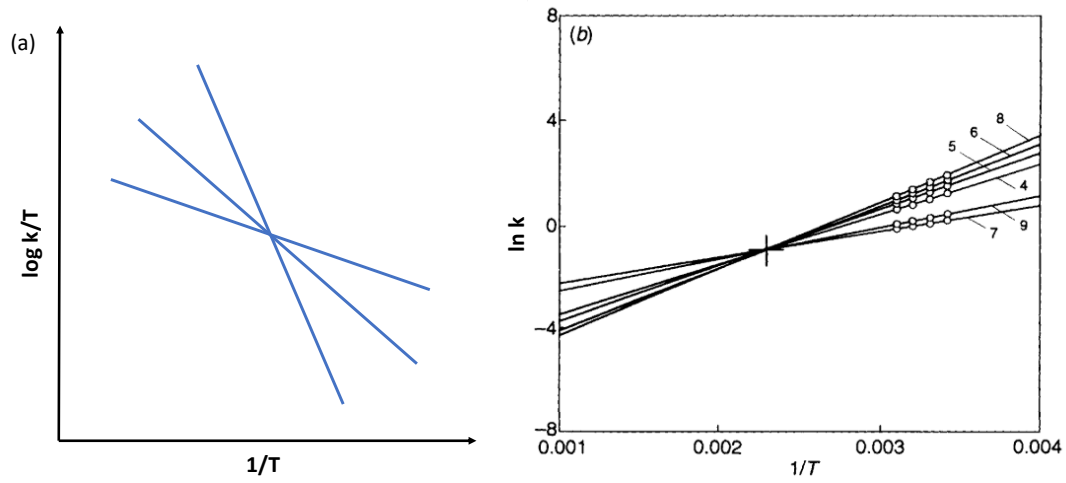

Figure 3.3. (a) Hypothetical cases for IKR occurrence for a reaction series (b) Van't Hoff plots of the alkaloids belonging to Dihydrosanguinarine (4), Berberine (5), Stilopine (6), Allocryptopine (7), Sanguinarine (8), Protopine (9).

3.3. Reaction Series studied for LFER under VSC

We studied the effect of the substituent in the benzoyl group on the apparent rate and the extracted activation parameters in an FP-cavity configuration. The transesterification of 4-nitrophenyl benzoate esters with mild base-TBAF in methanol was carried out by varying the substituent on the benzoate ring. The reactions were followed by monitoring the appearance of 4-nitrophenoxide at 400 nm using a Cary 5000 UV-VIS spectrophotometer. All the reactions were assumed to undergo a pseudo-first-order condition at room temperature. Different substitutions on *para*-nitrophenyl X-benzoates (X*: m-*CH_3*, p-*CH_3*, m-*OCH_3*, m-Cl, and p-Cl*) influence the reaction rate due to electron-withdrawing and electron-donating groups, which is sensitive towards the moiety of the acyl carbonyl group.[101] The synthesis of all the derivative *p*-nitrophenyl benzoate, *p*-nitrophenyl *m*-toluate (*m-*CH_3), *p*-nitrophenyl *p*-toluate (*p-*CH_3), *p*-nitrophenyl *m*-anisate (*m-*OCH_3), *p*-nitrophenyl *m*-chlorobenzoate (*m-Cl*) and *p*-nitrophenyl *p*-chlorobenzoate (*p-Cl*) was done in the laboratory and characterized by IR and NMR spectroscopy. The esters are stable at room temperature and used after recrystallization, which confirms the system's purity. All the fresh solutions of benzoates were prepared, 0.1 M in isopropyl acetate (IPAc) and stock solution of TBAF 0.1 M in methanol. Solvolysis was initiated by 190 μl of benzoates with 10 μl of TBAF. The final concentration of 0.1 M of solute and 0.05 M of reagent kept the ratio of 20: 1 and followed pseudo-first-order kinetics.

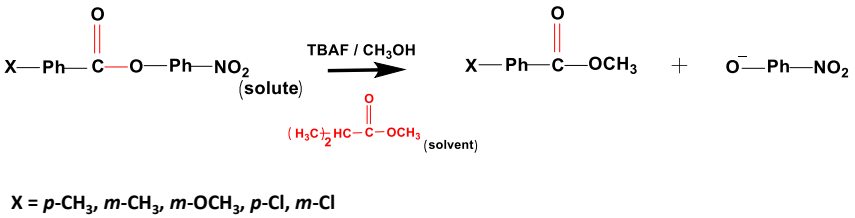

Scheme 3. 2. Scheme of PNPB transesterification reaction.

Strong electron-withdrawing -nitro group (σ high) and electron-donating amino group (σ low) substituted derivatives is the extreme case of the reaction. From experimental point of view the study of fast reaction in present set up is very difficult task. Because of the manual injection of the reaction mixture in microcavities. On the other hand, slow reactions are possible to study. This work aimed to examine the effect of X substituent in the benzoyl fragment under VSC. The nature of the substituent X was selected in such a way that two groups are electron-donating (*m-CH3*, *p-CH3*) with $\sigma = +ve$, having *m-CH3* (+I) and *p-CH3* (+I, +R). On the other hand, two substituents are electron-withdrawing (*m-Cl*, *p-Cl*) with $\sigma = -ve$, having a dominant (-I) effect. At the same time, *m-OCH3* is very close to unsubstituted benzoate because of the mild inductive effect. The nucleophilic attack on the C=O carbon and formation of the negatively charged tetrahedral TS is the reaction's rate-determining step (RDS).[102] All the derivatives follow a similar reaction mechanism, whereas the substituents at m- and p-position modify the reaction rate, either by inductive $(\pm I)$ or/ and by resonance $(\pm R)$ effects. Here, the idea is to look at the electron density effect on the reaction rate under coupling with the vacuum field. Electron donating substituent stabilizes the resonance structure in the ground state and increases the activation enthalpy for the reaction. It leads to the weakening of the reactivity for that benzoate ester. On the other hand, enhancement of the electron-withdrawing power of the substituent is accompanied by destabilization of the ground state.

Table 3. 1. Vibrational frequency of carbonyl band ($C=O_{str}$) in the given esters.

SL. No.	Compound	$C=O_{str}(cm^{-1})$
1	PNPB	1744
2	*m*-CH3	1742
3	*p*-CH3	1741
4	*m*-OCH3	1743
5	*m*-Cl	1748
6	*p*-Cl	1741

Therefore, the enthalpy component considerably decreases, and the reactivity increases. The mechanism of the transesterification reactions can be characterized by an isokinetic relationship and compensation plot. The linear regression of the Hammett plot gives the positive value for $\rho = +0.89$, indicating that electron-withdrawing substituent accelerates the nucleophilic attack due to an increase in the electrophilicity of the carbonyl carbon atom. Therefore, the substitution effect in the benzoyl moiety is expected to give helpful information about the reaction mechanism. It suggests acyl-transfer reactions occur by stepwise mechanism, and the formation of TS is the rate-determining step and is consistent with the mechanism involving the tetrahedral intermediate.

VSC experiments were conducted in an FP-cavity, and the mirrors were coated on BaF_2 windows to observe the reaction using infrared and UV-VIS spectrophotometers. The mirrors are prepared by coating Au of 10 nm, and a demountable flow cell configuration was used for all the measurements. After assembling the mirrors in the flow cell, the pathlength was

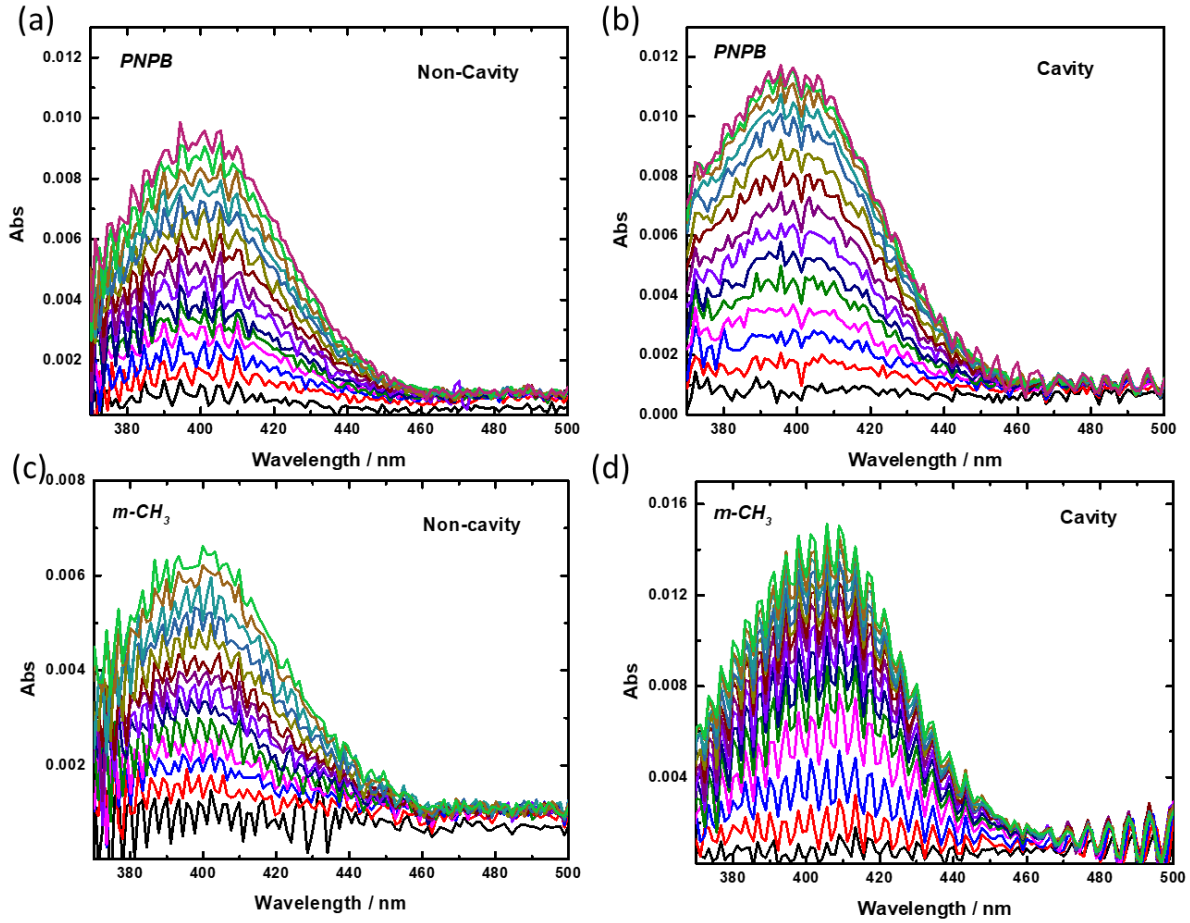

Figure 3. 4. Scan kinetics for the formation of *PNP*- ions from *PNPB* and *m-CH₃* (a, c) non-cavity; (b, d) ON-resonance cavity.

controlled using a mylar spacer of approximate thickness 12 μm. The flatness of the mirror is ascertained by forming a homogeneous display of Newton's ring at the center of the cavity. In this configuration, we achieved a Q-factor (finesse factor) of ~60, with an FWHM of 30 cm^{-1}. The non-cavity experiment was performed without the mirrors by keeping all other parameters fixed. The whole spectral region was recorded using the scan kinetics method in the UV-VIS spectrometer in the range of $350 - 500\ nm$. Kindly note that all the spectral measurements were conducted in a static condition by closing both the inlet and outlet after injection of the reacting solution. Each spectrum was collected in the 16 $seconds$ intervals by keeping the slit bandwidth of 5 nm. The evolution of the para-nitro phenoxide ion (PNP-) was recorded at 400 nm and the kinetic rate of the reaction was calculated from the scan plot, as shown in figure 3.4. Here, some reactions are faster and the corresponding time interval are shorter to get more points for linear regression fitting. In such cases, the temporal scan won't allow us to obtain the initial rate for (*m-Cl and p-Cl*). So, we collected the single point kinetics at 400 nm with an interval of 1 $second$ and SBW of 5 nm; plotted in reaction rate (Figure 3.5). To get a homogenous mixing between the reactant and TBAF, we mixed the solution thoroughly using the same syringe before injection. This process may take roughly 40 seconds (dead time) before we start the spectral measurements. Kinetic traces are recorded using the following first-order equation:

$$\ln\left(\frac{A_t}{A_0}\right) = -k_{app}t \qquad [3.8]$$

Apparent rate constant for unsubstituted molecule (average of three measurements at room temperature; 298 K):

$$k_{app} = 1.05\ \times 10^{-3}\ sec^{-1}$$

Consider at time t the remaining concentration of the reactant is 96%

$$A_t = 0.96A_0$$

Substitute the value of k_{app} and A_t in equation 3.8:

$$\ln\left(\frac{0.96A_0}{A_0}\right) = -1.05\ \times 10^{-3}\ t$$

$$\ln(0.96) = -1.05\ \times 10^{-3}\ t$$

$$-0.04082 = -1.05 \times 10^{-3}\ t$$

$$t \sim 40\ sec \text{ (dead time)}$$

The above calculation indicates that only 4 % of the reaction occurs outside the measurement data (dead time loss). All the cavity and non-cavity show a clean first-order fitting. A_{inf} has obtained after 5000 $seconds$ roughly 10 times the half-time (99.9 % conversion) and found to be 0.037 for unsubstituted benzoate shown in figure 3.5. This value was used for all apparent rate calculations in the subsequent experiments.

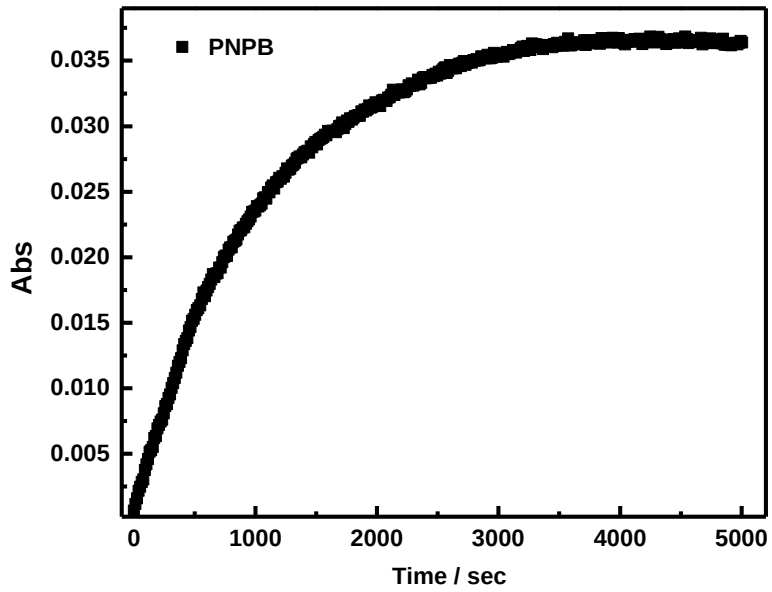

Figure 3. 5. Formation of PNP- ions during the reaction for solvolysis of PNPB (non-cavity) kept for 5000 $seconds$.

All the solutions of benzoate ester derivatives were prepared in IPAc solvent and VSC experiments were conducted by coupling 7th mode of the cavity with C=O stretching band at 1739 cm^{-1} of the solute-solvent system. Coupling of the C=O_{str} was observed using FTIR spectrophotometer and gives a Rabi splitting energy of 136 cm^{-1} with $VP+$ and $VP-$ at 1814 cm^{-1} and 1678 cm^{-1}, respectively. All the derivatives of the benzoate esters used in the experiment have matching C=O stretching bands with respect to the solvent molecules.

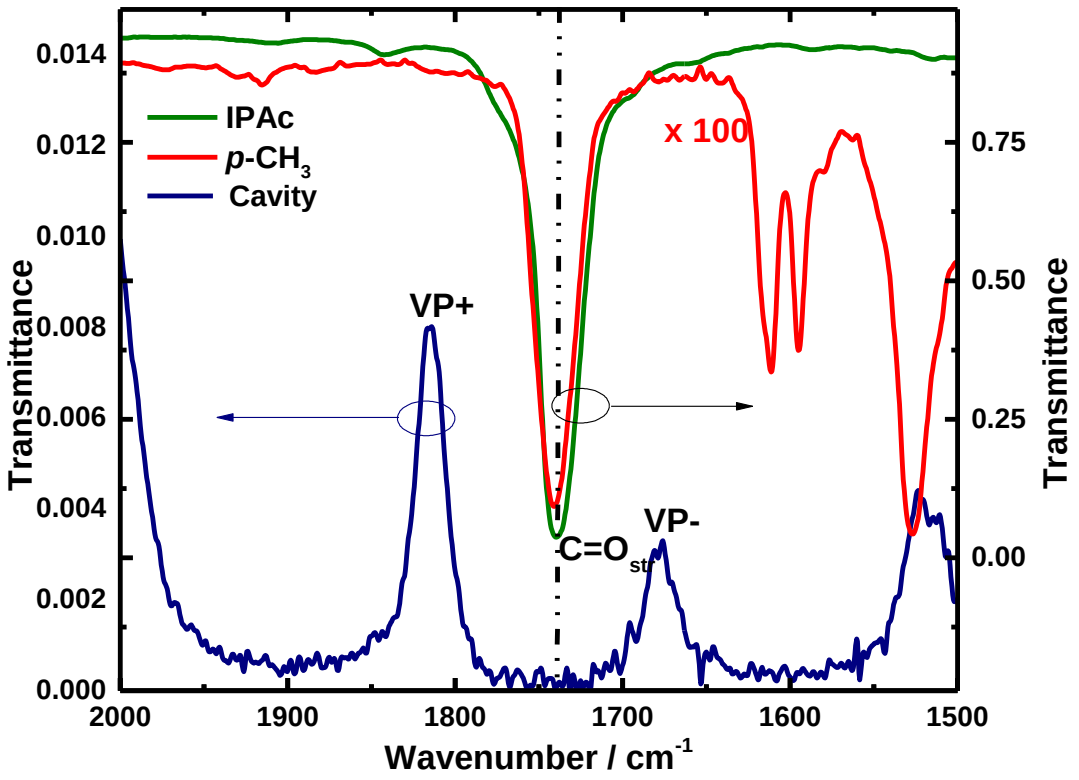

Figure 3.6. FTIR spectra of neat IPAc solvent (green trace), *p-CH₃* in chloroform (red trace) and cavity ON-resonance $7th$ mode coupling with C=O$_{str}$ band of solute and solvent molecules show the formation of vibro-polaritonic ($VP+$ *and* $VP-$) states.

It allows the system to enter the cooperative VSC condition (Figure 3.6). There is a limitation that direct coupling of the solute won't reach the strong coupling regime. Hence, the solute-solvent coupling is the only option to satisfy the above criteria. Please note that the solute concentration is 100 *times* lower than the solvent concentration.

3.4 Result and Discussion

Initially, we optimized the condition for kinetic trace measurement with unsubstituted derivative and the reaction rate calculated for PNPB in the non-cavity condition is: $k_{app} = 1.05 \times 10^{-3}\ sec^{-1}$. The experiment after ON-resonance coupling of the C=O$_{str}$ band of solute and the solvent molecules in the cavity is: $k_{app} = 1.55 \times 10^{-3}\ sec^{-1}$. The reaction rate changed by approximately 1.5 $times$ under the ON-resonance condition. Similarly, the kinetic experiments were performed for all the derivatives under similar experimental conditions and the reaction rates are plotted in figure 3.7 (kinetic action spectrum). It has been found that in non-cavity plotting $log\frac{k_X}{k_H}$ *versus* σ gives a straight line, as it follows the linear free energy

relationship. Here, we have taken the σ values from the reported literature, and ρ is the slope of the linear regression fitting parameter. The value of ρ of PNPB-based transesterification in IPAc is $+\ 0.89$. This value may change with the reaction condition and solvent medium. As in the previous studies, the FSR calculation was done in a similar manner discussed in the section 2.4. Here, again the FSR calculation of the FP-cavity was done in the UV-Vis spectrophotometer. During the FSR calculation the scanning error in wavelength is $\pm 1\ nm\ (at\ 700\ nm)$; that can give a propagation error for wavelength to wavenumber conversion. We always check the FSR after the reaction kinetics and make sure about the consistency in each measurement.

Interestingly, the experiment performed for all the derivatives in the cavity under ON-resonance conditions and the k_{app} change from 1.5 to 6 times for different substituents obtained from the linear fitting of the plot in figure 3.7; the values are given in table 3.2. For different substituents moving from electron-donating to electron-withdrawing changes the rate enhancement. The line shape of the kinetics versus wavenumber (Figure 3.8) of the different derivatives changes because the position of the C=O stretching band of the reaction center varies from one derivative to another. The apparent rate calculated by moving the cavity mode position from ON to OFF-resonance condition follows the line shape of the $C{=}O_{str}$ band. More clearly, the rate enhancement follows the vibrational envelope of both the solute and solvent molecules indicated in figure 3.8. These are the clear indication of a cooperative mechanism under VSC conditions. Also, note that the non-cavity pathlength can be assessed by observing shallow interference in the flow cell (Air-BaF_2 interface), and the changes in the pathlength within this range won't affect the apparent rate of the reaction. Another critical point is that the solution must be homogeneous so that the light beam of the UV-VIS spectrophotometer can pass through the homogeneous medium of the cavity/non-cavity to obtain clean kinetic traces. It will also help better analyze FSR and compare the tuning experiments.

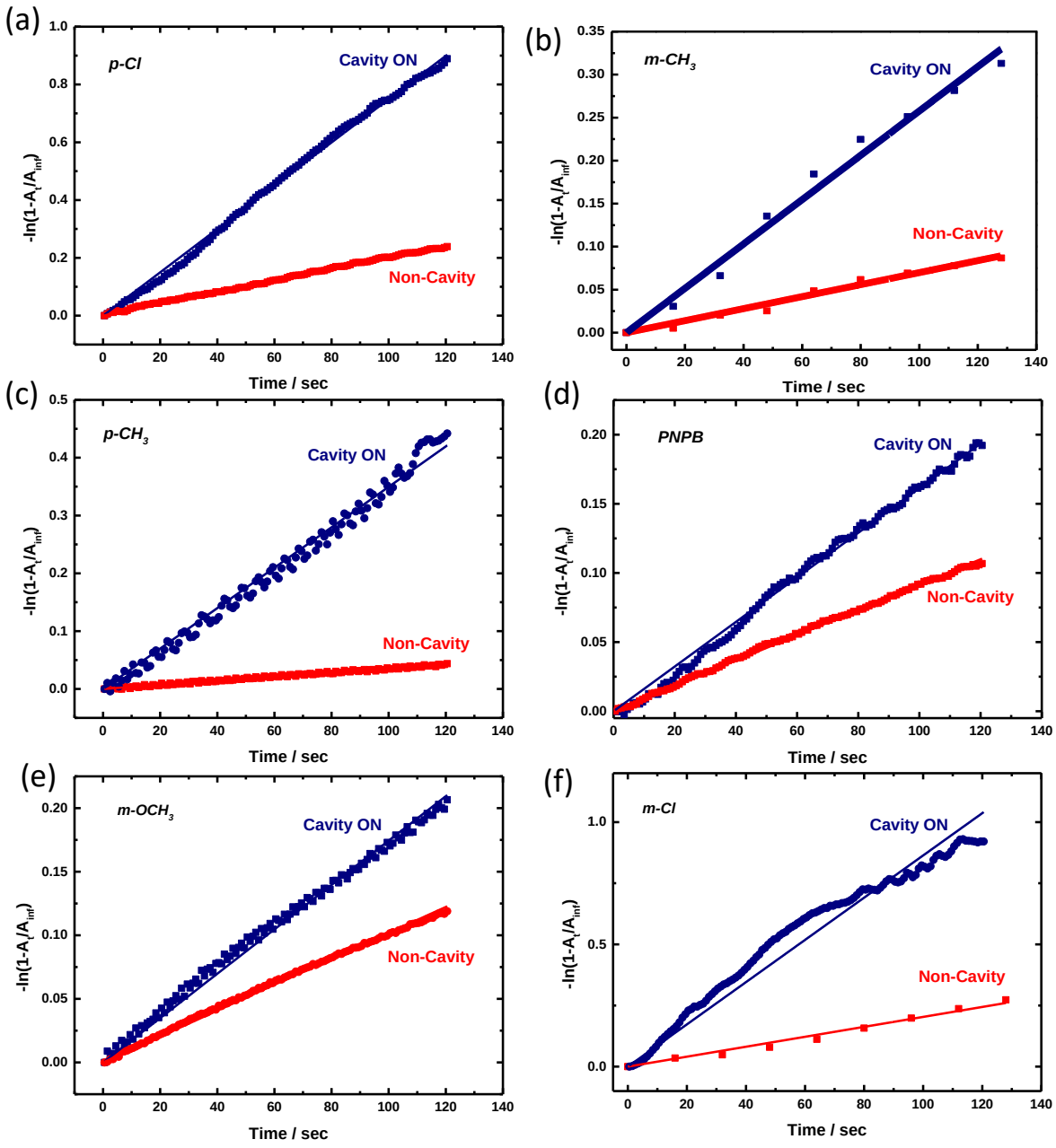

Figure 3. 7. Reaction rate plot for non-cavity and ON-resonance cavity (a) *p-Cl*, (b) *m-CH3*, (c) *p- CH3*, (d) *PNPB*, (e) *m-OCH3*, (f) *m-Cl*.

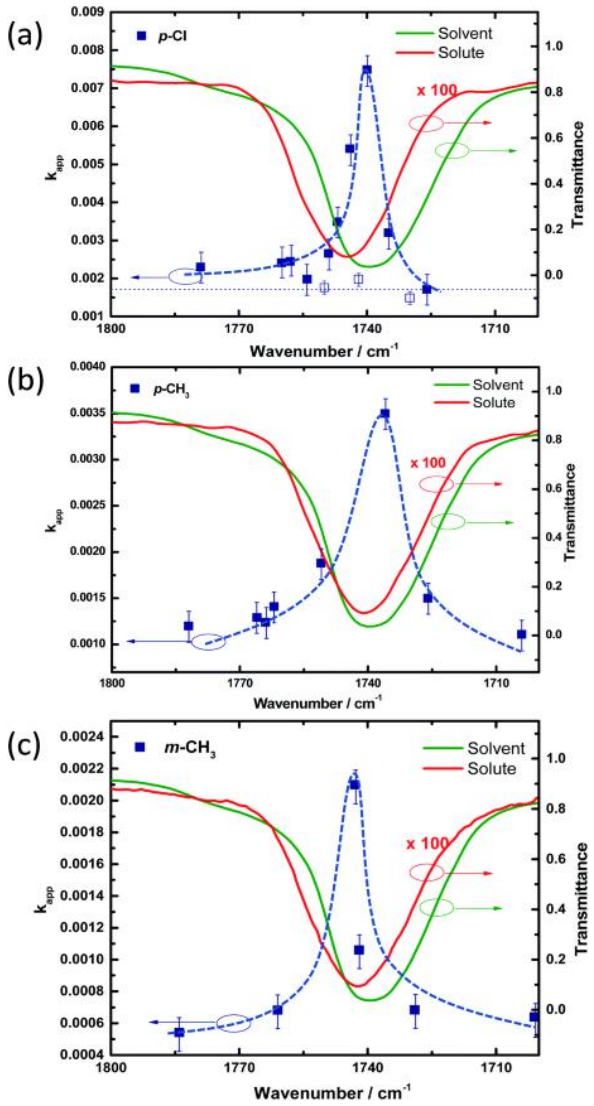

Figure 3.8. Tuning of the 7th mode position moved slowly from 1680 cm^{-1} to 1780 cm^{-1} in each experiment, and the corresponding k_{app} was plotted with the IR transmission spectra of the C=O_{str} band of solute (red trace) and solvent molecules (green trace). An increase in k_{app} was observed (blue squares) at the ON-resonance conditions for (a) *p-Cl*, (b) *p- CH_3*, and (c) *m-CH_3* derivatives [blue dotted curve is guiding to eye].

Table 3.2. k_{app} of cavity and non-cavity experiment as plotted in the figure 3.9.

SL. No.	Compound	Non-cavity k_{app} (s^{-1})	Cavity k_{app} (s^{-1})
1	*PNPB*	1.05 x 10^{-3}	1.55 x 10^{-3}
2	*m-CH_3*	7.73 x 10^{-4}	2.58 x 10^{-3}
3	*p-CH_3*	5.54 x 10^{-4}	3.50 x 10^{-3}
4	*m-OCH_3*	1.19 x 10^{-3}	1.86 x 10^{-3}
5	*m-Cl*	1.63 x 10^{-3}	7.26 x 10^{-3}
6	*p-Cl*	1.49 x 10^{-3}	7.50 x 10^{-3}

Interestingly, experiments conducted in the cavity condition and their corresponding plot of $log\frac{k_X}{k_H}$ *vs.* σ shows the breaking of the linear free energy relationship (Figure 3.9). For the cavity, the value of σ is kept constant as that of non-cavity and k_H value is taken from the ON-resonance condition of the unsubstituted benzoate (PNPB) derivative. Recently, Bhattacharyya et. al. also demonstrated that electrode can polarize the molecules in a similar way of the electronic structure effect as reflected in the Hammett equation.[137] The equivalence of a polarizing electric field at the electrochemical interface and a functional group at the para-position shows a shift in electronic charge density. Here, all the conditions were the same as

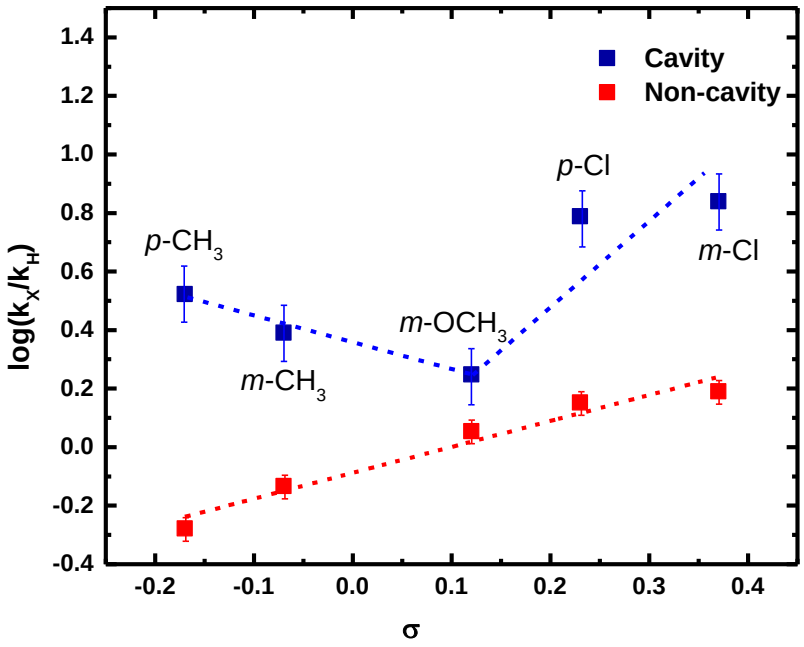

Figure 3. 9. Hammett plot for a series of ester solvolysis (*p-CH3, m-CH3, m-OCH3, p-Cl, and m-Cl*) in non-cavity (red squares) and ON-resonance cavity conditions (blue squares).

in the non-cavity experiment except the VSC effect. Substituents with $\sigma = -ve$ show a negative value of ρ, whereas substituents with $\sigma = +ve$ show a positive value of ρ at the ON-resonance condition. It can be suggested that substituents are having a different density of electron-donating and withdrawing groups get perturbed under VSC. Here, C=O oscillators coupled with the electromagnetic field modify the electron density in its surroundings. The substitution effect reshuffle under VSC of solute-solvent coupling as compared to non-cavity. At the same time, the electric field may affect the σ value, which is challenging to evaluate for this experiment. Literature reports suggest that deviation in the Hammett plot is probably due to a change in the mechanism of the reaction- concave upward or change in the rate-determining step- concave downward.[97]

To understand the effect of cooperative VSC, we studied kinetics by choosing a different solvent. Unlike IPAc, acetonitrile is transparent around $\sim 1750\ cm^{-1}$ and can be used as a control to study the effect of vibrational overlap. The reaction rate was observed using 0.1 M of *p*-nitrophenyl *p*-toluate dissolved in acetonitrile and performed in cavity and non-cavity

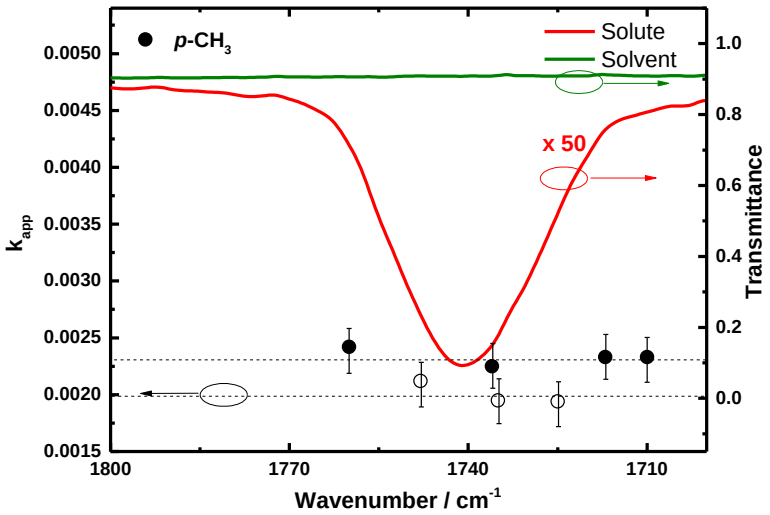

Figure 3.10. IR spectrum of acetonitrile (green trace), solute *p-CH₃* (red trace), and the calculated reaction rate k_{app} for detuning experiment of cavity (dark black circles) and non-cavity (empty black circles).

conditions. The tuning experiment suggests that reaction rate was not affected even if the 7th mode crosses the C=O$_{str}$ of the solute molecules as shown in figure 3.10. The solute concentration is very low, so coupling strength is very small or negligible. We do not observe any change in the reaction rate under such conditions. These control experiments also rule out the possibility of local thermal effect (heating) due to an infrared cavity mode. i.e., the presence of an infrared cavity mode is not a criterion for rate enhancement.

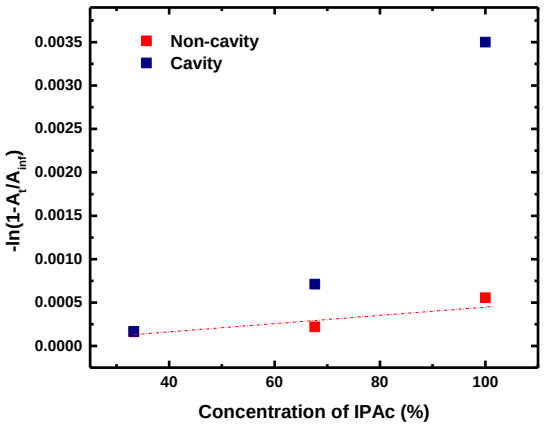

Figure 3.11. Concentration dependence experiment by mixing anisole and IPAc in different ratios and the corresponding reaction rate *p-CH₃* for non-cavity (red squares) and ON-resonance cavity (blue squares).

Similarly, we looked into the rate enhancement effect by changing the coupling strength of the available oscillators of C=O_{str}. It can be possible by mixing the active solvent with another solvent with similar polarity. We have chosen anisole for that purpose and fixed the 0.1 M of *p*-nitrophenyl *p*-toluate. Different batches of solutions were prepared by mixing anisole in IPAc ranging from 33 % to 100 %. The reaction under VSC increases with the Rabi splitting. Changing the concentration of the C=O oscillators (IPAc) shows a non-linear behavior in the reaction rate; it reflects the complex effect of VSC on the chemical landscape.

In contrast, the coupling strength varies linearly with respect to the square root of concentration. This experiment observation provides further evidence on the VSC effect on chemical reaction rate and excludes the role of thermal effect in controlling the chemical reactions. Similar behavior was observed in C-Si bond-breaking experiments studied reactions under VSC.[70-71] The non-linear behavior indicates the complex role of reaction dynamics under coupling conditions. It needs high-level theoretical intervention to fully understand the role of vibrational relaxation pathways in the system.

The following question can be asked to understand the role of cooperative VSC in chemical reactions. Can VSC change the reaction mechanism or the rate-determining step? The idea of an isokinetic relationship was tested for the same system; it gives insight into the reaction mechanism and hence the variation of LFER and the Hammett equation. Activated parameters were extracted for some of the derivatives by temperature-dependent studies.[103] In the first case, the Eyring equation plotted for unsubstituted (PNPB) in cavity and non-cavity is shown in figure 3.12 d. The change of enthalpy and entropy from non-cavity to cavity is given in Table 3.3. It indicates that PNPB enthalpy of activation decreases from 71.3 $kJmol^{-1}$ to 28.7 $kJmol^{-1}$ and the entropy of activation also decreases from $-19.2\ kJK^{-1}mol^{-1}$ to $-59\ kJK^{-1}mol^{-1}$.

The results show a similar trend to the previously reported PNPA ester solvolysis process. The same has been calculated for electron-donating substituent (*p*-CH_3) in figure 3.12 a, in which enthalpy of activation increases from 79.2 $kJmol^{-1}$ to 139.3 $kJmol^{-1}$ and the entropy of activation also increases from $-13.2\ kJK^{-1}mol^{-1}$ to $-52.2\ kJK^{-1}mol^{-1}$. The significant change in the activation parameters suggests that the change in free energy of activation from the cavity to non-cavity is $-5.23\ kJmol^{-1}$. The complete reshuffling of the enthalpy and entropy component of the activation parameters is drastic for a ground state VSC process. This

observation can be similar to solvent-triggered chemical reaction control in some of the reactions reported in the literature.

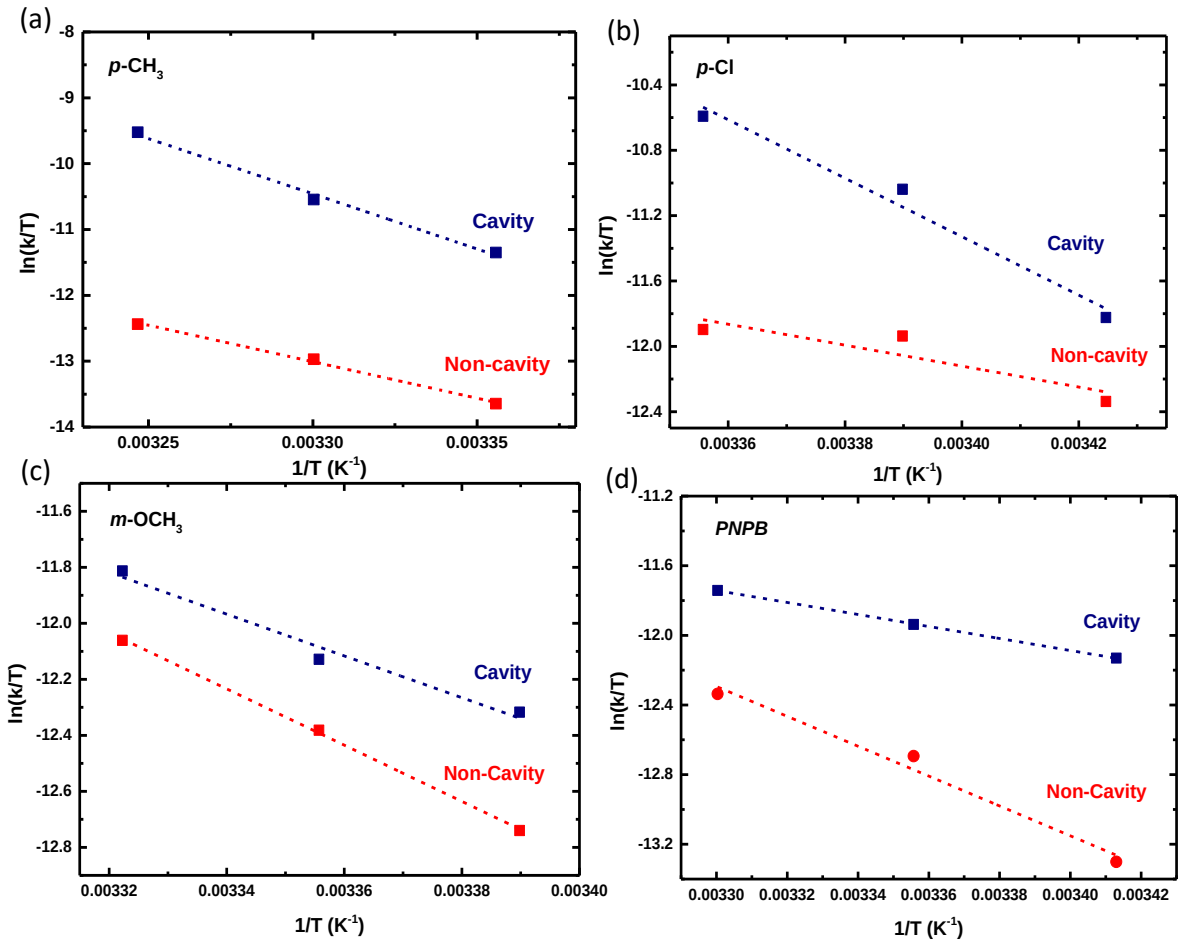

Figure 3. 12. Temperature dependence experiment for non-cavity and cavity;(a) *p-CH₃*, (b) *p-Cl*, (c) *m-OCH₃*, (d) *PNPB*.

Table 3. 3. Thermodynamic parameter extracted from the linear regression fit of figure 3.12.

SL. No.	Name	σ	$\Delta H^{\ddagger}_{NC}$ (kJmol^{-1})	$T\Delta S^{\ddagger}_{NC}$ (kJK^{-1}mol^{-1})	$\Delta H^{\ddagger}_{C}$ (kJmol^{-1})	$T\Delta S^{\ddagger}_{C}$ (kJK^{-1}mol^{-1})	$\Delta\Delta G^{\ddagger}_{C\text{-}NC}$ (kJmol^{-1})
1	*p*-CH_3	-0.17	79.2	-13.2	139.3	52.2	-5.2
2	*p*-Cl	0.23	53.5	-34.9	148.7	63.8	-3.2
3	*m*-OCH_3	0.12	83.5	-6.1	62.0	-26.8	-0.9
4	PNPB	0	71.3	-19.2	28.7	-59.0	-2.8

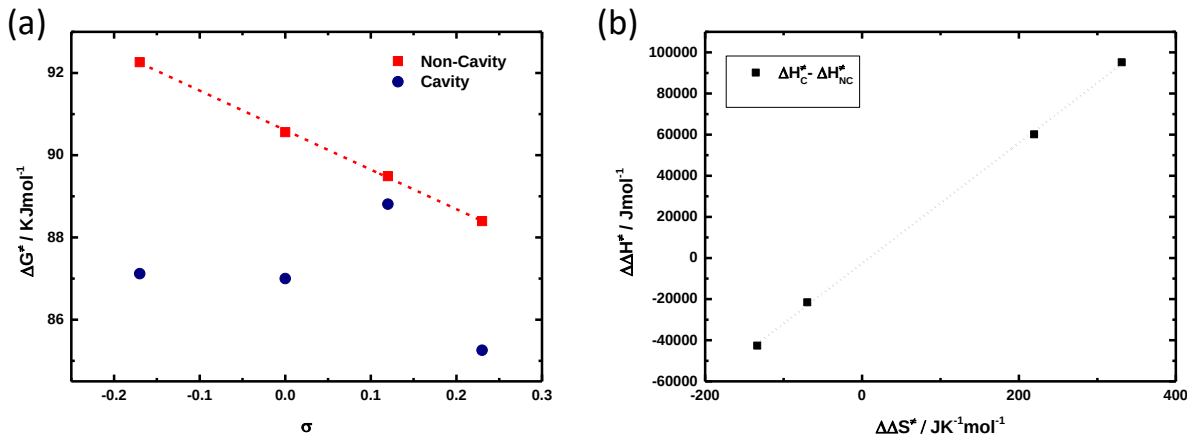

Figure 3. 13. (a) Thermodynamic relation between the free energy of activation versus σ for the cavity (blue circles) and non-cavity (red squares); (b) Enthalpy-entropy compensation plot for cavity versus non-cavity experiments is listed in table 3.3.

It is also very interesting to note that the electron-withdrawing substituent *p-Cl* follows a similar trend as that of *p-CH₃* under VSC conditions. In the case of *m-OCH₃*, the activation parameter shows the least variation as expected from the kinetic data. The thermodynamic data indicates that the cavity reshuffles the enthalpy-entropy distribution in the system. Under cavity, $\Delta G^{\neq}$ decreases for both electron-donating and withdrawing substitutes, and the system is eventually becoming entropy-driven.

Thermodynamic comparison is crucial for the cavity and non-cavity to understand the compensation effect of activation parameters in the TS. Plotting $\Delta\Delta H^{\neq}_{C-NC}$ against $\Delta\Delta S^{\neq}_{C-NC}$ gives a straight line shown in figure 3.13 b. There is an excellent linear correlation between enthalpy and entropy changes which demonstrates the example of the compensation effect.[99] The free energy of activation does not change as entropy compensates for the enthalpy of activation. However, plotting the change in free energy $\Delta\Delta G^{\neq}_{C-NC}$ versus temperature at which a common intersection point describes the kinetics of a series of chemical reactions. It indicates that the reaction rates can be close at the isokinetic temperature.

The kinetic and thermodynamic experiment shows that VSC plays a crucial role in controlling chemical reactions. The deviation of the structure-reactivity relationship under VSC may have a different origin. The electron density flow between the substituent and the reaction center through *sigma* and *pi* bonds and electron donating-withdrawing plays a critical role in VSC. The VSC of the solute-solvent C=O_{str} band favor/disfavor the electron density flow through the sigma and pi-bond. *p-CH₃* shows +R and +I effect, reaction rates faster than *m-CH₃* is having +I effect. On the other hand, *p-Cl* and *m-Cl* have both +R and -I effect but -I dominate and get amplified under VSC. It is important to note that $T\Delta\Delta S^{\neq}_{C-NC} > \Delta\Delta H^{\neq}_{C-NC}$; for *p-CH₃*

and *p-Cl* indicates an entropy-driven process triggered through cooperative VSC. Solute-solvent interaction is a complex phenomenon and challenging to understand under VSC. It requires more theoretical explanation with experimental work. Many factors can control the reaction, including- the intramolecular vibrational relaxation process within the solute molecules, self-dipolar interactions and solute-solvent vibrational energy transfer processes, etc.[104–108]

3.5 Conclusion

The above experiments demonstrate breaking the linear free-energy relationship by cooperative VSC of the solute and solvent molecules.[109] Thermodynamics suggests that the mechanism might remain the same under cavity catalysis conditions. The rate enhancement varies from one substitute to another, and non-linear behavior is due to internal vibrational relaxation between the substituent and the reaction center. The compensation plot suggests that energy density reshuffles the TS under cavity coupling. There is no information about the substituent constant (sigma) values in cavity and non-cavity conditions. There may be a change in resonance stabilization in the ground state under VSC, which may depend on the substituents. It can be the prime reason for the non-linear behavior of LFER. Here, cooperative VSC boosts a chemical conversion process. All the above evidence supports the selective coupling of vibrational states that can precisely control the reactivity of a chemical bond.

Chapter 4

Improving Enzyme Catalytic Efficiency by Cooperative Vibrational Strong Coupling of Water

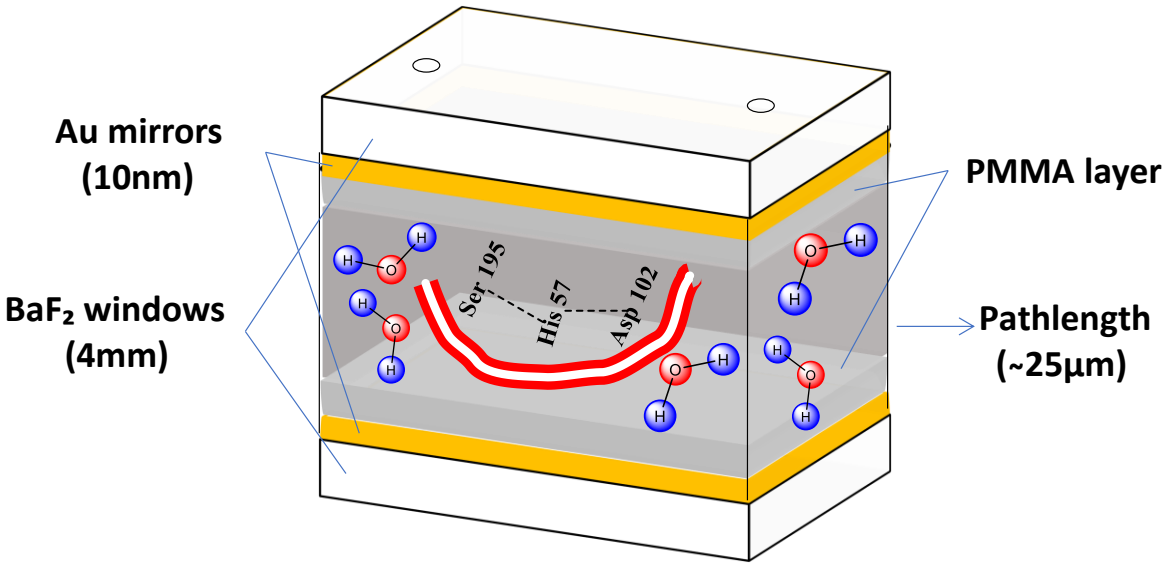

4. 1 Introduction

Light-matter strong coupling can be utilized to slow down or speed up chemical reactions by selectively coupling the responsible vibrational states. Previous chapters deal with small molecule reactions and the ground state reactivity modification by VSC. The modification of properties is not limited to small molecular systems; a large biomolecule can also thrive under selective VSC conditions. It has already been demonstrated that protein vibrations can be coupled to an IR photon in an FP-cavity configuration.[55] Effects of VSC can be studied for the enzyme since the absorption bands lie in the mid-infrared region.[110,111]

Infrared spectroscopy is one of the oldest techniques to study the secondary structure of polypeptides. It showed that the "amide I" band observed nearly $1650 - 1660\ cm^{-1}$ for α-helical conformation and $1630 - 1640\ cm^{-1}$ for β- stands. Protein amide bands are usually termed amide I-VII and amide A and B bands and are mainly used to assign the configuration of biomolecules. Enzyme catalysis is generally involved in a complex multi-step process and is mainly explained through a lock and key mechanism.[112] However, it has been observed that a small amount of enzyme can accelerate a chemical reaction, sometimes up to an order of magnitude. The correct orientation of the substrate can reduce the entropy of activation. The charge distribution at the active site and geometry of the binding site reduces the enthalpy for the enzyme-catalyzed reaction. Ariel Warshel et al. developed the idea of the electrostatic effect on enzyme activation by both ground state and TS stabilization processes.[113] Significant electrostatic contribution mainly originates from the preorganized polar environment of the enzyme active sites.[114] Energy-based consideration motivates us to couple the enzyme in the vacuum field.

One of the very first reports by Vergauwe et al. on the coupling of the biomolecules with the amide I band and γ-COO− (an asymmetric stretching band) of poly-L-glutamic acid (PLGA); amide I of bovine serum albumin. Later, the same group studied the activity of protease pepsin under the VSC of water molecules. Water plays an essential role in deciding the conformation of enzymes or any macromolecular protein systems due to the possibility of extended H-bonding. The effects of VSC on the liquid-water environment can slow down the proteolytic activity of the coupled system. The aspartic acid residues in the active site activate a water molecule as a

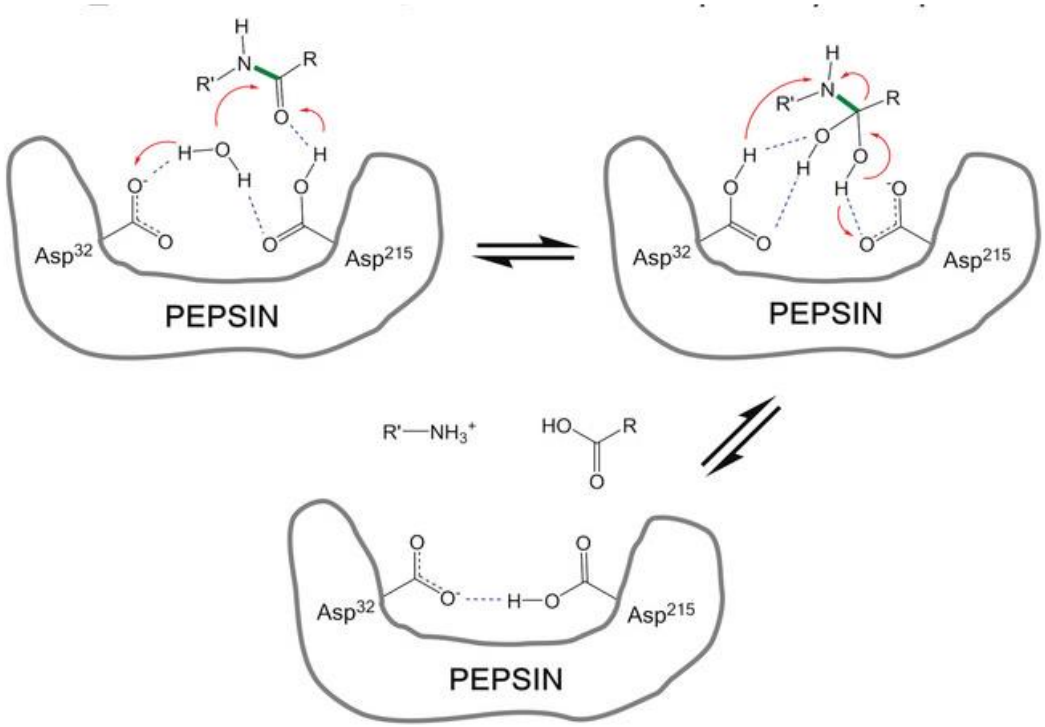

Scheme 4. 1. Mechanism of peptide bond cleavage in the active site of pepsin. (Vergauwe et al. 2019)

nucleophile for the attack on the carbonyl carbon of the amide bond (Scheme 4.1). They strongly coupled the water molecules having two prominent absorption peaks in the IR region, O-H stretching absorption band centered around 3367 cm^{-1} and the bending mode at 1642 cm^{-1}. Water plays the dual role of reactant as well as a medium of solvent in this enzymatic reaction. Time-stamped fluorescence spectra between 500 to 596 nm were sequentially collected one after another ($Tcycle \approx 30\ s$) under excitation with 485 nm light until the reaction was finished (Figure 4.1 a). The vacuum Rabi splitting of the ON-resonance cavity is 703 cm^{-1}; about 21% of the bare transition energy, representing the system, is under ultra-strong coupling. Based on the product concentration time traces, the initial rate of product formation was determined for each cavity (OFF-ON resonance) by the initial slope of each time trace with linear regression shown in figure 4.1 b. An approximately 4.5-fold decrease in the second-order rate constant (k_{cat}/K_M) was observed when coupling the O−H stretching vibration, whereas no effect was detected for the strong coupling of the bending vibration of water. Overall, the tuning experiment response to the strong coupling of the O-H stretching band on the proteolytic activity of pepsin (Figure 4.1 c). The modification of an enzymatic hydrolysis reaction under a strong coupling of the water vibrations presents an entirely novel method for biological molecules.

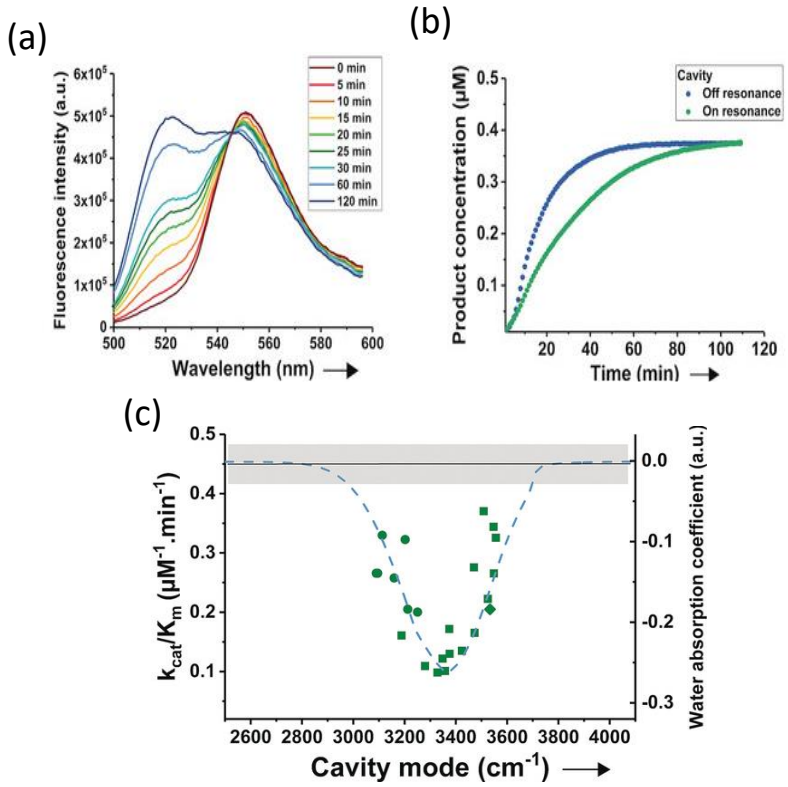

Figure 4. 1. Pepsin enzymatic activity under VSC of the water stretching mode. (a) Emission spectra between $500-596\ nm$ were collected under excitation with $485\ nm$ light for the pepsin hydrolytic activity towards substrate in a Fabry–Perot cavity; (b) kinetic traces for on- and off-resonance to the water stretching vibration; (c) Detuning plot for $6th$ order mode, $7th$ order mode and $10th$ order mode coupled. Blue dashed curve: water absorption coefficient. Black line: average measured initial reaction velocity of reactions measured in a non-cavity. (Vergauwe et al. 2019)

4. 2 Selection of Enzyme: α −Chymotrypsin

α −Chymotrpsin ($\alpha - CT$) is a digestive enzyme with a molecular weight of 24800 Da. It is a catalyst used for the cleavage of peptide bonds and amide bonds. Furthermore, it catalysis the hydrolysis of all derivatives of esters. $\alpha - CT$ catalyzed hydrolyses of specific ester and amide substrates indicated more than one pH dependency. However, in the general case, it provides a change in the rate-determining step upon varying the pH conditions. It is shown that the kinetics of the hydrolysis of PNPA catalyzed by $\alpha - CT$ can be fully described by a mechanism involving three distinct steps. The first step, which involves the rapid adsorption of the substrate on the enzyme- is too fast to be measured. The second step is the acylation of the enzyme and the liberation of p- nitrophenol. The third step involves the release of acetate and reactivation of the enzyme (Scheme 4.2). It was observed that $\alpha - CT$ catalyzes the hydrolysis

of PNPA, giving a considerable effort to study the kinetics of the reaction.[115–118] Here, the kinetic studies of the product formed can be characterized using spectrophotometric methods. Like other enzyme catalysts, $\alpha - CT$ hold higher regio- and stereoselectivity toward enzyme-substrate complex. $\alpha - CT$ is a β −protein which resembles a random coil conformation, as characterized by circular dichroism (CD) studies.[119,120] The crystal structure consists of antiparallel pleated sheets that are highly distorted and form short irregular strands. The stability of the enzyme was studied by different concentrations of the organic solvents (ethanol, 1,4-dioxane and acetonitrile), and CD measurements observed the characteristic change in the secondary structure.[121] Even at a higher concentration of organic solvents, the enzyme catalytic activity and stability are maintained.

Enzymes are highly complex and extremely sensitive that undergo reversible or irreversible conformation changes under external stress. It is recognized that enzymes are biological systems and are active in their native conformation. Therefore, the solvent that can stabilize the structure or enhance the activity is highly desirable. Buffer medium has a significant role in maintaining the native conformation of the enzyme and hence protects its activity in a range of pH. UV-Visible spectra of $\alpha - CT$ in aqueous solution exhibit two absorption peaks at $200 - 220\ nm$ and $260 - 300\ nm$, respectively, as shown in figure 4.2. The first peak in the lower wavelength reflects $\pi \rightarrow \pi^*$ transition, and it is the backbone framework of the protein. This peak shifts towards a higher wavelength and is less intense as the concentration of buffer increases. It is probably an increase in the polarity of the solvent and an increase in the buffer concentration that induced the shielding of the peptide group from the aqueous environment. The second peak shows $n \rightarrow \pi^*$ transition corresponds to the aromatic amino acids.

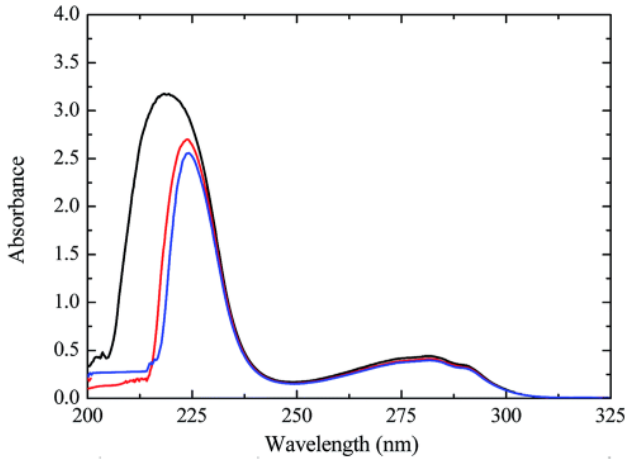

Figure 4. 2. UV-Visible spectra of $\alpha - CT$ in TRIS buffer at different concentrations 0.05 M (black line), 0.5 M (red line), 0.1 M (blue line) at pH 8.0 and temperature 25℃.

$\alpha - CT$ is a monomeric enzyme that exhibits no allosteric effects. It is a member of serine proteases because of their common catalytic mechanism in which serine is the reactive part for enzyme activity. The three catalytically critical residues of $\alpha - CT$ form a hydrogen-bonded circuit called a catalytic triad. This triad is made from residues: His-57, Ser-195, and Asp-102 is hydrogen bonded with each other and is common in all serine protease active sites.[114] The hydrophobic binding pocket surface is not inert or non-polar but contains sufficient polarity to provide weak polar interactions with the solvent. The catalytic effect is also explained by low barrier hydrogen bonding (LBHB), which allows the hydrogen to be equally shared between the closely matched pK_a (gaseous phase).[113] Frey et al. (2000) showed the participation of LBHB in the mechanism of $\alpha - CT$ and introduced the role of Asp-102 and His-57 in catalysis.[114] It suggests that in the TS, LBHB increases the basicity of His-57, thereby facilitating the abstraction of a proton from the Ser-195. This process stabilizes the tetrahedral intermediate in the acylation step. These results were characterized by NMR spectroscopy in which deuterium isotope effects shifted to 17 ppm from 18 ppm with a broad downfield signal for the proton bridging of His-57 and Ser-195.[122] However, Warshel et al. disagree with the LBHR because, for a polar liquid, the hydrogen bond will be polarized to attain large solvation energy, making the LBHB unfavorable.

$\alpha - CT$ catalyzes the hydrolysis of esters was studied in the $1960s$, and the observed hydrolysis of acyl-enzyme is the rate-determining step.[123,124] It has one "active site" per molecule, and the saturation phenomenon catalyzes the reactions. A plot of reaction rate versus substrate concentration is shown in figure 4.6. Linear behavior is observed at low concentration, but at high concentration, the rate becomes independent of the substrate concentration.[125] There must be a requirement that enzymes bind with the substrate before the catalytic reaction occurs.

$$E + S \underset{}{\overset{K_M}{\rightleftharpoons}} ES \xrightarrow{k_2} E + P$$

Scheme 4. 2. Stepwise mechanism of $\alpha - CT$ involving three distinct steps.

It can be defined by E as the enzyme ($\alpha - CT$), and S is the substrate, K_M is the dissociation constant of binding and k_2 is the catalytic rate constant. When the initial concentration of the substrate is much greater than the enzyme concentration, the initial reaction rate (v_0) is defined by the equation 4.1:

$$v_0 = \frac{k_2[E]_0[S]_0}{[S]_0 + K_M} \quad [4.1]$$

Eqn. 4.1 is known as Michaelis-Menten kinetics and $v_{max} = k_2[E]_0$ is representing the maximum rate when an enzyme E exists entirely in the form of ES. The equation becomes linear by taking the reciprocal of that can be written as:

$$\frac{1}{v_0} = \frac{1}{k_2[E]_0} + \frac{K_M}{k_2[E]_0[S]_0} \quad [4.2]$$

Equation 4.2 is described by the Lineweaver-Burk plot. Plotting $1/v_0$ Vs. $1/[S]_0$, the ordinate intercept is $1/k_2[E]_0$ and the slope of the straight line is $K_M/k_2[E]_0$, thus evaluating the value of K_M. The slope is increased in the presence of competitive inhibition, but the intercept does not change. In the case of non-competitive inhibition, the intercept also rises. It measures the value of k_2/K_M known as the catalytic efficiency of an enzyme. k_2 it is the turnover number, which describes how many substrate molecules are transformed into products per unit of time. The K_M value gives us a description of the substrate's affinity to the enzyme's active site. Putting these two together to obtain the ratio allows a way to test the enzyme's effectiveness on that particular substrate. The greater the ratio, the higher the rate of catalysis is; conversely, the lower the ratio, the slower the catalysis. A comparison of specificity constants can also be used to measure an enzyme's preference for different substrates (i.e., substrate specificity). The higher the specificity constant, the more the enzyme "prefers" that substrate. However, a complete analysis requires to evaluate of potential inhibition events, allosteric effects, binding effects, and time-dependent inhibition.[112]

4. 3 Type of inhibition

In competitive inhibition, an inhibitor resembles the substrate that binds to the active site and prevents the substrate from further binding. The substrate and inhibitor compete for the same active site. It raises the apparent value of K_M for its substrate with no change in the v_{max} value. It can be overcome by adding more substrate to increase the chance of the enzyme-substrate binding process. A competitive inhibitor can be reversible or irreversible and bind with the allosteric site in the enzyme. A non-competitive inhibitor binds equally to both free enzyme and enzyme-substrate complex simultaneously. However, the substrate-enzyme-inhibitor complex cannot form the product; it can only back convert into an enzyme-substrate or

enzyme-inhibitor complex. It differs from a competitive inhibition- the binding of the inhibitor does not prevent the binding of the substrate and *vice-versa*. The inhibitor binds with the enzyme's allosteric site and prevents the reaction from occurring. This type of inhibitor changes the binding affinity of the catalyst for the substrate and reduces the rate of the chemical reaction. In terms of the Lineweaver-Burk plot; a non-competitive inhibitor reduced the v_{max} and K_M remain unchanged. Another kind of inhibitor formed after forming an enzyme-substrate complex is known as an uncompetitive inhibitor. It cannot be reversed by increasing the concentration of the substrate. The Lineweaver-Burk plot shows parallel lines rather than intersecting at any point. The formation of complex enzyme-substrate-inhibitor reduces the v_{max} maximum enzyme activity since it takes a longer time to convert into the product and also decreases the value of K_M.

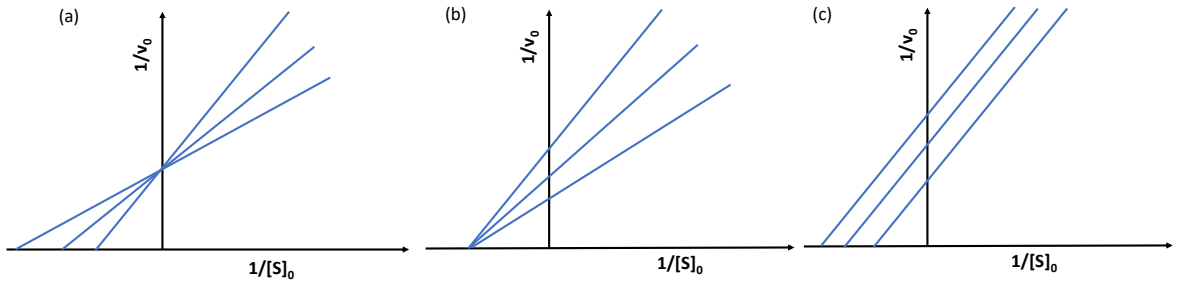

Figure 4.3. Modes of inhibition (a) Competitive inhibition; (b) Non-competitive inhibition; (c) Uncompetitive inhibition.

4.4 Experiment methods to study the kinetic parameter of $\alpha - CT$ under VSC:

4.4.1 Solution preparation

PNPA and $\alpha - CT$ from bovine pancreas type-II were used for the hydrolysis studies of macromolecule in FP-cavity. All the chemicals, including tris(hydroxymethyl)aminomethane (TRIS), polymethyl methacrylate (PMMA), dimethoxy ethane (DME), toluene, and deuterium oxide (D_2O) were purchased from Sigma-Aldrich.

The rate of hydrolysis of PNPA by $\alpha - CT$ has been determined by measuring the appearance of *p*-nitro phenoxide ion (PNP-) at 400 nm. 0.1 M stock solution of PNPA prepared in DME. The substrate concentration was 100 times higher than the enzyme concentration, following first-order kinetics. There is always a considerable substrate concentration range for the

enzymatic reactions; otherwise, another mechanism starts to play a role. At higher concentrations, the reaction rate can be considered substrate-independent. At the same time, enzyme $\alpha - CT$ was prepared in the aqueous solution of biological buffer TRIS at pH 8.6 and temperature 25℃. An increase in buffer concentration increases the activity of an enzyme.[126] We optimized the TRIS concentration of 0.05 M, and to maintain the pH, we mixed the equal ratio of TRIS-acid and TRIS-base. 110 mg of TRIS-acid and 218 mg dissolved separately in 50 ml of distilled water, stored at 8℃, and further used as a stock solution to prepare the enzyme solution. Mixing of TRIS-acid and TRIS-base in 1:1 resulted in a 0.05 M concentration of the final buffer solution. $\alpha - CT$ −12.5 g dissolved in 10 ml of TRIS buffer solution and kept overnight before starting the reaction. The final concentration of $\alpha - CT$ was $E_0 = 5 \times 10^{-5} M$; the same E_0 is for all the set of experiments. Enzyme activity normally get affected by aging, so we normally make sure collect one set of cavity and non-cavity data on the same day for precise comparison. Before starting the experiment, PNPA and $\alpha - CT$ were kept in the water bath for 30 $minutes$ to stabilize the solution temperature. Experiments were carried out by varying the PNPA concentration and keeping the constant value of E_0, pH, and temperature.

All the kinetic experiments were performed in the pathlength of 25 μm demountable microfluidic flow cell. BaF_2 windows are dip-coated with 2 % PMMA (2g of PMMA in 98 g toluene) solution to avoid any enzyme inhibition from the surface of the windows. If the BaF_2 windows are not coated with PMMA, there shall be a complete deviation for the enzyme first-order kinetic rates. After that, BaF_2 passivates with the dilute solution of enzyme 10^{-7} M solution and washed with distilled water $2-3$ $times$ before each measurement. PMMA coating and passivation are done on cavity and non-cavity conditions, allowing us to compare the reaction rate properly.

4.4.2 Cavity preparation and reaction study

Here, the idea is to couple the O-H_{str} band of water that overlap with the O-H_{str} and N-H_{str} band of amide A of $\alpha - CT$ at 3325 cm^{-1}. At the same time, the O-H_v bending band of water overlap with the amide I of $\alpha - CT$ at 1637 cm^{-1}. The coupling strength achieved is approximately 700 cm^{-1} by cooperative coupling of water and enzyme molecules. We could achieve this by using a spacer of 6 μm that gave an empty cavity FSR of ~630 cm^{-1}. Coupling of the 7th mode

of the 6 μm cavity with the O-H_{str} band of water molecules and taking into account the refractive index of the medium – vibro polaritonic states are formed with $VP+$ and $VP-$ at 3720 cm^{-1} and 3003 cm^{-1}, respectively as shown in figure 4.4.

However, all the kinetic experiment was performed using 25 μm mylar spacer so that the signal of PNP- is readily detectable at 400 nm; this also avoids the interference issues related to the cavity structure. Substrate concentration is also optimized within a range of 0.2 to 2 mM; beyond that, the reaction rate is not accessible for standard kinetic measurements. It is also seen that cavity modes are highly dissipative near the absorption region of the PNP- ions. The strong absorption band of O-H_{str} shows an FWHM of 410 cm^{-1} that can couple to more than two FP-cavity modes. Further, the empty cavity FSR is 204 cm^{-1} having $22nd\ and\ 23rd$ modes coupled simultaneously to the O-H_{str} band (Figure 4.4). At the same time, $11th$ mode is also coupled to the O-H_v bending band of water molecules. Here, we achieved a cooperative

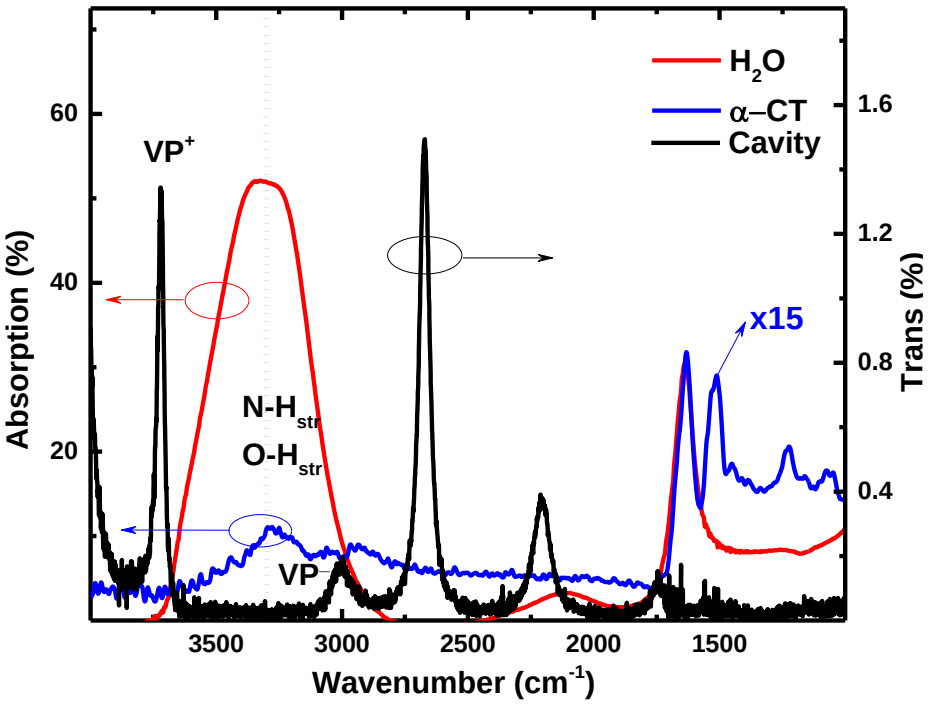

Figure 4. 4. ATR absorption spectra (red and blue arrow) of water (O-H_{str}; red trace), $\alpha - CT$ (blue trace) , and transmission spectrum corresponds to black arrow shows the formation of $VP+$ and $VP-$ with mylar spacer 6 μm coupling of 7th mode of the cavity (black trace) with O-H_{str} bond.

VSC condition between the solute and solvent molecules by forming vibro-polaritonic states. Detuning the cavity is difficult because of using the large thickness spacer and inhomogeneous broad-spectrum range of the O-H_{str} band of water molecules.

In chymotrypsin, the triad consists of Ser 195, His 57, and Asp 102. Spectroscopic evidence indicates that a strong hydrogen bond (a low-barrier hydrogen bond or LBHB) links His 57 and Asp 102in the protonated state of the catalytic triad. The formation of LBHB between His 57 and Asp 102 in the course of catalysis should increase the reactivity of His 57 as a general base. This proposes a new mechanism in which the formation of this LBHB facilitates nucleophilic attack by the -OH group of Ser 195 on the acyl carbonyl group of substrates. C=O of PNPA is to be close to the OH group of Ser 195, with His 57 fixed in the right position to abstract the OH proton. The Asp 102 residue is to hold the imidazole ring of His 57 in position through hydrogen bonding so that the substrate (PNPA) is constrained to react with Ser 195 and cannot acylate the more reactive His 57.[114] Two concerted proton transfers are postulated to take place in the transition state to form the tetrahedral addition intermediate. NMR data on the carbon-bonded protons of the catalytic histidine in chymotrypsin supported the conventional general acylation mechanism. These conclusions are supported by the chemical shift of this proton, the deuterium isotope effect on the chemical shift, and the properties of hydrogen-bonded model compounds in solvents.[122] The enzyme consists of nearly 250 amino acid residues with some 400 exchangeable sites, that make the system more exposed to the surroundings.

The reaction follows the charge relay mechanism in which the activated Ser-195 attack on the electron-deficient carbonyl carbon of PNPA forms an enzyme-PNPA complex (Scheme 4.3). The release of PNP- ions, and then detects using UV-VIS spectroscopy. The reaction was initiated by fixing the mixing of $\alpha - CT$ in the volume of 1000 μl from the stock solution of $5 \times 10^{-5} M$ and varying the PNPA volume from $2 - 10\ \mu l$ from the stock solution of 0.1 M. Mixing both systems has a negligible effect on the enzyme concentration (E_0). This procedure allowed us to get PNPA concentration in the range of $0.4 - 2.0\ mM$ and the system is in the pre-steady condition ($E_0 \ll S_0$). The non-linear absorption due to FP-cavity was ruled out by plotting Beer's law and calculating the absorption coefficient of PNP- ions for cavity and non-cavity. A_{inf} values for the different concentrations of PNPA indicate the complete reaction conversion into PNP- ions and give absorption coefficient (ϵ_{nc}) in non-cavity was $1.7 \times 10^4\ mol^{-1} L\ cm^{-1}$. Under VSC, Beer's law is followed as obtained in the linear fitting and extracts the ε_c was $1.6 \times 10^4\ mol^{-1} L\ cm^{-1}$(Figure 4.5). These values match with the literature absorption coefficient of PNP- ions.[116]

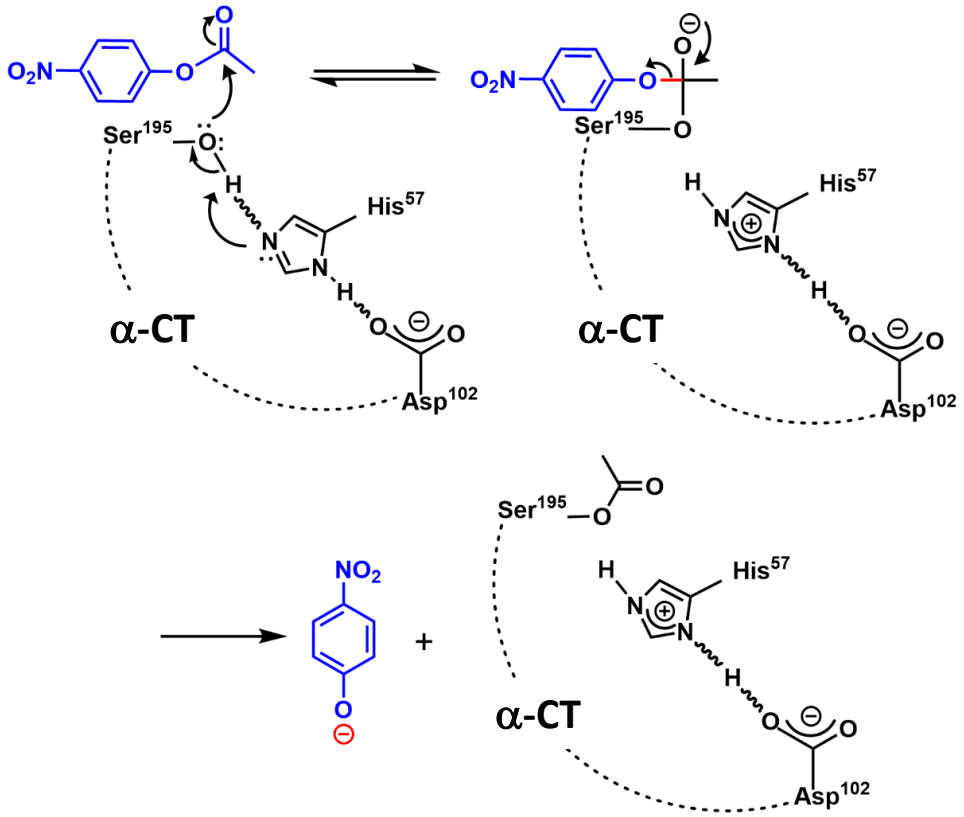

Scheme 4. 3. Charge-Relay mechanism for ester hydrolysis of PNPA using $\alpha - CT$.

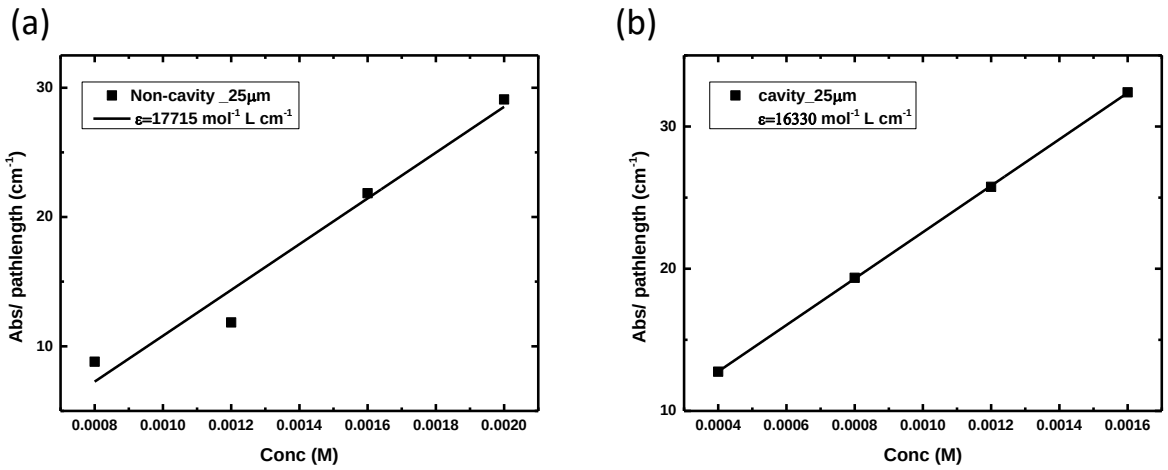

Figure 4. 5. Beer law plot- follow linear relation in the (a) non-cavity (b) cavity; by varying the PNPA concentration $0.4 - 2.0\,mM$ and keeping enzyme concentration fixed $E_0 = 5 \times 10^{-5} M$ for a pathlength of 25 μm.

4. 5 Result and Discussion

Michaelis-Menten equation (Eqn. 4.1) was used to understand the substrate and enzyme interaction's nature and extract the turnover number (TON) and catalytic efficiency. Under

steady-state approximation, v_0 is proportional to S_0 and the non-cavity experiments are recorded between 0.4 to 2.0 mM concentration range. Experimentally obtained apparent rate versus substrate concentration is given in figure 4.6:

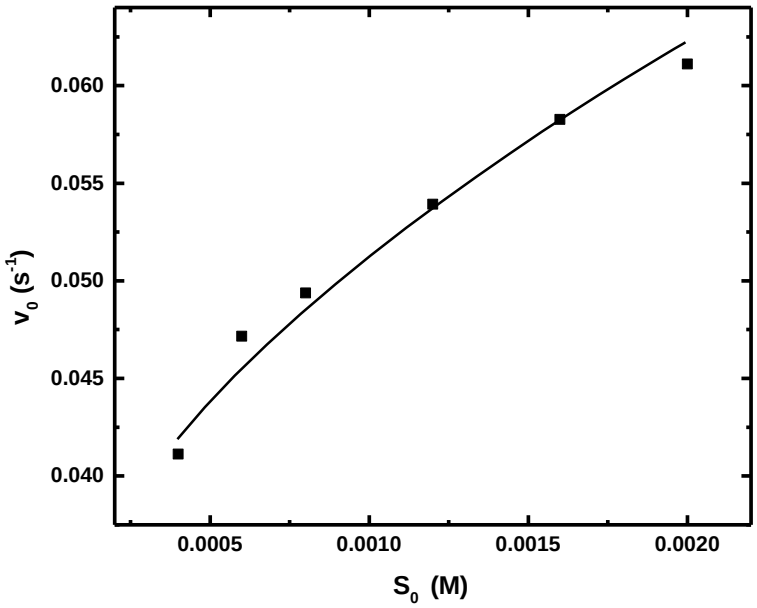

Figure 4.6. Michaelis-Menten plot for non-cavity keeping fixed concentration of enzyme $5 \times 10^{-5} M$ and varying the substrate concentration $0.4 - 2.0\ mM$.

Cavity experiments were carried out with Au mirrors on BaF_2 windows in the same pathlength of the spacer. Initially, the reaction rate was studied for one of the low concentrations of substrate $[S]_0 = 0.5\ mM$ and kept the enzyme concentration constant. It was found that the initial rate boosts up to 3 $times$ by tuning the cavity mode at 3386 cm^{-1} shown in figure 4.7. Here, UV-Vis spectrophotometer is used for the calculation of FSR. The control experiment changed one of the mirrors with the bare substrate known as half-cavity. This experiment proved the effect of VSC and ruled out any other weak interactions that are likely to happen due to the presence of Au mirrors. For example, the Au mirror can provide a near field and evanescent field close to the mirror vicinity, which may affect the reaction process. However, half-cavity experiments did not show any rate enhancement, suggesting that the requirement of FP cavity mode is one of the necessary criteria for VSC, thereby affecting the reactivity of the enzyme molecules. Inhomogeneously broad O-H_{str} won't allow us to do a tuning experiment. It is seen that initial kinetic traces for the half-cavity and non-cavity have negligible change (Figure 4.9). Please also note that all the experiments had been done with the same procedure of passivating with PMMA, dilute enzyme solution, and washing with distilled water. The above experiments confirm that the rate is not affected by half-cavity, and

the reaction was only controlled by resonance coupling of the cavity mode (Figure 4.9). In the next step, we optimized the same experiment in the cavity by varying the substrate concentration from $[S]_0 = 0.4 - 2.0\,mM$. It has been clearly observed from the reaction rate as the concentration increases, the system follows zero-order kinetics.

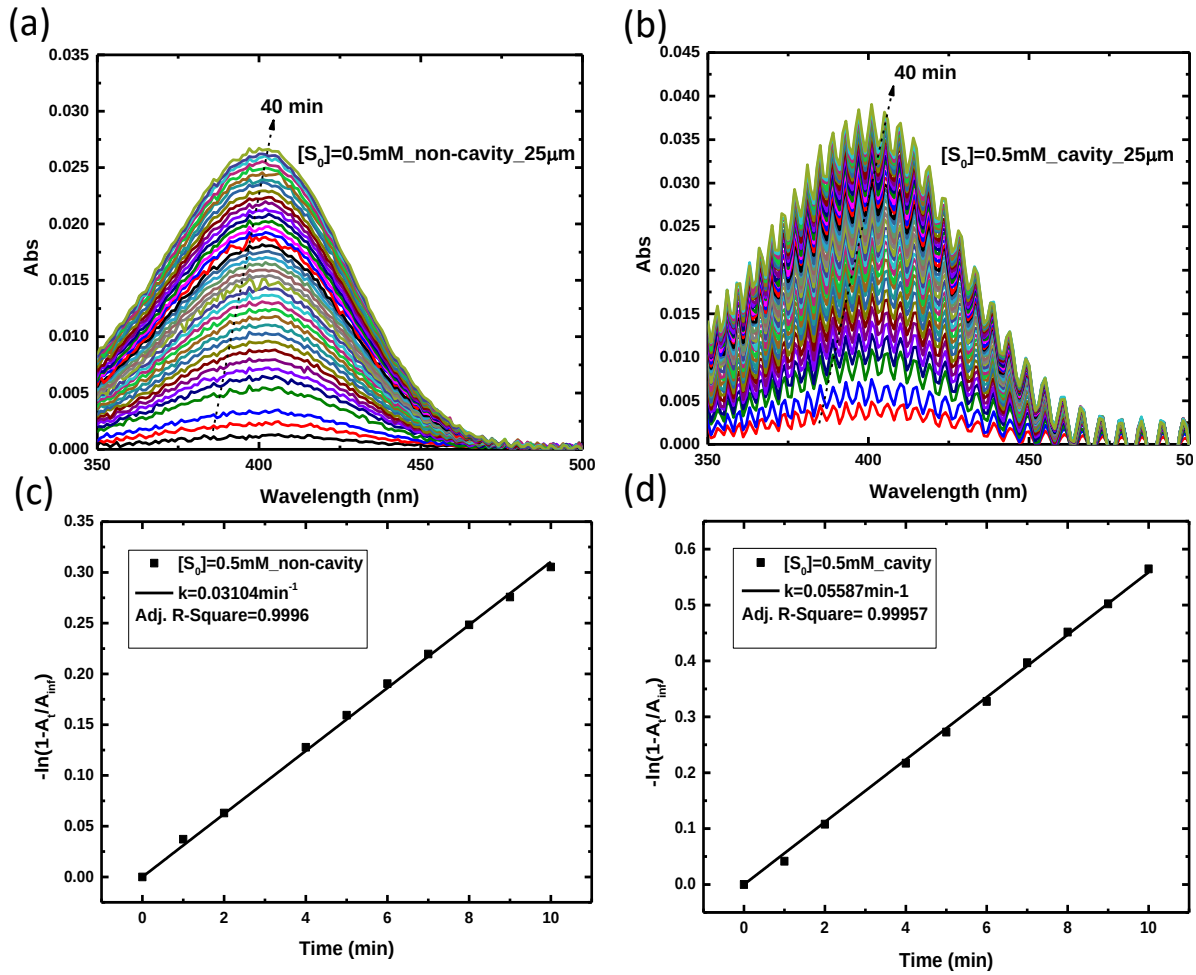

Figure 4.7. Temporal evolution of PNP- ions during the hydrolysis with $\alpha - CT$ $(5 \times 10^{-5} M)$ with PNPA $0.5\,mM$ for (a,b) non-cavity and cavity with $25\,\mu m$, (c,d) are the corresponding rate plot.

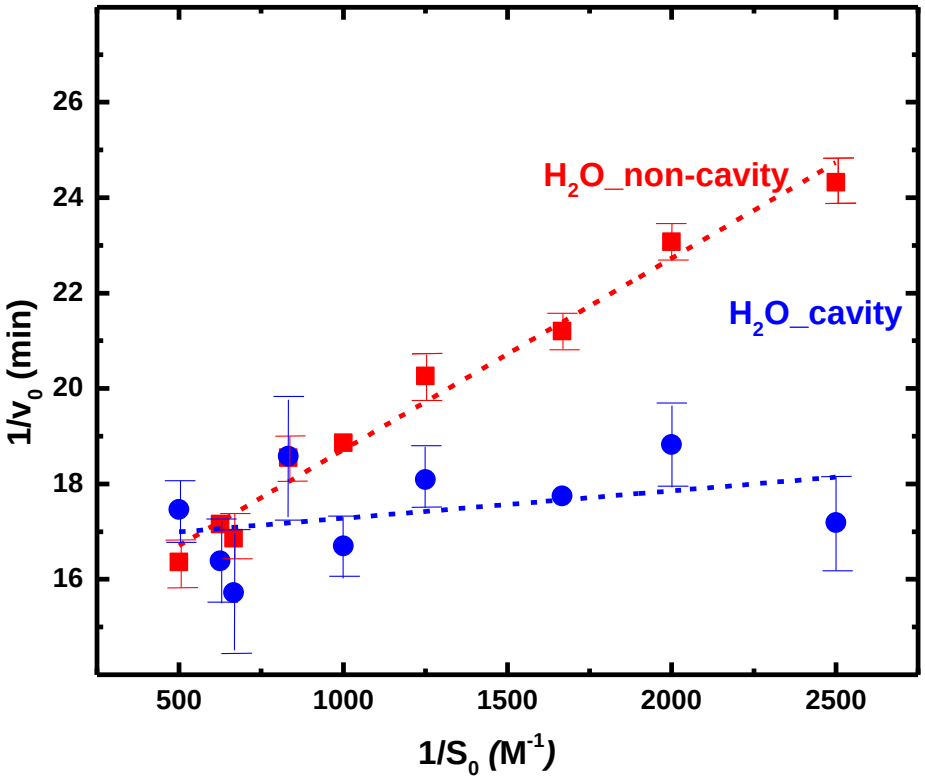

Figure 4.8. Lineweaver-Burk plot for the hydrolysis of PNPA $(0.4 - 2.0\ mM)$ using $\alpha - CT$ $(5 \times 10^{-5} M)$, non-cavity (red trace), and cavity (blue trace).

Table 4.1. Hydrolysis of PNPA by $\alpha - CT$ $(5 \times 10^{-5} M)$ keeping $pH = 8.5$ and $T = 22$°C.

Solvent	S_0(mM)	TON (min^{-1})	k_{cat}($M^{-1}min^{-1}$)
H_2O (Non-cavity)	0.4-2.0	0.068±0.001	248.75± 13.68
H_2O (cavity)	0.4-2.0	0.059± 0.002	1740.03±1564.11
D_2O (Non-cavity)	0.4-1.6	0.051± 0.003	240.96± 56.62
D_2O (cavity)	0.4-1.6	0.050± 0.003	273.97± 48.31

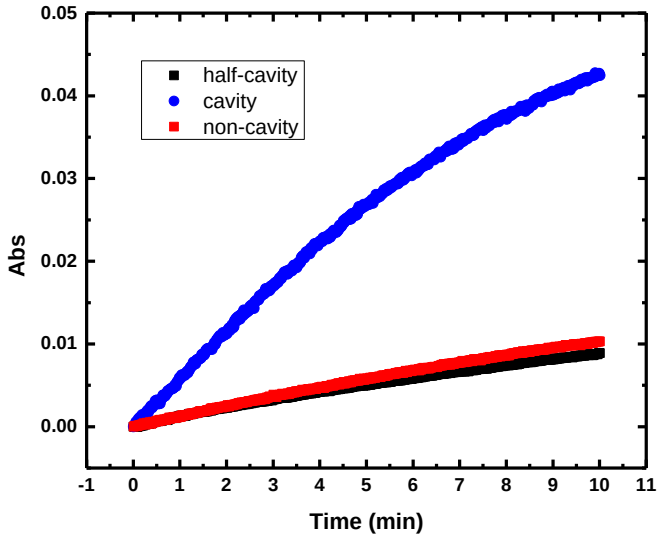

Figure 4.9. Comparison of half-cavity (black trace), ON-resonance (blue trace), and non-cavity (red trace) with a PNPA concentration of 0.4 mM.

Analysis of the Lineweaver-Burk plot for non-cavity and cavity gives a straight line, as shown in figure 4.8. Plotting of $1/v_0$ Vs. $1/[S]_0$, help us to calculate the TON of 0.068 and 0.060 min^{-1} for the cavity and non-cavity, respectively. At the same time, catalytic efficiency (k_{cat}) increased by $\sim 7\ times$ (changes from 1740 to 249 $M^{-1}min^{-1}$) for the cavity to non-cavity (Figure 4.8). In the case of a cavity, we cannot reach the same resonance condition, so the given data is the average of 3 sets of experiments. The change in catalytic efficiency without affecting the TON is interpreted as competitive catalysis under VSC conditions. It is reported in the literature that hydrogen bonding plays a vital role in the charge-relay mechanism, where water has a significant impact on controlling the TS of the activated complex.[127] The isotopic change of the buffer solvent from H_2O to D_2O was investigated to understand the effect of VSC on the mechanism of the enzyme-substrate complex. Now, the enzyme prepared in the deuterated solvent having the same concentration [$5 \times 10^{-5} M$]. The coupling of O-D_{str} band of D_2O with the 15-17th mode of the cavity gave the coupling strength of 522 cm^{-1} shown in figure 4.10. Initially, for the lowest concentration of the substrate, 0.4 mM was used to study the reaction kinetics, and for this condition, the reaction rate decreased by a factor of 1.3 $times$ in non-cavity compared to H_2O solvent system. Very interestingly, the cavity did not show any change in the reaction rate by coupling the O-D_{str} band of D_2O at 2550 cm^{-1}. In the non-cavity and cavity experiment, D_2O decreases the TON by 1.3 $times$ as compared to H_2O, as represented in figure 4.13.

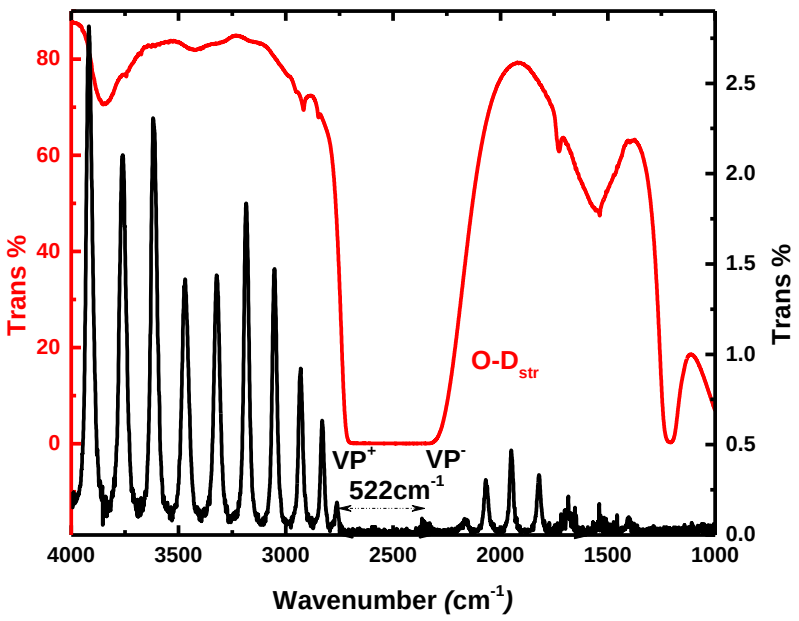

Figure 4.10. FT-IR spectra of D_2O in red traces and FP cavity mode splitting into $VP+$ $and\ VP-$ in black traces with 25 μm spacer.

The literature reported that the primary kinetic isotopic effect changes the reaction rate by 2.4 $times$.[124] The secondary effect comes into play due to the solvent also, and that gives rise to a change in the kinetic rate by a factor up to $1-1.5\ times$. We observed that changing H_2O to D_2O does not affect the charge relay mechanism or proton-transfer event. Evidence for this mechanism includes the downfield chemical shift of the proton bridging His 57 and Asp 102 in the transition state. Deuterium isotope effects in this range are characteristic of LBHBs, and this observation provides further support for the assignment of the proton bridging His 57 and Asp 102 in transition-state analog complexes as an LBHB.

To understand the role of isotope exchange in $\alpha-CT$, high-resolution mass spectroscopy (HRMS) has been done in different solvents (H_2O and D_2O). $\alpha-CT$ $(1\ nM)$ was injected into the mass spectrometer. Data were acquired in the ESI (negative biased) mode and plotted according to the m/z ratio of the molecular fragments formed during the ionization of the enzyme. We follow a simple analogy to compare the molecular mass of the fragments formed from H_2O and D_2O: Actual peak position of one of the unknown enzyme fragments (in H_2O): m/z = 2537.22 $(M)^+$ (Figure 4.11). Its secondary peak: m/z = 2539.22 $(M+2H)^{2+}$: The difference between the primary and secondary peak is 2. i.e., the effective charge z= 2 (Please note that $[M]^+$ to $[M+2H]^{2+}$ gives z=2; $[M]^+$ to $[M+3H]^{3+}$ gives z=3; $[M]^+$ to $[M+4H]^{4+}$ gives z=4 etc.); that implies the above fragment give a molecular weight of 2537.22/2 = 1268.61 for the enzyme in H_2O. Similarly, the enzyme in D_2O gives a molecular weight of 1268.85 atomic

units. i.e., the difference in molecular weight for this particular fragment is 1268.85 - 1268.61 = 0.24. We know that the actual molecular weight is 25 kDa. Extrapolating the molecular fragment weight to 25 kDa (20 x 0.24) gives a difference of roughly 5 atomic units (Figure 4.11).

These are the rough estimate of the relative molecular mass variation from H_2O to D_2O. Absolute mass calculation and identifying the fragments is a tedious process that requires proper sequencing and molecular simulation-based fragmental analysis. It is beyond the scope of the work. HRMS studies indicate that the isotope exchange is very slow as observed in the aging studies of $\alpha - CT$ in D_2O. At the same time, we took the CD for $\alpha - CT$ in both the solvents H_2O and D_2O (Figure 4.12). The experiment was to utilize far-UV CD measurements to study the changes in the secondary structures of $\alpha - CT$. We found no significant change or alternation in the spectrum for $\alpha - CT$ in both the solvents and the stability remains the same. The characteristic β −conformation of the $\alpha - CT$ do not change with the isotopic solvents.

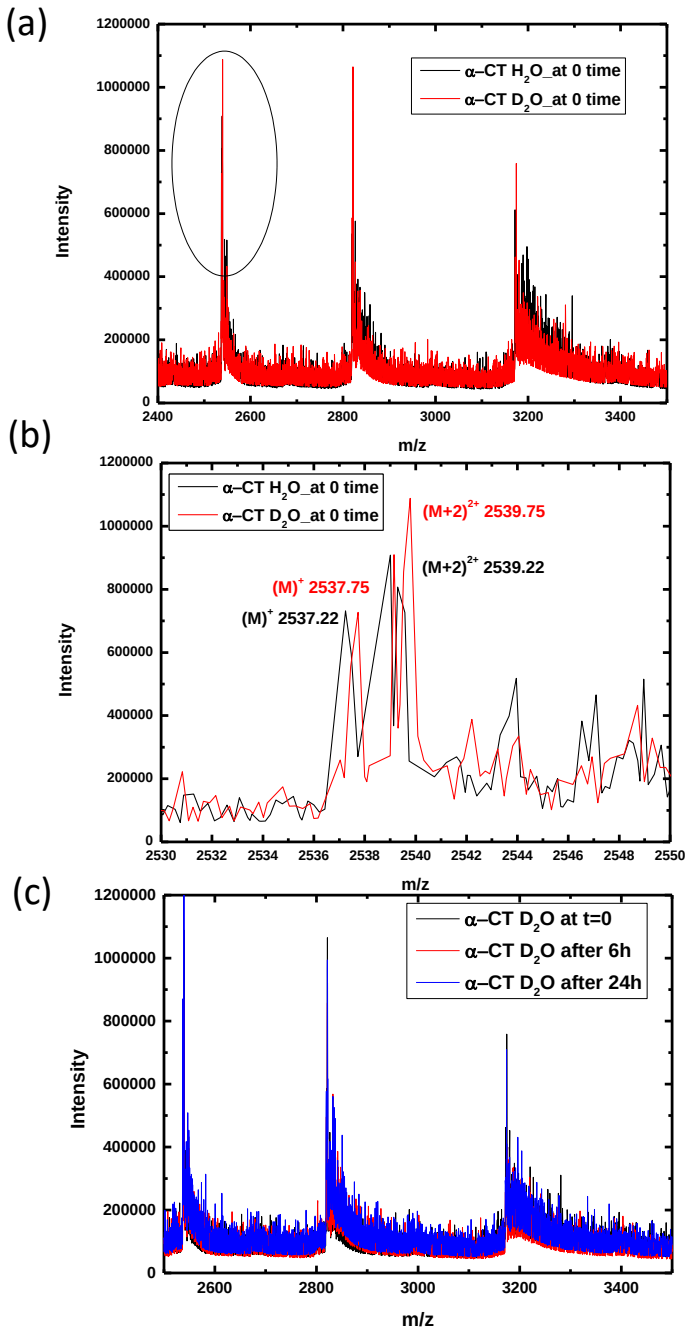

Figure 4.11. (a) High-resolution mass spectra of $\alpha - CT$ in H_2O (black trace), D_2O (red trace) at zero time; (b) is the corresponding zoomed spectra indicating the fractional change in the m/z value, and (c) Aging experiment of $\alpha - CT$ in D_2O.

To get a clear picture of the VSC of water molecules, we looked into the dispersion behavior of polaritonic states formed from the coupling of the O-H_{str} band. For clear evidence, we used $6\ \mu m$ pathlength of the cavity and injected water (H_2O) into it. The setup was placed on a goniometer and calibrated to normal incidence using a red laser, the FTIR's reference line. The angle of incidence changes from $0\ to\ 8$ degrees with slow graduation of an angle of 2^0

variation (figure 4.14 a). Experimental results clearly show the dispersive behavior of the vibro-polaritonic states. Transfer matrix simulations produce the same features and show the Rabi splitting energy of $\sim 700\ cm^{-1}$ (figure 4.14 b).

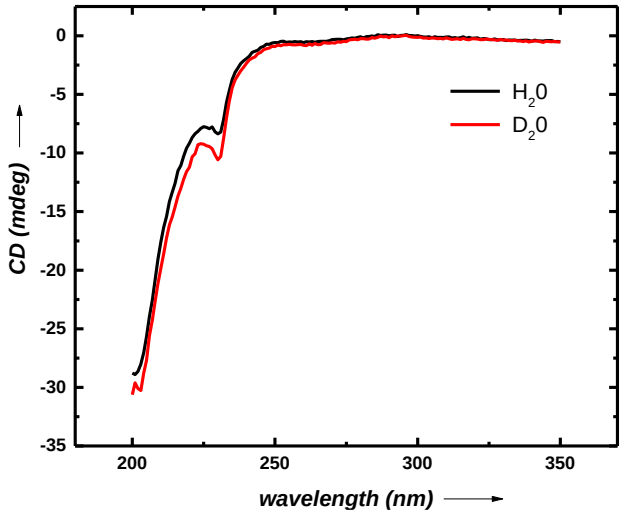

Figure 4. 12. Circular dichroism spectra of α-CT in a buffer solution of H_2O (black trace), D_2O (red trace).

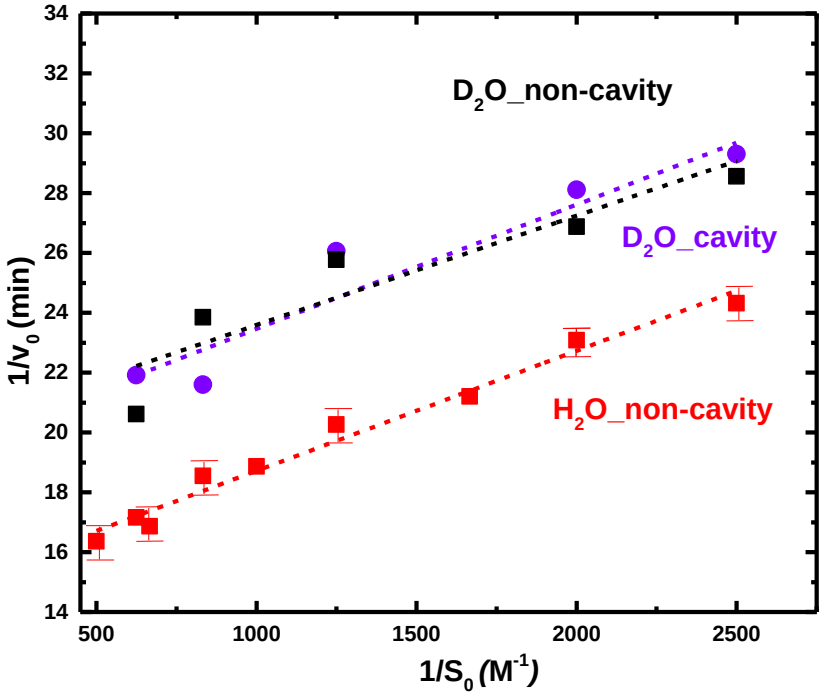

Figure 4. 13. Lineweaver-Burk plot for the hydrolysis of PNPA in D_2O for the non-cavity (black squares) and a cavity (violet circles) by coupling to the O-D_{str} band and its comparison with the O-H_{str} band of water coupling.

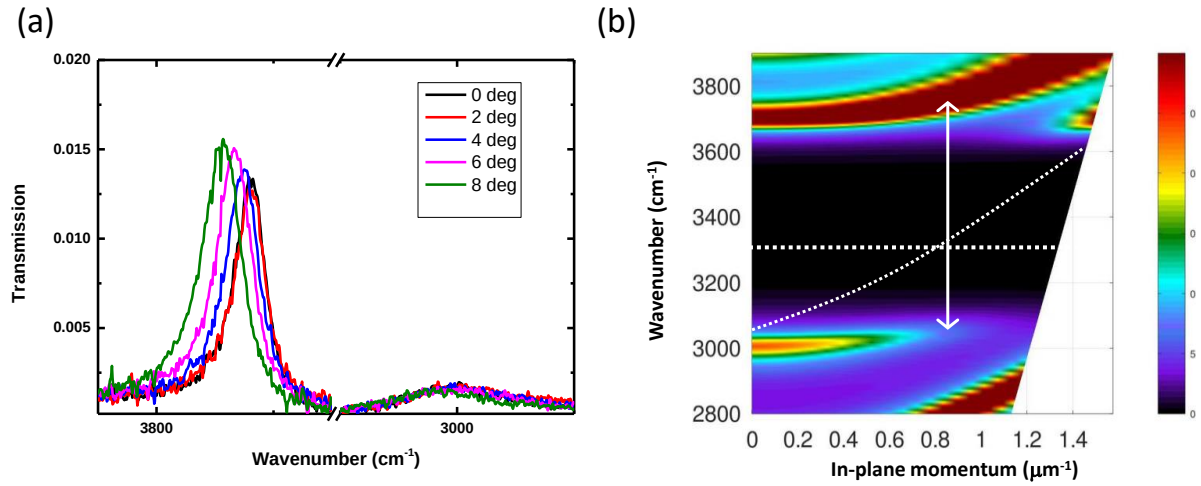

Figure 4. 14. (a) Experimental cavity dispersion of vibro-polaritonic states formed by coupling O-H_{str} mode of water molecules in 6 μm spacer; (b) Dispersive curve of Vibro-polaritonic states by using TMM simulation.

As mentioned in the previous chapters, coupling strength is directly proportional to the square root of the number of oscillators involved. We tested this effect by studying the reaction rate by varying the coupling strength of the medium. The apparent rate increases as one moves from D_2O to H_2O water molecules. It also indicates that the solvent has a role (secondary kinetic isotopic effect) that doesn't affect the enzyme reaction mechanism but may be involved through the solvation shell of the enzyme molecules.[113,128] Please note that we only varied the solvent concentration of H_2O by mixing it with D_2O and the substrate and enzyme were kept intact for a better comparison. Under VSC condition (ON-resonance at 3386 cm^{-1}) the apparent rate changes non-linearly, as shown in figure 4.15.

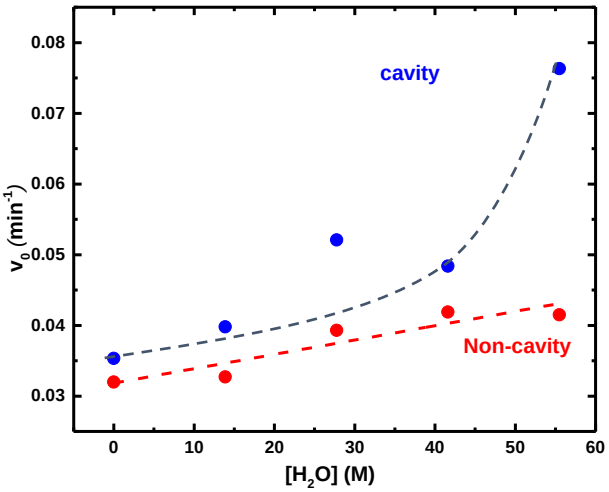

Figure 4. 15. The enzymatic reaction with a fixed concentration of PNPA ($0.4\,mM$) and $\alpha - CT$ ($5 \times 10^{-5} M$) by changing the concentration of H_2O: D_2O molecules in the non-cavity (red dot) and cavity (blue dot). (Dotted lines are guides to the eye)

Similar non-linear behavior is reported in other polaritonic chemistry experiments, and this effect's origin is still unknown to us. However, we believe that the self-interaction of the dipole is dominant once the system enters into ultra-strong coupling conditions, which may drive a quadratic behavior in the rate enhancement. A similar observation was observed spectroscopically in similar coupling conditions.

4. 6 Conclusion

VSC shows a change in the rate of a reaction in enzymatic reaction by selective coupling of water molecules. Ser-195 is the active binding site having O-$H_{str,}$ which is strongly coupled, forming active catalytic triad formation. This finding of cooperative coupling of water and enzyme molecules can improve catalytic efficiency. The same technique can also be used to elucidate the complex enzymatic reaction mechanism as we did in understanding the relay mechanism and its effect on H-bonding. Here, the VSC of O-H_{str} either controls the charge relay mechanism, thereby boosting the proton transfer process. The O-D_{str} gives the comparable splitting energy, whereas its influence on reaction rate is negligible under strong coupling due to poor overlap of the vibrational envelope of the enzyme and the solvent system. These experiments show the versatility of the selective bond coupling and cooperative VSC to control and study the chemical and physical properties at the molecular level.

Chapter 5

Conclusion and Outlook

For decades, selective bond breaking and bond making was a dream until lasers became a common tool for molecular spectroscopists.[26-42] Vibrational mode control of reactions is a topic that has fascinated chemists using selective excitation of a vibrational state. The simplest idea is to excite an electronic ground state that maps onto the reaction coordinate; reaction dynamics can be probed by giving energy below the ionization threshold. A multiphoton vibrational excitation provides high energy (usually tera-Watt), produces the change in the electronic excitation probability, and opens several different fragmentation channels (figure 5.1 A). In comparison, vibrational excitation dumps multiple quanta of energy to a selective band for achieving high efficiency of the desired products (figure 5.1B). However, rapid intramolecular randomization of the energy seems to be a major obstacle to realizing mode-specific reactivity using laser sources. Cryogenic matrices offer a unique environment for a single photon vibrational excitation in the absence of rotational or translational degrees of freedom.[27,28] Such selective excitation of vibrational states help us understand a particular mode's role in reaction dynamics. These provide information about the conformation of TS and the orientation of reactants towards the path of a reaction. Later, pulsed lasers were used to probe the nuclear motion of the transition state in the femtosecond timescale.[42] The above experiments realized the resonance behavior in reaction coordinates during bond conversion from covalent to ionic.

The journey of the evolution of coherent chemistry in the 1990s used external stimuli and cryogenic temperatures. Strong light-matter interaction and its application control may be an unconventional alternative because it can exist even without external photons.[10-24,43-85,136] It does not require any illumination by intense external fields to influence a chemical reaction (figure 5.1 C). The last decade witnessed a surge in the use of strong coupling to modify photophysical properties like emission quantum yields, intersystem crossing, and lifetimes by

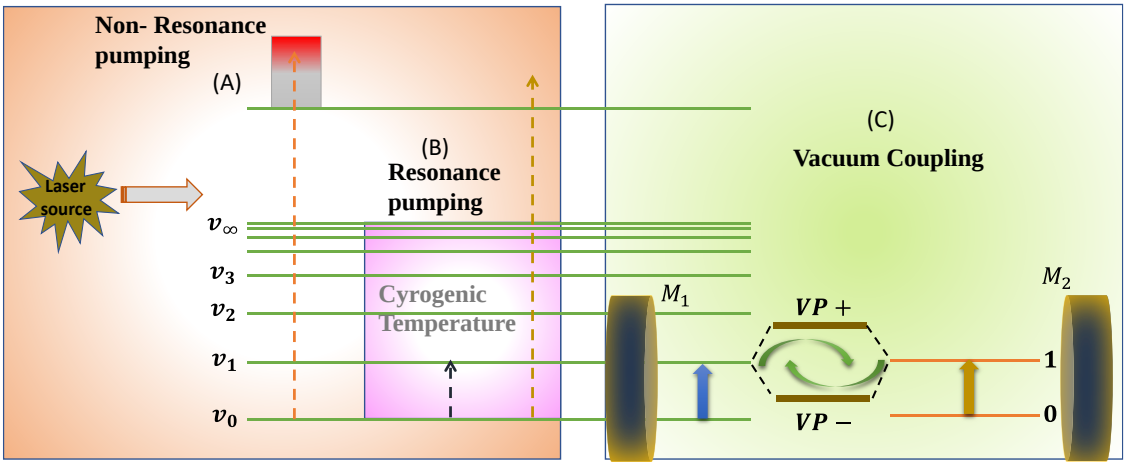

Figure 5.1. (A, B) Laser control experiments used (A) Non-resonance pumping; (B) Resonance pumping; (C) Resonance coupling using optical cavities in ground state.

coupling the first electronic excited states. The first demonstration of modified chemistry was done by electronic strong coupling of a photochromic molecule in a solid polymer matrix.[43] This proof of principle experiments suggests that reactivity could be modified under strong coupling, which came as a surprise and generated much interest among spectroscopists to couple vibrational states. Later, solution-based vibrational strong coupling was introduced that nurtured the study of homogeneous chemical reactions by selective coupling a vibrational transition.[132] In the first report, a chemical reaction under VSC of a pure reactant has been achieved; it states that band-selective coupling has a remarkable potential to modify its reactivity.[70] The high probability of the molecular vibration modes existing in the ground state can be characterized by Boltzmann distribution. The experimental difficulty facing VSC is that most homogeneous reactions occur in dilute conditions, and VSC needs a very high concentration. We have made a different approach to coupling the solvent vibrations; both match vibrational energy and simultaneously couple the reactant and solvent molecules to the infrared photon. Another advantage is that the solvent does not consume during the reaction, and the overall splitting energy is preserved. The vibro-polaritonic states formed from the collective coupling-generally known as cooperative VSC of the reactant and solvent molecules can amplify the solute-solvent interactions.

The development of polaritonic chemistry and the effect of cooperative VSC open a new tool to control the ground state chemical reaction and hence gives a new approach to understanding the mechanism of the process. In our first demonstration of cavity catalysis, the reaction rate was enhanced by three times as compared to the outside cavity. Surprisingly, the large modification of the activation energies came as a surprise which is larger in quantity than the

collective Rabi splitting observed in the system. One can precisely tune the interaction and the rate by moving the position of the cavity mode. ON-resonance to OFF-resonance experiments is the best control to understand the role of strong coupling on chemical reaction rates.

Similarly, we used isotopic experiments to prove the cooperativity in VSC and assess the role of the vibrational state involved in the reaction mechanism.[132] Change in the activation of free energy under cooperative VSC helped us to look into the structure-reactivity relationship. A study of different derivatives under VSC shows a non-linear behavior in the free-energy of activation (Hammett equation). Thermodynamics studies suggest that the mechanism of the reaction remains the same. The free energy of activation decreased by 2-5 kJ/mol, indicating a clear role of VSC in catalyzing the reaction.[109] This concept of cavity catalysis targets the vibrational bands that are selectively involved in the rate-determining process of a reaction. However, LFER elucidates that the energy density reshuffles the TS under cavity conditions. Cooperative VSC is not limited to organic reactions but has huge potential to change the catalytic efficiency of enzymatic reactions.[131] The reaction shows that it behaves competitively along with enzyme activation where the number of conversions into product per unit time is not changing. The interaction between solute and solvent is still unclear under VSC conditions.

So far, few reactions have been reported in the literature under VSC. The approach of VSC cannot be applied for the fast reactions in the present setup. However, the conformation change of an enzyme binding with the substrate involves rapid adsorption, which is too fast to be measured. VSC can be a valuable tool for studying the conformation change of large macromolecules such as proteins and enzymes. It has already been reported that VSC can be enhanced and tuned by controlling the orientation of molecules.[64] To achieve strong coupling, the molecule's transition dipole moment must be exactly parallel to the electromagnetic field. As a future endeavor, the VSC effect on the reaction rate can be studied by varying the external voltage that orient the molecule with the confined electromagnetic field. These studies will contribute to the fundamental understanding of the role of the vacuum field in chemical reactions. The first experimental observation of cavity catalysis and the effect of VSC on selective chemical reactions through many questions and open possibilities to explore further experimentally and theoretically.

References:

(1) Fetter, S. A. A. O. R.; Mozley, R. Emission And Absorption Of Radiation. *Sci. Glob. Secur.* **1990**, *1*, 265–285.

(2) Dzyaloshinskii, I. E.; Lifshitz, E. M.; Pitaevskii, L. P. The General Theory of van der Waals Forces. *Adv. Phys.* **1961**, *10*, 165–209.

(3) Rodriguez, A. W.; Capasso, F.; Johnson, S. G. The Casimir Effect in Microstructured Geometries. *Nat. Photonics* **2011**, *5*, 211–221.

(4) Lamb, W. E.; Retherford, R. C. Fine Structure of the Hydrogen Atom by a Microwave Method. *Phys. Rev.* **1947**, *72*, 241–243.

(5) Lundeen, S. R.; Pipkin, F. M. Measurement of the Lamb Shift in Hydrogen, N=2. *Phys. Rev. Lett.* **1981**, *46*, 232–235.

(6) Purcell, E. M. Proceedings of the american physical society. *Phys. Rev.* **1946**, *69*, 674–674.

(7) Kuhn, H. Classical Aspects of Energy Transfer in Molecular Systems. *J. Chem. Phys.* **1970**, *53*, 101–108.

(8) Drexhage, K. H.; Jose, S. INFLUENCE OF A DIELECTRIC INTERFACE. **1970**, *2*, 693–701.

(9) Morawitz, H.; Philpott, M. R. Coupling of an Excited Molecule to Surface Plasmons. *Phys. Rev. B* **1974**, *10*, 4863–4868.

(10) Kaiuzny, Y.; Goy, P.; Gross, M.; Raimond, J. M.; Haroche, S. Observation of Self-Induced Rabi Oscillations in 2-Level Atoms Excited inside a Resonant Cavity - the Ringing Regime of Super-Radiance, *Phys. Rev. Lett.* **1983**, *51*, 1175-1178.

(11) Haroche, S.; Kleppner, D. Cavity Quantum Electrodynamics. *Phys. Today* **1989**, *42*, 24−30.

(12) Kimble, H. J. Strong Interactions of Single Atoms and Photons in Cavity QED. *Phys. Scr.* **1998**, *76*, 127–137.

(13) Jaynes, E.T.; Cummings, F.W. Comparison of quantum and semiclassical radiation theories with application to the beam maser. *Proc. IEEE*, **1963**, *51*, 89-109.

(14) Gonzalez-Ballestero, C.; Feist, J.; Gonzalo Badía, E.; Moreno, E.; Garcia-Vidal, F. J. Uncoupled Dark States Can Inherit Polaritonic Properties. *Phys. Rev. Lett.* **2016**, *117*, 1–5.

(15) Weisbuch, C.; Nishioka, M.; Ishikawa, A.; Arakawa, Y. Observation of the Coupled Exciton-Photon Mode Splitting in a Semiconductor Quantum Microcavity. *Phys. Rev. Lett.* **1992**, *69*, 3314–3317.

(16) Kottilil, D.; Babusenan, A.; Vijayan, C.; Ji, W. Strong Light–Matter Interaction in Organic Microcavity Polaritons: Essential Criteria, Design Principles and Typical Configurations. *Eur. Phys. J. Spec. Top.* **2021**, *230*, 4091–4097.

(17) Hobson, P. A.; Barnes, W. L.; Lidzey, D. G.; Gehring, G. A.; Whittaker, D. M.; Skolnick, M. S.; Walker, S. Strong Exciton-Photon Coupling in a Low-Q All-Metal Mirror Microcavity. *Appl. Phys. Lett.* **2002**, *81*, 3519–3521.

(18) Reithmaier, J. P.; Sęk, G.; Löffler, A.; Hofmann, C.; Kuhn, S.; Reitzenstein, S.; Keldysh, L. V.; Kulakovskii, V. D.; Reinecke, T. L.; Forchel, A. Strong Coupling in a Single Quantum Dot-Semiconductor Microcavity System. *Nature* **2004**, *432*, 197–200.

(19) Gómez, D. E.; Vernon, K. C.; Mulvaney, P.; Davis, T. J. Surface Plasmon Mediated Strong Exciton-Photon Coupling in Semiconductor Nanocrystals. *Nano Letters*. **2010**, *10*, 274–278.

(20) Liu, X.; Galfsky, T.; Sun, Z.; Xia, F.; Lin, E. C.; Lee, Y. H.; Kéna-Cohen, S.; Menon, V. M. Strong Light-Matter Coupling in Two-Dimensional Atomic Crystals. *Nat. Photonics* **2014**, *9*, 30–34.

(21) Zengin, G.; Johansson, G.; Johansson, P.; Antosiewicz, T. J.; Käll, M.; Shegai, T. Approaching the Strong Coupling Limit in Single Plasmonic Nanorods Interacting with J-Aggregates. *Sci. Rep.* **2013**, *3*, 1–8.

(22) Vasa, P.; Pomraenke, R.; Cirmi, G.; De Re, E.; Wang, W.; Schwieger, S.; Leipold, D.; Runge, E.; Cerullo, G.; Lienau, C. Ultrafast Manipulation of Strong Coupling in Metal-Molecular Aggregate Hybrid Nanostructures. *ACS Nano*. **2010**, *4*, 7559–7565.

(23) Kena-Cohen, S.; Maier S.A.; Bradley D.D.C. Ultrastrongly Coupled Exciton-Polaritons in Metal-Clad Organic Semiconductor Microcavities, *Adv. Opt. Mater.* **2013**, *1*, 827-833.

(24) Schwartz, T.; Hutchison, J. A.; Genet, C.; Ebbesen, T. W. Reversible Switching of Ultrastrong Light-Molecule Coupling. *Phys. Rev. Lett.* **2011**, *106*, 1–4.

(25) Porter, G. Flash Photolysis and Spectroscopy: A New Method for the Study of Free Radical Reactions. *Life Sci. Leg. Georg. Porter* **2006**, No. 1947, 41–60.

(26) Bucksbaum, P. H.; Zavriyev, A.; Muller, H. G.; Schumacher, D. W. Softening of the H2+ Molecular Bond in Intense Laser Fields. *Phys. Rev. Lett.* **1990**, *64*, 1883–1886.

(27) Frei, H.; Pimentel, G. C. Selective Vibrational Excitation of the Ethylene-Fluorine Reaction in a Nitrogen Matrix. I. *J. Chem. Phys.* **1983**, *78*, 3698–3712.

(28) Frei, H.; Fredin, L.; Pimentel, G. C. Vibrational Excitation of Ozone and Molecular Fluorine Reactions in Cryogenic Matrices. *J. Chem. Phys.* **1980**, *74*, 397–411.

(29) Orr-Ewing, A. J.; Zare, R. N. Orientation and Alignment of Reaction Products. *Annu. Rev. Phys. Chem.* **1994**, *45*, 315–366.

(30) Zare, R. N. Laser Control of Chemical Reactions. *Science.* **1998**, *279*, 1875–1879.

(31) Fernández-Alonso, F.; Zare, R. N. Scattering Resonances in the Simplest Chemical Reaction. *Annu. Rev. Phys. Chem.* **2002**, *53*, 67–99.

(32) Crim, F. F. Bond-Selected Chemistry: Vibrational State Control of Photodissociation and Bimolecular Reaction. *J. Phys. Chem.* **1996**, *100*, 12725–12734.

(33) Tannor, D. J.; Rice, S. A.; Tannor, D. J.; Rice, S. A. Via Control of Wave Packet Evolution of Wave Packet Evolution. **1998**, *85*, 5013-5017.

(34) Brumer, P.; Shapiro, M. Coherence Chemistry: Controlling Chemical Reactions with Lasers. *Acc. Chem. Res.* **1989**, *22*, 407–413.

(35) Brumer, P.; Shapiro, M. The Essence of Control : Quantum Interference. *Annu. Rev. Phys. Chem.* **1992**, *43*, 257–282.

(36) Shapiro, M.; Brumer, P. Coherent Control of Atomic, Molecular, and Electronic Processes. *Advances in Atomic, Molecular and Optical Physics*. **2000**, *42*, 287–345.

(37) Shapiro, M.; Brumer, P. Coherent Control of Molecular Dynamics. *Reports Prog. Phys.* **2003**, *66*, 859–942.

(38) Zhu, L.; Kleiman, V.; Li, X.; Lu, S. P.; Trentelman, K.; Gordon, R. J. Coherent Laser

Control of the Product Distribution Obtained in the Photoexcitation of HI. *Science*. **1995**, *270*, 77–80.

(39) Rose, T. S.; Rosker, M. J.; Zewail, A. H. Wave Packet Oscillations (Resonance) in Dissociation Reactions. **1998**, *6672*, 22–24.

(40) Rose, T. S.; Rosker, M. J.; Zewail, A. H. Femtosecond Real-Time Probing of Reactions. IV. The Reactions of Alkali Halides. *J. Chem. Phys.* **1989**, *91*, 7415–7436.

(41) Dantus, M.; Rosker, M. J.; Zewail, A. H. Real-Time Femtosecond Probing of "Transition States" in Chemical Reactions [3]. *J. Chem. Phys.* **1987**, *87*, 2395–2397.

(42) Zewail, A. H. Femtochemistry: Atomic-Scale Dynamics of the Chemical Bond. *J. Phys. Chem. A* **2000**, *104*, 5660–5694.

(43) Hutchison, J. A.; Schwartz, T.; Genet, C.; Devaux, E.; Ebbesen, T. W. Modifying Chemical Landscapes by Coupling to Vacuum Fields. *Angew. Chem. Int. Ed.* **2012**, *51*, 1592–1596.

(44) Hutchison, J. A.; Liscio, A.; Schwartz, T.; Canaguier-Durand, A.; Genet, C.; Palermo, V.; Samorì, P.; Ebbesen, T. W. Tuning the Work-Function via Strong Coupling. *Adv. Mater.* **2013**, *25*, 2481–2485.

(45) Galego, J.; Garcia-Vidal, F. J.; Feist, J. Suppressing Photochemical Reactions with Quantized Light Fields. *Nat. Commun.* **2016**, *7*, 1–6.

(46) Flick, J.; Ruggenthaler, M.; Appel, H.; Rubio, A. Atoms and Molecules in Cavities , from Weak to Strong Coupling in Quantum-Electrodynamics (QED) Chemistry. *Proc. Nat. Acad. Sci.* **2017**, *114*, 3026-3034.

(47) Du, M.; Ribeiro, R. F.; Yuen-Zhou, J. Remote Control of Chemistry in Optical Cavities. *Chem* **2019**, *5*, 1167–1181.

(48) Coupling, L. M.; Zhong, X.; Chervy, T.; Zhang, L.; Thomas, A.; George, J.; Genet, C.; Hutchison, J. A.; Ebbesen, T. W. Energy Transfer between Spatially Separated Entangled Molecules. *Angew. Chem. Int. Ed.* **2017**, *56*, 9034–9038.

(49) Li, X.; Liu, F.; Tian, M.; Zhong, X. Tunable Multimode Plasmon − Exciton Coupling for Absorption- Induced Transparency and Strong Coupling. *J. Phys. Chem. C* **2020**, *124*, 23888–23894.

(50) Herrera, F.; Spano, F. C. Cavity-Controlled Chemistry in Molecular Ensembles. *Phys. Rev. Lett.* **2016**, *116*, 1–6.

(51) Flick, J.; Rivera, N.; Narang, P. Strong Light-Matter Coupling in Quantum Chemistry and Quantum Photonics. *Nanophotonics* **2018**, *7*, 1479–1501.

(52) Herrera, F.; Owrutsky, J. Molecular Polaritons for Controlling Chemistry with Quantum Optics. *J. Chem. Phys.* **2020**, *152*, 100902(1-19).

(53) Shalabney, A.; George, J.; Hutchison, J.; Pupillo, G.; Genet, C.; Ebbesen, T. W. Coherent Coupling of Molecular Resonators with a Microcavity Mode. *Nat. Commun.* **2015**, *6*, 1–6.

(54) Long, J. P.; Simpkins, B. S.; Coherent Coupling between a Molecular Vibration and Fabry−Perot Optical Cavity to Give Hybridized States in the Strong Coupling Limit. *ACS Photonics* **2015**, *2*, 130-136.

(55) Chervy, T.; Thomas, A.; Akiki, E.; Vergauwe, R. M. A.; Shalabney, A.; George, J.; Devaux, E.; Hutchison, J. A.; Genet, C.; Ebbesen, T. W. Vibro-Polaritonic IR Emission in the Strong Coupling Regime. *ACS Photonics* **2018**, *5*, 217–224.

(56) Vergauwe, R. M. A.; George, J.; Chervy, T.; Hutchison, J. A.; Shalabney, A.; Torbeev, V. Y.; Ebbesen, T. W. Quantum Strong Coupling with Protein Vibrational Modes. *J. Phys. Chem. Lett.* **2016**, *7*, 4159–4164.

(57) Simpkins, B. S.; Fears, K. P.; Dressick, W. J.; Spann, B. T.; Dunkelberger, A. D.; Owrutsky, J. C. Spanning Strong to Weak Normal Mode Coupling between Vibrational and Fabry-Pérot Cavity Modes through Tuning of Vibrational Absorption Strength. *ACS Photonics* **2015**, *2*, 1460–1467.

(58) Casey, S. R.; Sparks, J. R. Vibrational Strong Coupling of Organometallic Complexes. *J. Phys. Chem. C* **2016**, *120*, 28138–28143.

(59) George, J.; Shalabney, A.; Hutchison, J. A.; Genet, C.; Ebbesen, T. W. Liquid-Phase Vibrational Strong Coupling. *J. Phys. Chem. Lett.* **2015**, *6*, 1027–1031.

(60) Shalabney, A.; George, J.; Hiura, H.; Hutchison, J. A.; Genet, C.; Hellwig, P.; Ebbesen, T. W. Enhanced Raman Scattering from Vibro-Polariton Hybrid States. *Angew. Chem. Int. Ed.* **2015**, *127*, 8082–8086.

(61) Ahn, W.; Simpkins, B. S. Raman Scattering under Strong Vibration-Cavity Coupling. *J. Phys. Chem. C* **2021**, *125*, 830–835.

(62) Del Pino, J.; Feist, J.; Garcia-Vidal, F. J. Signatures of Vibrational Strong Coupling in Raman Scattering. *J. Phys. Chem. C* **2015**, *119*, 29132–29137.

(63) George, J.; Chervy, T.; Shalabney, A.; Devaux, E.; Hiura, H.; Genet, C.; Ebbesen, T. W. Multiple Rabi Splittings under Ultrastrong Vibrational Coupling. *Phys. Rev. Lett.* **2016**, *117*, 1–5.

(64) Hertzog, M.; Rudquist, P.; Hutchison, J. A.; George, J.; Ebbesen, T. W.; Börjesson, K. Voltage-Controlled Switching of Strong Light–Matter Interactions Using Liquid Crystals. *Chem. Eur. J.* **2017**, *23*,18166 –18170.

(65) Gan, C. H.; Luxmoore, I. J.; Liu, P. Q.; Valmorra, F.; Li, P.; Faist, J.; Nash, G. R. Observation of Strong Coupling between Graphene Plasmons and THz Surface Optical Phonons. *Front. Opt.* **2014**.

(66) Brawley, Z. T.; Storm, S. D.; Contreras Mora, D. A.; Pelton, M.; Sheldon, M. Angle-Independent Plasmonic Substrates for Multi-Mode Vibrational Strong Coupling with Molecular Thin Films. *J. Chem. Phys.* **2021**, *154*, 104305 (1-11).

(67) Huang, J.; Grys, D. B.; Griffiths, J.; de Nijs, B.; Kamp, M.; Lin, Q.; Baumberg, J. J. Tracking Interfacial Single-Molecule PH and Binding Dynamics via Vibrational Spectroscopy. *Sci. Adv.* **2021**, *7*, 1–9.

(68) Menghrajani, K. S.; Nash, G. R.; Barnes, W. L. Vibrational Strong Coupling with Surface Plasmons and the Presence of Surface Plasmon Stop Bands. *ACS Photonics* **2019**, *6*, 2110–2116.

(69) Menghrajani, K. S.; Chen, M.; Dholakia, K.; Barnes, W. L. Probing Vibrational Strong Coupling of Molecules with Wavelength-Modulated Raman Spectroscopy. *Adv. Opt. Mater.* **2022**, *10*, 2102065 (1-11).

(70) Thomas, A.; George, J.; Shalabney, A.; Dryzhakov, M.; Varma, S. J.; Moran, J.; Chervy, T.; Zhong, X.; Genet, C.; Hutchison, J. A.; Ebbesen, T. W. Ground-State Chemical Reactivity under Vibrational Coupling to the Vacuum Electromagnetic Field. *Angew. Chem. Int. Ed.* **2016**, *128*, 11634–11638.

(71) Thomas, A.; Jayachandran, A.; Lethuillier-Karl, L.; Vergauwe, R. M. A.; Nagarajan, K.;

Devaux, E.; Genet, C.; Moran, J.; Ebbesen, T. W. Ground State Chemistry under Vibrational Strong Coupling: Dependence of Thermodynamic Parameters on the Rabi Splitting Energy. *Nanophotonics* **2020**, *9*, 249–255.

(72) Hirai, K.; Takeda, R.; Hutchison, J. A.; Uji-i, H. Modulation of Prins Cyclization by Vibrational Strong Coupling. *Angew. Chem. Int. Ed.* **2020**, *59*, 5332–5335.

(73) Vergauwe, R. M. A.; Thomas, A.; Nagarajan, K.; Shalabney, A.; George, J.; Chervy, T.; Seidel, M.; Devaux, E.; Torbeev, V.; Ebbesen, T. W. Modification of Enzyme Activity by Vibrational Strong Coupling of Water. *Angew. Chem. Int. Ed.* **2019**, *58*, 15324–15328.

(74) Thomas, A.; Nagarajan, K.; Vergauwe, R. M. A.; George, J.; Chervy, T.; Shalabney, A.; Devaux, E.; Genet, C.; Moran, J.; Ebbesen, T. W. Tilting a Ground-State Reactivity Landscape by Vibrational Strong Coupling. *Science*. **2019**, *363*, 615–619.

(75) Fukushima, T; Yoshimitsu, S.; Murakoshi K. Inherent Promotion of Ionic Conductivity via Coherent Vibrational Strong Coupling of Water. *J. Am. Chem. Soc*. **2022**. https://doi.org/10.1021/jacs.2c02991.

(76) Joseph, K.; Kushida, S.; Smarsly, E.; Ihiawakrim, D.; Thomas, A.; Paravicini-Bagliani, G. L.; Nagarajan, K.; Vergauwe, R.; Devaux, E.; Ersen, O.; Bunz, U. H. F.; Ebbesen, T. W. Supramolecular Assembly of Conjugated Polymers under Vibrational Strong Coupling. *Angew. Chem. Int. Ed.* **2021**, *133*, 19817–19822.

(77) Grafton, A. B.; Dunkelberger, A. D.; Simpkins, B. S.; Triana, J. F.; Hernández, F. J.; Herrera, F.; Owrutsky, J. C. Excited-State Vibration-Polariton Transitions and Dynamics in Nitroprusside. *Nat. Commun.* **2021**, *12*, 1–9.

(78) Thomas, A.; Devaux, E.; Nagarajan, K.; Rogez, G.; Seidel, M.; Richard, F.; Genet, C.; Drillon, M.; Ebbesen, T. W. Large Enhancement of Ferromagnetism under a Collective Strong Coupling of YBCO Nanoparticles. *Nano Lett.* **2021**, *21*, 4365−4370.

(79) Pang, Y.; Thomas, A.; Nagarajan, K.; Vergauwe, R. M. A.; Joseph, K.; Patrahau, B.; Wang, K.; Genet, C.; Ebbesen, T. W. On the Role of Symmetry in Vibrational Strong Coupling: The Case of Charge-Transfer Complexation. *Angew. Chem. Int. Ed.* **2020**, *132*, 10522–10526.

(80) Mandal, A.; Li, X.; Huo, P. Theory of Vibrational Polariton Chemistry in the Collective

Coupling Regime. *J. Chem. Phys.* **2022**, *156*, 014101.

(81) Schütz, S.; Schachenmayer, J.; Hagenmüller, D.; Brennen, G. K.; Volz, T.; Sandoghdar, V.; Ebbesen, T. W.; Genes, C.; Pupillo, G. Ensemble-Induced Strong Light-Matter Coupling of a Single Quantum Emitter. *Phys. Rev. Lett.* **2020**, *124*, 113602.

(82) Li, T. E.; Nitzan, A.; Subotnik, J. E. Collective Vibrational Strong Coupling Effects on Molecular Vibrational Relaxation and Energy Transfer: Numerical Insights via Cavity Molecular Dynamics Simulations**. *Angew. Chem. Int. Ed.* **2021**, *60*, 15533–15540.

(83) Pannir-Sivajothi, S.; Campos-Gonzalez-Angulo, J. A.; Martínez-Martínez, L. A.; Sinha, S.; Yuen-Zhou, J. Driving Chemical Reactions with Polariton Condensates. *Nat. Commun.* **2022**, *13*, 1–9.

(84) Hirai, K.; Ishikawa, H.; Chervy, T.; Hutchison, J. A.; Uji-i, H. Selective Crystallization via vibrational Strong Coupling. *Chem. Sci.* **2021**, *12*, 11986–11994.

(85) Ahn, W; Herrera, F.; Simpkins, B. S. Modification of Urethane Addition Reaction via Vibrational Strong Coupling. DOI :10.26434/chemrxiv-**2022**.

(86) Biggs, A. I. A Spectrophotometric Determination of the Dissociation Constants of P-Nitrophenol and Papaverine. *Trans. Faraday Soc.* **1954**, *50*, 800–802.

(87) Bender, M. L.; Turnquest, B. W. General Basic Catalysis of Ester Hydrolysis and Its Relationship to Enzymatic Hydrolysis. *J. Am. Chem. Soc.* **1957**, *79*, 1656–1662.

(88) Clark, J. H. Fluoride Ion as a Base in Organic Synthesis. *Chem. Rev.* **1980**, *80*, 429–452.

(89) Jencks, W. P.; Gilchrist, M. Nonlinear Structure-Reactivity Correlations. The Reactivity of Nucleophilic Reagents toward Esters. *J. Am. Chem. Soc.* **1968**, *90*, 2622–2637.

(90) Mitton, C. G.; Schowen, R. L.; Gresser, M.; Shapley, J. Isotope Exchange and Solvolysis in the Basic Methanolysis of Aryl Esters. Molecular Interpretation of Free Energies, Enthalpies, and Entropies of Activaiion. *J. Am. Chem. Soc.* **1969**, *91*, 2036–2044.

(91) Lather, J.; Bhatt, P.; Thomas, A.; Ebbesen, T. W.; George, J. Cavity Catalysis by Cooperative Vibrational Strong Coupling of Reactant and Solvent Molecules. *Angew. Chemie* **2019**, *131*, 10745–10748.

(92) Universitit, F. C. Der. Empirical Parameters of Solvent Polarity as Linear Free-Energy Relationships. *Angew. Chem. Int. Ed.* **1979**, *110*, 98–110.

(93) Hammett, L. P. The Effect of Structure upon the Reactions of Organic Compounds . Benzene Derivatives Reactivity. *J. Am. Chem. Soc.* **1937**, *59*, 96-103.

(94) Shorter, B. J. The Separation of Polar, Steric, and Resonance Effects in Organic Reactions by the Use of Linear Free Energy Relationships. *Chem. Soc. Rev.* **1970**, 433-453.

(95) Taft. R. W. The Separation of Relative Free Energies of Activation to Three Basic Contributing Factors and the Relationship of These to Structure. *J. Am. Chem. Soc.* **1953**, *75*, 4534–4537.

(96) Wells, P. R. Linear Free Energy Relationships. *Chem. Rev.* **1963**, *63*, 171-219.

(97) Schreck, J. O. Nonlinear Hammett Relationships. *J. Chem. Educ.* **1971**, 48, 103–107.

(98) Um, I.; Im, L.; Kim, E.; Shin, J. H. Nonlinear Hammett Plots in Pyridinolysis of 2 , 4-Dinitrophenyl X-Substituted Benzoates: Change in RDS versus Resonance Contribution. *Org. Biomol. Chem.* **2010**, *8*, 3801–3806.

(99) Liu, L; and Guo, W. X. Isokinetic Relationship, Isoequilibrium Relationship, and Enthalpy−Entropy Compensation. *Chem. Rev.* **2001**, *101*, 673−695.

(100) Linert, W. Mechanistic and Structural Investigations Based on the Isokinetic Relationship. *Chem. Soc. Rev.* **1994**, *23*, 429-438.

(101) Keenan, S. L.; Peterson, K. P.; Peterson, K.; Jacobson, K. Determination of Hammett Equation Rho Constant for the Hydrolysis of p -Nitrophenyl Benzoate Esters. *J. Chem. Educ.* **2008**, *85*, 558–560.

(102) Urn, I.; Kwon, D. Evidence of a Stepwise Acyl-transfer Reaction Mechanism : Nonlinear Hammet Plots for Reactions of p-Nitrophenyl Substituted Benzoates with Hydroxide and p-Chlorophenoxide. *Tetrahedron Lett.* **1997**, *38*, 4787–4790.

(103) Cainelli, G.; Galletti, P.; Giacomini, D. Solvent Effects on Stereoselectivity: More than Just an Environment. *Chem. Soc. Rev.* **2009**, *38*, 990–1001.

(104) Kadyan, A.; Shaji, A.; George, J. Boosting Self-Interaction of Molecular Vibrations under Ultrastrong Coupling Condition. *J. Phys. Chem. Lett.* **2021**, *12*, 4313–4318.

(105) Timbers, P. J.; Parmenter, C. S.; Moss, D. B. Acceleration of Intramolecular Vibrational Redistribution by Methyl Internal Rotation. II. A Comparison of m-Fluorotoluene and

p-Fluorotoluene. *J. Chem. Phys.* **1994**, *100*, 1028–1034.

(106) Xiang, B.; Ribeiro, R. F.; Du, M.; Chen, L.; Yang, Z.; Wang, J.; Yuen-Zhou, J.; Xiong, W. Intermolecular Vibrational Energy Transfer Enabled by Microcavity Strong Light–Matter Coupling. *Science.* **2020**, *368*, 665–667.

(107) Li, X.; Mandal, A.; Huo, P. Cavity Frequency-Dependent Theory for Vibrational Polariton Chemistry. *Nat. Commun.* **2021**, *12*, 1–9.

(108) Lindoy, L. P.; Mandal, A.; Reichman, D. R. Resonant Cavity Modification of Ground State Chemical Kinetics. **2022**, 1–9.

(109) Lather, J.; Thabassum, A. N. K.; Singh, J.; George, J. Chemical Science Cavity Catalysis : Modifying Linear Free-Energy Relationship under Cooperative Vibrational Strong Coupling. *Chem. Sci.*, **2022**, *13*, 195-202.

(110) Singh, B. R. Basic Aspects of the Technique and Applications of Infrared Spectroscopy of Peptides and Proteins. *ACS Symposium Series.* **2000**, 750, 2-37.

(111) Chuntonov, L.; Kumar, R.; Kuroda, D. G.; Rouge, B. Non-linear infrared spectroscopy of the water bending mode: Direct experimental evidence of hydration shell reorganization? *Phys Chem Chem Phys.* **2015**, *16*, 13172–13181.

(112) Voet, D; Pratt, C. W.; Voet, J. G. Principles of Biochemistry**.** Rates of Enzymatic Reactions Chapter *14*, 482–505.

(113) Warshel, A. Electrostatic Origin of the Catalytic Power of Enzymes and the Role of Preorganized Active Sites. *J. Biol. Chem.* **1998**, *273*, 27035-27038.

(114) Warshel, A.; Papazyan, A.; Kollman, P. A.; Cleland, W. W.; Kreevoy, M. M.; Frey. P.A. On Low-Barrier Hydrogen Bonds and Enzyme Catalysis. *Science.* **2020**, *269*, 102–106.

(115) Blow, D. M. Structure and Mechanism of Chymotrypsin. *Acc. Chem. Res.* **1976**, *678*, 672–678.

(116) Bender, M. L.; Kézdy, F. J.; Wedler, F. C. Alpha-Chymotrypsin: Enzyme Concentration and Kinetics. *J. Chem. Educ.* **1967**, *44*, 84–88.

(117) Verma, S. K.; Ghosh, K. K. Activity, Stability and Kinetic Parameters for α-Chymotrypsin Catalysed Reactions in AOT/Isooctane Reverse Micelles with Nonionic and Zwitterionic Mixed Surfactants. *J. Chem. Sci.* **2013**, *125*, 875–882.

(118) Gutfreund, H.; Sturtevant J. M. The Mechanism of the Reaction of Chymotrypsin with P-Nitrophenyl Acetate. *Biochem. J.* **1956**, *63*, 656–661.

(119) Kong, J.; Yu, S. Fourier Transform Infrared Spectroscopic Analysis of Protein Secondary Structures. **2007**, *39*, 549–559.

(120) Volini, M.; Tobias, P. Circular Dichroism Studies of Chymotrypsin and Its Derivatives. *J. Biochem.* **1969**, *244*, 5105–5109.

(121) Simon, L. M.; Kotorma, M.; Garab, G.; Laczko, I. Structure and Activity of alpha-Chymotrypsin and Trypsin in Aqueous Organic Media. *Biochem. Biophys.* **2001**, *280*, 1367–1371.

(122) Cassidy, C. S.; Lin, J.; Frey, P. A. The Deuterium Isotope Effect on the NMR Signal of the Low-Barrier Hydrogen Bond in a Transition- State Analog Complex of Chymotrypsin. *Biochem. Biophys. Res. Commun.* **2000**, *273*, 789–792.

(123) Bender, B. M. L.; Clement, G. E.; Kézdy, F. J. The Correlation of the pH (pD) Dependence and the Stepwise Mechanism of alpha-Chymotrypsin-Catalyzed Reactions. *J. Am. Chem. Soc.* **1964**, *86*, 3680–3690.

(124) Kresge, A. J. Solvent Isotope Effects and the Mechanism of Chymotrypsin Action. *J. Am. Chem. Soc.* **1973**, *95*, 3065–3067.

(125) Abuin, E.; Lissi, E.; Bridi, R. Kinetics of p - Nitrophenyl acetate hydrolysis catalyzed by α- Chymotrypsin in presence of polyethylene glycol. *J. Chil. Chem. Soc.* **2015**, *56*, 948-950.

(126) Gupta, B. S.; Taha, M.; Lee, M. RSC Advances Superactivity of α- Chymotrypsin with Biological. *RSC Adv.*, **2014**,*4*, 51111-51116.

(127) Frey, P. A.; Whitt, S. A.; Tobin, J. B. A Low-Barrier Hydrogen Bond in the Catalytic Triad of Serine Proteases A-B. *Science*. **1994**, *264*, 1927–1930.

(128) Carey, C.; Cheng, Y.; Rossky, P. J. Hydration Structure of the a -Chymotrypsin Substrate Binding Pocket : The Impact of Constrained Geometry. *J. Chem. Phys.* **2000**, *258*, 415-425.

(129) Wiesehan, G. D.; Xiong, W. Negligible Rate Enhancement from Reported Cooperative Vibrational Strong Coupling Catalysis. *J. Chem. Phys.* **2021**, *155*, 241103.

(130) Schäfer, C. Polaritonic Chemistry from First Principles via Embedding Radiation Reaction. *J. Phys. Chem. Lett.* **2022**, 13, 6905−6911.

(131) Lather, J.; George, J. Improving Enzyme Catalytic Efficiency by Co-Operative Vibrational Strong Coupling of Water. *J. Phys. Chem. Lett.* **2021**, *12*, 379–384.

(132) Nagarajan, K.; Thomas, A.; Ebbesen, T. W. Chemistry under Vibrational Strong Coupling. *J. Am. Chem. Soc.* **2021**, *143*, 16877–16889.

(133) Gómez, A. J. Reproducibility of Effects of Vibrational Strong Coupling on Chemical Reaction Rates. *UC San Diego Electron. Theses Diss.* **2022**.

(134) Singh, J.; Lather, J.; George, Solvent Dependence on Cooperative Vibrational Strong Coupling and Cavity Catalysis. DOI: https://doi.org/10.26434/chemrxiv-2022-vmwn0. **2022**.

(135) Scholes, G. D.; Delpo, C. A.; Kudisch, B. Entropy Reorders Polariton States. *J. Phys. Chem. Lett.* **2020**, *11*, 6389–6395.

(136) Damari, R.; Weinberg, O.; Krotkov, D.; Demina, N.; Akulov, K.; Golombek, A.; Schwartz, T.; Fleischer, S. Strong Coupling of Collective Intermolecular Vibrations in Organic Materials at Terahertz Frequencies. *Nat. Commun.* **2019**, *10*, 1–8.

(137) Bhattacharyya, D.; Videla, P. E.; Cattaneo, M.; Batista, V. S.; Lian, T.; Kubiak, C. P. vibrational Stark Shift Spectroscopy of Catalysts under the Influence of Electric Fields at electrode-Solution Interfaces. *Chem. Sci.* **2021**, *12* , 10131–10149.

(138) Lindoy, L. P.; Mandal, A.; Reichman, D. R. Resonant Cavity Modification of Ground State Chemical Kinetics. **2022**, 1–9.

(139) Li, X.; Mandal, A.; Huo, P. Cavity Frequency-Dependent Theory for Vibrational Polariton Chemistry. *Nat. Commun.* **2021**, *12*, 1–9.

List of Publications

- J. Lather, A. N. K. Thabassum, J. Singh, J. George, Cavity Catalysis: Modifying Linear Free-energy Relationship under Cooperative Vibrational Strong Coupling. Chem. Sci. 2022, 13, 195–202.
- J. Lather, J. George, Improving Enzyme Catalytic Efficiency by Co-operative Vibrational Strong Coupling of Water. J. Phys. Chem. Lett. 2021, 12, 379-384.
- J. Lather, P. Bhatt, A. Thomas, T. W. Ebbesen*, J. George* "Cavity Catalysis by Cooperative Vibrational Strong Coupling of Reactant and Solvent Molecules" Angew. Chem. Int. Ed. 2019, 58, 10635-10638.
- J. Singh, J. Lather, J. George. Solvent Dependence on Cooperative Vibrational Strong Coupling and Cavity Catalysis. DOI: https://doi.org/10.26434/chemrxiv-2022-vmwn0. 2022.

Conference presentations

- A talk *"Controlling Chemical Reaction Rate by Coupling to Vacuum Field"* in a live focus session of "Chemistry in a New Light - Altering Reactivity and Selectivity with Optical Cavities" in the annual conference "NWO CHAINS 2021, The Netherlands" on 8 December 2021.
- A talk *"Controlling Chemical Reactions by Cooperative Vibrational Strong Coupling"* at the "11th Asian Photochemistry Conference" (APC 2021), held on Oct 31-Nov 4, 2021.
- A poster *"Controlling Enzymatic Reactions by Vibrational Strong Coupling of Water"* in the 17th conference on "Spectroscopy and Dynamics of Molecules and Clusters (SDMC-2020) organized by BITS Pilani, Pilani campus and IIT Jodhpur" held 20th to 23rd February 2020.
- A poster *"Controlling Enzymatic Reactions by Vibrational Strong Coupling of Water"* in "1st CRIKC Chemistry Symposium" from 2nd-3rd November 2019, co-organized by IISER Mohali.
- A poster *"Cavity Catalysis by Co-operative Vibrational Strong Coupling of Reactant and Solvent Molecules"* in 25th CRSI National Symposium in chemistry July 19-21, 2019, organized by IIT Kanpur.
- A poster *"Controlling Chemical Reaction Rates via Vibro-polaritonic States"* in RAOBC, organized by IISER Mohali in association with the Royal Society of Chemistry during March 22-24, 2019.
- A poster *"Accelerating Chemical Reaction Rate by Vibrational Strong Coupling of Solvent Molecules"* in FCS 2018; organized by JNU, IIT Delhi, and co-organized by TIFR Mumbai, Fluorescence Society.